NAVAL POSTGRADUATE SCHOOL
Monterey, California

DISSERTATION

SENSITIVITY OF A NAVY REGIONAL OCEAN MODEL TO HIGH-RESOLUTION ATMOSPHERIC MODEL AND SCATTEROMETER WIND FORCING

by

Henry Jones

September 2003

Dissertation Supervisor: Mary L. Batteen

Approved for public release; distribution is unlimited

THIS PAGE INTENTIONALLY LEFT BLANK

REPORT DOCUMENTATION PAGE			Form Approved OMB No. 0704-0188

Public reporting burden for this collection of information is estimated to average 1 hour per response, including the time for reviewing instruction, searching existing data sources, gathering and maintaining the data needed, and completing and reviewing the collection of information. Send comments regarding this burden estimate or any other aspect of this collection of information, including suggestions for reducing this burden, to Washington headquarters Services, Directorate for Information Operations and Reports, 1215 Jefferson Davis Highway, Suite 1204, Arlington, VA 22202-4302, and to the Office of Management and Budget, Paperwork Reduction Project (0704-0188) Washington DC 20503.

1. AGENCY USE ONLY *(Leave blank)*	2. REPORT DATE September 2003	3. REPORT TYPE AND DATES COVERED Dissertation

4. TITLE AND SUBTITLE: Title (Mix case letters) Sensitivity of a Navy Regional Ocean Model to High-Resolution Atmospheric and Scatterometer Wind Forcing	5. FUNDING NUMBERS
6. AUTHOR(S) Henry Jones	
7. PERFORMING ORGANIZATION NAME(S) AND ADDRESS(ES) Naval Postgraduate School Monterey, CA 93943-5000	8. PERFORMING ORGANIZATION REPORT NUMBER
9. SPONSORING / MONITORING AGENCY NAME(S) AND ADDRESS(ES) N/A	10. SPONSORING / MONITORING AGENCY REPORT NUMBER

11. SUPPLEMENTARY NOTES The views expressed in this thesis are those of the author and do not reflect the official policy or position of the Department of Defense or the U.S. Government.

12a. DISTRIBUTION / AVAILABILITY STATEMENT Approved for public release; distribution is unlimited	12b. DISTRIBUTION CODE

13. ABSTRACT *(maximum 200 words)*

As the focus of Navy attention shifts to littoral regions, higher resolution and re-locatable nested models have been developed to improve shallow-water operations for ocean prediction. One of the scientific and technical challenges is to determine accuracy of ocean models on high-resolution grids needed to meet operational requirements for ocean prediction. A series of 14-day experiments are performed to evaluate the sensitivity of a regional ocean model to low-resolution Navy Ocean Global Atmospheric Prediction System (NOGAPS) versus high-resolution Coupled Ocean Atmospheric Model Prediction System (COAMPS) wind forcing that includes scatterometer data from synthetic QuikSCAT (quick scatterometer mission) observations. Atmospheric model wind stress/wind stress curl and Pacific West Coast ocean model (PWC) surface and subsurface current/temperature model results are compared and analyzed. The results show that there is significant sensitivity in sea surface current and wind stress variability to the choice of atmospheric model grid resolution and the insertion of high-resolution satellite data. In coastal areas, increasing atmospheric model resolution produces a finer depiction of the variability observed near capes and promontories. Insertion of QuikSCAT data produces a statistical difference but no significant difference in the model fields. The ocean model runs have the expected climatological features and variability. The higher wind stress in COAMPS causes the ocean model to predict higher velocity currents and better-defined eddies near capes and promontories. However, comparisons to observations show that using models with the same high-resolution for all regions may not be an efficient use of computer resources.

14. SUBJECT TERMS Sigma Coordinate Model, NOGAPS, COAMPS, Scatterometer, High-Resolution	15. NUMBER OF PAGES 150
	16. PRICE CODE

17. SECURITY CLASSIFICATION OF REPORT	18. SECURITY CLASSIFICATION OF THIS PAGE	19. SECURITY CLASSIFICATION OF ABSTRACT	20. LIMITATION OF ABSTRACT
Unclassified	Unclassified	Unclassified	UL

NSN 7540-01-280-5500 Standard Form 298 (Rev. 2-89)
Prescribed by ANSI Std. 239-18

THIS PAGE INTENTIONALLY LEFT BLANK

Approved for public release; distribution is unlimited

SENSITIVITY OF A NAVY REGIONAL OCEAN MODEL TO HIGH-RESOLUTION ATMOSPHERIC MODEL AND SCATTEROMETER WIND FORCING

Henry Jones
Commander, United States Navy
B.S., United States Naval Academy, 1979
M.S., Naval Postgraduate School, 1986

Submitted in partial fulfillment of the
requirements for the degree of

DOCTOR OF PHILOSOPHY IN PHYSICAL OCEANOGRAPHY

from the

NAVAL POSTGRADUATE SCHOOL
September 2003

Author: _____
Henry Jones

Approved by:

_____
Mary L. Batteen
Associate Professor of Oceanography
Dissertation Supervisor

_____
Roland W. Garwood
Professor of Oceanography

_____
Curtis A. Collins
Professor of Oceanography

_____
Wendell A. Nuss
Associate Professor of Meteorology

_____
Douglas K. Miller
Associate Research Professor of Meteorology

Approved by: _____
Mary L. Batteen, Chair, Department of Oceanography

Approved by: _____
Carson K. Eoyang, Associate Provost for Academic Affairs

THIS PAGE INTENTIONALLY LEFT BLANK

ABSTRACT

As the focus of Navy attention shifts to littoral regions, higher resolution and re-locatable nested models have been developed to improve shallow-water operations for ocean prediction. One of the scientific and technical challenges is to determine accuracy of ocean models on high-resolution grids needed to meet operational requirements for ocean prediction. A series of 14-day experiments are performed to evaluate the sensitivity of a regional ocean model to low-resolution Navy Ocean Global Atmospheric Prediction System (NOGAPS) versus high-resolution Coupled Ocean Atmospheric Model Prediction System (COAMPS) wind forcing that includes scatterometer data from synthetic QuikSCAT (quick scatterometer mission) observations. Atmospheric model wind stress/wind stress curl and Pacific West Coast ocean model (PWC) surface and subsurface current/temperature model results are compared and analyzed. The results show that there is significant sensitivity in sea surface current and wind stress variability to the choice of atmospheric model grid resolution and the insertion of high-resolution satellite data. In coastal areas, increasing atmospheric model resolution produces a finer depiction of the variability observed near capes and promontories. Insertion of QuikSCAT data produces a statistical difference but no significant difference in the model fields. The ocean model runs have the expected climatological features and variability. The higher wind stress in COAMPS causes the ocean model to predict higher velocity currents and better-defined eddies near capes and promontories. However, comparisons to observations show that using models with the same high-resolution for all regions may not be an efficient use of computer resources.

THIS PAGE INTENTIONALLY LEFT BLANK

TABLE OF CONTENTS

I. INTRODUCTION 1
A. PURPOSE 1
B. OBJECTIVE 4

II. EXPERIMENT DESIGN 5
A. OCEAN MODELS 5
B. ATMOSPHERIC MODELS 7
C. NUMERICAL EXPERIMENTS 8
1. Atmospheric Models 8
2. Ocean Model 10
3. Scatterometer Winds 11

III. DATA ANALYSIS 21
A. STATISTICAL METHODS 21
1. Accuracy measures 21
2. Student t-test and Analysis of Variance (ANOVA) 22
3. Empirical orthogonal functions (EOF) 23
4. Autocorrelations and Crosscorrelations 24
B. WIND STRESS CURL, VORTICITY AND EKE 25
1. Wind Stress Curl 25
2. Vorticity 26
3. Eddy Kinetic Energy (EKE) 26
C. FIELD DATA 27
1. Cruise Data 27
2. CODAR 27
3. Moored Buoys 28
D. INTERPOLATION ISSUES 29

IV. PHYSICAL ENVIRONMENT 35
A. COASTAL METEOROLOGY 35
B. COASTAL OCEANOGRAPHY 36

V. ATMOSPHERIC MODEL RESULTS 39
A. STATISTICAL TESTS 39
B. WIND STRESS 40
1. Wind Structure Resolution 41
2. Wind Stress Curl 43
C. COMPARISON TO OBSERVATIONS 44
E. DISCUSSION AND SUMMARY 46

VI. OCEAN MODEL RESULTS 63
A. OCEAN CURRENT 63
1. Surface Current Velocity 63
2. Eddy Kinetic Energy (EKE) and Vorticity 66

C. CODAR 70
D. CALCOFI 71
E. DISCUSSION AND SUMMARY 72
VII. CONCLUSIONS AND RECOMMENDATIONS 101
APPENDIX A. SUPPLEMENTAL GRAPHICS & TABLES 105
LIST OF REFERENCES 109
INITIAL DISTRIBUTION LIST 125

LIST OF FIGURES

Figure 2.1. COAMPS/PWC domains. 16
Figure 2.2. 09 January 1999 synthetic QuikSCAT swaths. 17
Figure 2.3. (A) Real and (B) synthetic QuikSCAT winds for 29 January 2000. 18
Figure 2.4. Real/synthetic QuikSCAT winds (1200 UTC 30 Jan 2000). 19
Figure 2.5. Same as Figure 2.4, except for Cape Mendocino. 20
Figure 3.1. Actual CenCal CalCOFI tracks for the period of 06-20 Jan 1999. 31
Figure 3.2. Monterey Bay CODAR Sites and MBARI moorings. 32
Figure 3.3. Pacific West Coast NDBC Moored Buoys. 33
Figure 5.1. NOGAPS/COAMPS wind stress for 07-21 January 1999. 49
Figure 5.2. First EOF of wind stress for 07-21 January 1999. 50
Figure 5.3. Second EOF of wind stress for 07-21 January 1999. 51
Figure 5.4. COAMPS 10 km mean wind stress for 07-21 January 1999. 52
Figure 5.5. COAMPS 45 km wind stress (0900 UTC, 07 Jan 1999). 53
Figure 5.6. Same as Figure 5.8, expect for COAMPS 10 km. 54
Figure 5.7. COAMPS 45 km mean wind stress curl (07-21 Jan 1999). 55
Figure 5.8. COAMPS 10 km wind stress curl (0900 UTC, 07 Jan 1999). 56
Figure 5.9. Buoy wind stress - San Francisco to St. George (17 Jan 1999). 57
Figure 5.10. NDBC buoy 46005 (Washington) wind stress versus. 58
Figure 5.11. C-MAN station TTIW1 (Tatoosh, Island) wind stress. 59
Figure 5.12. PTGC1 (Point Arguello, CA) wind stress. 60
Figure 5.13. Buoy wind stress RMSE (46053, 46054, 46023, PTGC1). 61
Figure 5.14. Same as Figure 5.12, except for mean error (ME). 62
Figure 6.1. COAMPS 25 km mean current speed. 75
Figure 6.2. PWC mean surface current speed. 76
Figure 6.3. COAMPS 45 km first EOF of current speed. 77
Figure 6.4. COAMPS 45 km second EOF of Current speed. 78
Figure 6.5. Southern California Bight (COAMPS 10 km). 79
Figure 6.6. PWC SST 07-21 January 1999 (NOGAPS). 80
Figure 6.7. Same as Figure 6.6, except for COAMPS 10 km. 81
Figure 6.8. Mean current in the vicinity of Cape Mendocino. 82
Figure 6.9 Depth integrated current for 00 UTC, 19 January 1999 (NOGAPS). 83
Figure 6.10 Same as Figure 6.9 except for COAMPS 25 km. 84
Figure 6.11 Washington coast mean depth integrated EKE 85
Figure 6.12 PWC mean surface current vorticity (COAMPS 10 km). 86
Figure 6.13. Mean current vorticity for vicinity of Cape Mendocino. 87
Figure 6.14. NDBC buoy 46023 (Pt. Arguello) ADCP 25 m depth velocity. 88
Figure 6.15. Same as Figure 6.15, except for buoy 46054 (Santa Barbara, West). 89
Figure 6.16. Same as Figure 6.15, except for buoy 46062 (Pt. San Luis). 90
Figure 6.17. MBARI buoy M1 ADCP 22.64 m depth velocity. 91
Figure 6.18. MBARI buoy M2 ADCP 25.76 m depth velocity. 92
Figure 6.19. MBARI buoy M3 ADCP 25.76 m depth velocity. 93
Figure 6.20. Buoy 46023 (Pt. Arguello) RMSE. 94

Figure 6.21. Same as Figure 6.25, except for Buoy M1 95
Figure 6.22. Buoy 46062 (Port San Luis) & PWC current speed. 96
Figure 6.23. CODAR & PWC (CMP 10 km) current velocity (20 Jan 1999)..... 97
Figure 6.24. NAVO & PWC (CMP 10 km) current velocity (13 Jan 1999). 98
Figure 6.25. NAVO & PWC (CMP 25 km) current velocity (16 Jan 1999). 99
Figure 6.26. NAVO & PWC (CMP 45 km w/Q) current velocity (19 Jan 1999)..... 100
Figure A.1. NDBC buoy and tidal currents..... 107
Figure A.2. MBARI buoy and tidal currents..... 108

LIST OF TABLES

Table 2.1 Numerical Experiments 8
Table 2.2. COAMPS Wind Stress Input 10
Table A.1 NDBC buoy locations, depths, and distances to model gridpoints. 105
Table A.2. ADCP buoy depth levels (meters). 106

THIS PAGE INTENTIONALLY LEFT BLANK

LIST OF SYMBOLS, ACRONYMS AND/OR ABBREVIATIONS

ADCP	Acoustic Doppler Current Profiler
ADEOS	Advanced Earth Observing Satellite
ADFC	Altimeter Data Fusion Center
AE	Absolute Error
ANOVA	Analysis of Variance
ARSC	Arctic Region Supercomputing Center
CalCOFI	California Cooperative Fisheries Investigations
CenCAL	Central California
CC	California Current
CCS	California Current System
CMP	COAMPS
COAMPS	Coupled Ocean Atmospheric Mesoscale Prediction System
CODAR	Costal Ocean Doppler Radar
CTD	Conductivity Temperature Depth
CUC	California Undercurrent
DBDB5	Digital Bathymetric Data Base (0.5 minutes)
DC	Davidson Current
DMSP	Defense Meteorological Satellite Program
ECMWF	European Centre for Medium-Range Weather Forecasts
EKE	Eddy Kinetic Energy
EOF	Empirical Orthogonal Function
ERS	European Remote Sensing Satellite
FE	Forecast Error
FNMOC	Fleet Numerical Meteorology and Oceanography Center
FOV	Field of View
GCM	Global Climate Model
GDEM	Generalized Digital Environmental Model
HPC	High Performance Computing
IC	Initial Condition
MABL	Marine Atmospheric Boundary Layer
MAE	Mean Absolute Error
MBARI	Monterey Bay Aquarium Research Institute
MCSST	Multi-channel Sea Surface Temperature
ME	Mean Error
MM5	Penn State/NCAR Mesoscale Model Version 5
MSE	Mean-Squared Error
MLD	Mixed Layer Depth
NASA	National Aeronautics and Space Administration
NAVOCEANO	Naval Oceanographic Office
NCAR	National Center for Atmospheric Research
NCDC	National Climatic Data Center
NCOM	Navy Coastal Ocean Model

NDBC	National Data Buoy Center
NGP	NOGAPS
NLOM	NRL Layered Ocean Model
NMLD	NRL Mixed Layer Depth
NOGAPS	Navy Oceanographic Global Atmospheric Prediction System
NOAA	National Oceanographic Atmospheric Administration
NORAD	North American Defense Command
NPS	Naval Postgraduate School
NRL	Naval Research Laboratory
NWP	Numerical Weather Predition
OI	Optimum Interpolation
POM	Princeton Ocean Model
PWC	Pacific West Coast Ocean Model
/Q	with QuikSCAT
QuikSCAT	NASA's Quick Scatterometer Satellite
RMSE	Root Mean Square Error
SCC	Southern California Counter Current
SCE	Southern California Eddy
SFC	Surface
SOAP	Satellite Orbital Analysis Program
SSH	Sea Surface Height
SSM/I	Special Sensor Microwave Imager
SST	Sea Surface Temperature
UTC	Coordinated Universal time
XBT	Expendable Bathythermograph

ACKNOWLEDGMENTS

Computing resources were provided by the Fleet Numerical Meteorological and Oceanographic Command (FNMOC), Center for High Performance Computing (HPC) at the Arctic Region Supercomputing Center (ARSC) and Naval Oceanographic Office (NAVOCEANO).

A special thanks to my dissertation advisor Mary Batteen and former Chair, Roland Garwood, for providing me the opportunity to pursue my degree while working as a full-time NPS faculty member and later as a long-distance student on the faculty of the United States Naval Academy. I would like to thank Mike Clancy (FNMOC) for providing the initial direction for my research and my committee members, Mary Batteen, Roland Garwood, Curtis Collins, Wendell Nuss and Douglas Miller for their time, constructive criticism and patience.

Webb DeWitt (FNMOC), Paul May (NRL Monterey) and Dong-Shan Ko (NRL Stennis) generously shared their time and expertise in guiding me through the intricacies of the ocean and atmospheric models. Mike Cook (NPS) and Dylan Righi (Oregon State University) were invaluable in providing answers to MATLAB questions and assisting in the design of my graphic programs.

I would like to thank my wife, Dr. Stacy Harris, for her support, encouragement and patience throughout my trials and tribulations. A special thanks to Dr. Abel B. Sykes for serving as a role model and inspiration for pursuing the degree. Finally, I would like to thank my parents, Una Jones and Henry Jones, Sr., and my sister, Mona Jones, for their guidance towards my life goals of naval service and scientific learning.

THIS PAGE INTENTIONALLY LEFT BLANK

EXECUTIVE SUMMARY

As the focus of Navy attention shifts to littoral regions, higher resolution and re-locatable nested models have been developed to improve shallow-water operations, including better search planning and tactics development in range and azimuth dependent environments. In the coastal and shallow water environments, mesoscale oceanographic processes (~2-50 km horizontal space scales and ~2-10 day time scales) over the continental shelf are mostly influenced by the variability of atmospheric forcing (Batteen, 1997). One of the scientific and technical challenges is to determine the accuracy of ocean models on high-resolution grids needed to meet operational requirements in ocean prediction.

Wind data from satellites and high resolution atmospheric models are providing a wealth of high-resolution data to augment the historically sparse observations in coastal regions. Scatterometers are at present the only satellite sensor capable of giving a wind direction as well as wind speed estimate (Liu, 2001). Conceived as an instrument for measuring open-ocean winds on large scales, the scatterometer has seen continuous improvement to its coverage and resolution of ocean surface winds and has been found to give useful data in coastal and enclosed sea areas (Nihoul et al., 1998). The primary role of high-resolution atmospheric models in the coastal regime is to satisfy the requirement for realistic representations of the wind field constrained by limited ship and satellite observations. As the resolution of Navy ocean models approach and/or exceed that of the satellites and atmospheric models that provide the wind data, there exists a need to assess the impact of satellite/model wind data on these ocean models.

The Fleet Numerical Meteorological and Oceanographic Center (FNMOC), Naval Oceanographic Office (NAVO) and the Naval Research Laboratory (NRL) have ongoing operational and research programs to provide the needed wind information in littoral regions that include high-resolution atmospheric models and real-time assimilation of satellite data (Burnett et al., 2002). A major component of NRL's ocean model program has been a detailed study of the resolution required for ocean prediction. NRL research

has demonstrated that a grid size of 8 km for each ocean model prognostic variable (mid-latitudes) is not unrealistic, and halving the grid size to 4 km provides substantial improvement (Metzger et al., 2001). Similarly, an atmospheric model study of the Penn State/NCAR Mesoscale Model Version 5 (MM5) suggested clear improvement in 10-m wind forecasts as grid spacing decreases from 36 to 12 km (Mass et al., 2002).

The focus of this study is on the wind-forced coastal ocean regime. This study examines the impact of variable atmospheric model resolution wind forcing and synthetic scatterometer data assimilation on a regional ocean model with a fixed resolution. The time period of this study is 07-21 January 1999 and real QuikSCAT data was not available until June 1999. The primary goals of this research are to evaluate: 1) The difference that high-resolution atmospheric model winds make for the coastal regions of a regional ocean model, and 2) The impact of synthetic scatterometer data on both the atmospheric models and ocean models with emphasis on the locations of the differences. A series of 14-day experiments are performed to evaluate the sensitivity of a regional ocean model to low (NOGAPS) versus high-resolution (COAMPS) wind forcing including scatterometer data insertion into COAMPS using synthetic QuikSCAT observations. Atmospheric model wind stress/wind stress curl and ocean model surface current results are compared and analyzed.

There is significant improvement (evaluated subjectively) with increasing atmospheric model resolution in producing realistic structures (e.g., expansion fans) in coastal areas with variable topography. The COAMPS runs provide more structure compared to NOGAPS and other COAMPS runs with increasing horizontal grid resolution. Quantitatively, the COAMPS wind stress and wind stress curl values are in agreement with previous research conducted with aircraft (Enriquez and Friehe, 1995). Atmospheric model comparisons to buoy data show good agreement with a tendency for NOGAPS and COAMPS to underestimate and overestimate wind stress amplitude, respectively with a small direction bias to the right of the real wind stress. The insertion of synthetic QuikSCAT data into the COAMPS 45 km numerical experiment produces a statistical difference, thought not significant, in wind stress, wind stress curl and ocean current. This result implies that higher spatial and/or temporal resolution (i.e., multiple

QuikSCAT satellites with improved sensors) may be required for the satellites to have a significant impact, or that the atmospheric model has sufficient skill in coastal areas using currently (i.e., DMSP SSM/I, etc) available observations.

The ocean model predictions have the expected climatological features and variability. In comparisons of model currents to ADCP buoys, the model currents usually underestimate observed current amplitude. Model current direction reflected the variability of CalCOFI data and increased with increasing atmospheric model resolution. Similarly, model currents had improved agreement with CODAR observations for higher resolution COAMPS experiments. In comparison to buoy data, the direction of the model currents often followed the offshore flow, sometimes in opposition to the observed direction. Thus, the offshore ocean features (e.g., California/Davidson Currents) in the model may mask the variability attributed to local wind forcing, bottom topography, baroclinic tides, transient coastal waves, and non- hydrostatic model physics. No comparison is made between COAMPS/NOGAPS wind forcasts and buoy observations to see that frontal propagaton in the models agree with reality. However, because this inertial time scale is approximately equal to the PWC 12-hour output, a systematic bias in frontal propagation speed of 12-24 hours may cause phase differences between buoy and model observations.

The "one size fits all" approach, in which all regions are run with the same resolution, may not be a good use of computer resources and the demonstrable benefits of increasing resolution may vary spatially and temporally. For example, fast moving storm and land-sea breeze systems and their associated winds cannot be sampled properly in both space and time. The along the coast is also difficult to sample. The consequence is that the multi-day composite ocean winds derived from satellites are not optimal for use in driving a high-resolution coastal ocean model. Thus, it is recommended that the Navy combine its current approach of developing relocatable, nested, high-resolution atmospheric (hon-hydrostatic) models with the development of multiple scatterometer satellite platforms and non-hydrostatic, nested ocean models capable of 1-10 km resolution.

THIS PAGE INTENTIONALLY LEFT BLANK

I. INTRODUCTION

A. PURPOSE

Current Navy sensor/prediction systems and tactics are heavily biased toward relatively homogeneous, deep-water areas where spatial and temporal variability are not dominant factors. As the focus of Navy attention shifts to littoral regions, higher resolution and re-locatable nested models have been developed to improve shallow-water operations. Numerical models of ocean circulation on the global scale (~ 1000 km) and geostropic eddies (~10 – 100 km) are accurately described by the hydrostatic primitive equations (HPEs). In the coastal environments, mesoscale oceanographic processes (~2-50 km horizontal space scales and 2-10 day time scales) over the continental shelf are mostly influenced by the variability of atmospheric forcing (Batteen, 1997). Deep mixing during the winter and inhibition of mixing by strong stratification during summer due to solar heating affects the density structure of the water coumn which as an effect on the coastal shelf circulation. Currently, most operational regional ocean models have horizontal scales of 1-10 km which represents the "grey area" in which the HPEs begin to break down (Marshall et al., 1997). For example, in conditions of weak stratification (winter) and small horizontal scales (i.e., convective scale ~ 1 km) the hydrostatic assumption may not be adequately satifsifed (Jones and Marshall, 1993). One of the scientific and technical challenges is to determine how much detail and accuracy in ocean wind data is needed to meet operational ocean prediction requirements for these regional coastal models.

Wind data from satellites and high resolution atmospheric models provide a wealth of high-resolution data to augment the historically sparse observations in coastal regions. The assimilation of Special Sensor Microwave Imager (SSM/I) data produces a more realistic ocean model circulation, especially in data sparse regions and areas of high variability (Rienecker et al., 1996; Phoebus et al., 1994; Busalacchi et al., 1993; Phoebus and Goerss, 1991). The SSM/I provides only wind speed, not direction. Scatterometers are at present the only satellite sensor capable of giving a wind direction as well as wind

speed estimate (Liu, 2001). Conceived as an instrument for measuring open-ocean winds, the scatterometer has seen continuous improvement to its coverage and resolution of ocean surface winds and has been found to give useful data in coastal and enclosed sea areas (Nihoul et al., 1998).

Due to long antenna wavelength, and relatively smaller swath widths, scatterometers have very low resolution (~25-50 km) compared to visible and infrared satellite instruments (~1-5 km). The operating wavelength is also a cause of potential land contamination which is a limiting factor for its use in close proximity to coastal regions (~25-50 km). A reliable interpretation of scatterometer data also requires first-guess wave spectra and/or wind data from other meteorological sources due to ambiguities in wind direction because of the sinusoidal relationship between the backscatter and wind direction. Finally, the inability of one satellite to sample any point more frequently than twice a day may also be a limitation on the operational impact of the sensor (Kramer, 1994).

High resolution ocean forecasts must be constrained by corresponding high resolution input measurements (Hutt, 2002). The primary role of high-resolution atmospheric models in the coastal regime is to satisfy the requirement for realistic representations of the wind field constrained by limited ship and satellite observations. FNMOC, Naval Oceanographic Office (NAVOCEANO) and NRL have ongoing operational and research programs to provide the needed wind information in littoral regions. Both programs include high-resolution atmospheric models and real-time assimilation of satellite data. A major component of NRL's ocean model program has been a detailed study of the resolution required for ocean prediction (Burnett et al., 2002). Recent research has demonstrated that a grid size of 8 km for each ocean model prognostic variable (mid-latitudes) is not unrealistic, and doubling the grid size to 4 km provides substantial improvement (Metzger et al., 2001). Similarly, the Navy's Coupled Ocean Atmosphere Mesoscale Prediction System (COAMPS) is being applied with horizontal grid spacing below 10 km. In the private sector, several companies are experimenting with high resolution atmospheric models such as the Penn State/NCAR Mesoscale Model version 5 (MM5). A recent study of the MM5 suggests a clear

improvement in 10-m wind forecasts as grid spacing decreases from 36 to 12 km (Mass et al., 2002).

High resolution atmospheric models like COAMPS are designed for circulations forced by topography and surface contrasts, especially in coastal areas where orographic flows or diurnal circulations are important. The surface layers of the ocean are dominated by turbulent mixing processes and the air-sea heat and momentum fluxes. Operationally, the bottom of the mixed layer often represents the surface maximum in the sound velocity profile. Diurnal circulations, and orographic wind flows that find passage to the sea, may cause changes to the mixed layer. The mixed layer leads to a surface duct which can drastically alter the propagation of high-frequency sound in the ocean. In addition, changes in current speed and direction can complicate search and rescue (SAR), mine countermeasure, and special warfare operations.

As the resolution of Navy ocean models approach and/or exceed that of the satellites and atmospheric models that provide the wind data, there exists a need to assess the impact of satellite/model wind data on these models. Historically, the major uses for satellite-derived wind vectors have been for global studies, dictated by the scatterometer repeat coverage and footprint size. Thus, nearly all of the research literature on the evaluation and application of scatterometer winds to ocean models has been restricted to open-ocean conditions (Legler and O'Brien, 1985; Large et al., 1991; Barnier et al., 1991 and 1994; Milliff et al., 1996 and 1999; Chin et al., 1998; Grima et al., 1999; Kelly et al., 1999; and Chen et al., 1999a, b). Most recently, the European Centre for Medium-Range Weather Forecasts (ECMWF) and FNMOC have begun assimilating scatterometer data operationally into their global atmospheric models. The focus of this study is on the wind-forced coastal ocean regime and will examine the impact of variable atmospheric model resolution wind forcing and synthetic scatterometer data assimilation on a regional ocean model with a fixed resolution.

B. OBJECTIVE

Recent evaluations (Hodur et al., 2002) have found clear benefit (e.g., COAMPS 27 km grid better represents maximum winds of the Mistral than 81 km grid) in increasing atmospheric model resolution in regions where orographic flows or diurnal circulations are important. Similarly, NRL research has shown that fine resolution (~10 km) is required to obtain dynamic coupoing between upper ocean currents and seafloor topography via flow instabilities (Rhodes et al., 2002). In most cases, increasing horizontal resolution produces better defined and more realistic structures. However, few studies have demonstrated quantitatively that accuracy increases with decreasing grid spacing (Mass et al., 2002). The primary objective of this research is to assist the Navy in quantifying its investment in space-based observations and air-ocean modeling. The primary goals of this research are to evaluate:

1) The impact of increasing atmospheric model horizontal resolution for the coastal regions of a regional ocean model.

2) The impact of synthetic scatterometer data on both the atmospheric and ocean models with emphasis on the locations of the differences.

The sensitivity of a Navy coastal ocean circulation model is conducted using atmospheric model low-resolution wind forcing, high-resolution wind forcing, and high-resolution wind forcing with synthetic scatterometer data assimilation from a single satellite. The period of this study is 07-21 January 1999 due to the availability of observational data for comparison to model results. QuikSCAT scatterometer data was not available until June 1999. Thus, synthetic scatterometer data is generated for the time period of this research. The ocean-atmospheric model configuration and experiment design are described in Chapter II. In Chapter III, the methods used to analyze the model data are discussed. The climatology and description of the physical environment are provided in Chapter IV. Chapters V and VI provide the atmospheric and ocean model results, respectively. Conclusions and recommendations are offered in Chapter VII.

II. EXPERIMENT DESIGN

A. OCEAN MODELS

The Navy's Pacific West Coast (PWC) model is based on the Princeton Ocean Model - POM (Blumberg and Mellor, 1987; Mellor, 1996). The POM has already exhibited the variability known to exist off the U.S. west and east Coasts (Allard et al, 1996; Aikman et al., 1995). Similar nested and fully automated high-resolution versions of the model have been implemented by FNMOC in other coastal regions (e.g., Mediterranean Sea, Persian Gulf, Red Sea and Adriatic Sea) of Navy interest (Horton et al, 1992, 1997; Clifford et al., 1997, Riedlinger, 1996; Clancy et al., 1996; Chu et al., 1997, 1998; Harding et al., 1996).

The PWC is a three-dimensional, 30 sigma layer, free surface model based on the primitive equations for momentum, salt, and heat. The model is configured on a 1/12 degree (~ 10 km horizontal resolution) spherical grid extending from the coast (116° W) to 135° W and 30° N to 49° N (Figure 2.1). Composite multi-channel sea surface temperature (MCSST) for surface heat forcing and monthly salinity climatology are provided by the Generalized Digital Environmental Model (GDEM). The monthly temperature and salinity climatology is used for lateral boundary conditions and relaxation of deep temperature and salinity to climatology. A filtered version of the Navy's Digital Bathymetric Data Base (DBDB5) provides ocean depths at oceanic geographic positions evenly divisible by 0.5 minutes of latitude and longitude. Depths shallower than 10 meters are considered land. Sources of fresh water include monthly varying climatological fresh water run-off from seven major rivers that drain into the domain. Turbulence closure is provided by the turbulence closure submodel developed by Mellor and Yamada (1982), while the Smagorinsky (1963) formula is used for horizontal mixing (Ezer and Mellor, 2000).

Since its development, there have been several changes to the PWC model code that include efforts to more tightly couple the lateral boundary conditions to the PWC interior and to reduce the error near steep topography (e.g., by subtracting the mean

density state prior to the calculation of the horizontal pressure gradient terms, Haney, 1991). Undesired diapycnal mixing due to the iso-sigma diffusion over steep topography is greatly reduced by subtraction of climatological temperature and salinity fields before the diffusion fluxes are calculated. The side effect of this formulation is a weak relaxation tendency toward the prescribed climatology on a timescale of ~20 years. With high enough resolution, recent experiments with POM have indicated that diffusion and relaxation towards climatology can be negligible (Ezer and Mellor, 2000).

The PWC is coupled to the NRL Layered Ocean Model (NLOM) with a nudging/relaxation scheme for boundary conditions along the northern, southern and western boundaries. NLOM is a multi-layer, free surface, hydrodynamic primitive equation ocean model with full-scale bottom topography in the lowest layer (Hurlburt and Thompson, 1980; Wallcraft, 1991). The NLOM model region can be any closed geometry and has a uniform model grid that can be on a beta-plane, f-plane or on the surface of an earth-sized sphere. A horizontal grid with a resolution of $1/8^{th}$ to $1/16^{th}$ of a degree provides for the inclusion of externally forced events such as upstream variations of the California Current and Kelvin waves excited along the Pacific West Coast south of the model domain and in the equatorial regions. In 1998, the NLOM model providing the boundary conditions was switched from a global 5 ½ layer (reduced-gravity version) model to a global 6-layer finite depth model.

NLOM is forced by 6-hourly wind stress fields produced at FNMOC. TOPEX/Poseidon and ERS-2 altimeter data, produced daily at the NRL Stennis Altimeter Data Fusion Center (ADFC), are sent to FNMOC where they are assimilated into the NLOM using the optimum interpolation (OI) of Sea Surface Height (SSH). The vertically averaged PWC current velocities are nudged on a time scale of 10 minutes over an e-folding distance of five PWC gridpoints into the PWC domain from the open boundaries to match those calculated from NLOM. The vertical shapes of the PWC velocity profiles are unconstrained by the global model and determined purely by PWC dynamics. Along the open boundaries, a radiation boundary condition is applied to the velocities normal to the boundaries. The temperature and salinity values on the open boundaries are obtained from an advection scheme with inflow values for temperature

and salinity taken from seasonal climatology. The PWC sea surface elevation, spatially averaged over the PWC domain, is forced to match the spatial average of the global model over the same domain.

B. ATMOSPHERIC MODELS

Ocean circulation model wind forcing is provided by the Navy Operational Global Atmospheric Prediction System (NOGAPS) and the Coupled Ocean-Atmospheric Mesoscale Prediction System (COAMPS). NOGAPS is a global spectral model (GCM) consisting of 160 spectral waves and 18 vertical levels to 10 mb. The vertical coordinate is a hybrid system that follows the terrain at low levels and contains pressure surfaces at upper levels. Model physics include long-wave and short-wave radiation, boundary layer processes, and stable and convective cloud and precipitation parameterization (Hogan and Rosmond, 1991; Rosmond, 1992 and Rosmond et al., 2002). In this study, NOGAPS forcing drives NLOM and provides boundary and initial conditions for COAMPS.

COAMPS was developed by the Naval Research Laboratory (Hodur, 1993,1997) based on the Klemp and Wilhelmson (1978) atmospheric model. Operational at FNMOC since July 1998 (Hodur et al.,1998, 2002), COAMPS is a 3-D, limited area, relocatable, multi-nested, non-hydrostatic model composed of an objective analysis scheme incorporating data quality control (Baker, 1992; Barker, 1992), and a multivariate optimum interpolation (MVOI) analysis (Baker, 1992; Goerss and Phoebus, 1992). COAMPS includes predictive equations for momentum, the non-dimensional pressure perturbation, the potential temperature, and mixing ratios of water vapor, clouds, rain, ice and snow. In this study, the MVOI analysis in COAMPS is replaced by two-dimensional multiquadric interpolation (Nuss and Titley, 1994).

For initialization and the required lateral boundary conditions, COAMPS is designed for nesting within NOGAPS. The nesting is accomplished by imposing NOGAPS fields on the outer gridpoints of the outermost COAMPS grid in a one-way interactive mode. The grid spacing is reduced by a factor of three between each nest that allows the COAMPS grid to telescope down to resolutions of less than 10 km in areas

that require high resolution. In this study, the COAMPS domain is located over the western U.S. from 90°W to 165°W longitude and 10°N to 65°N latitude (Figure 2.1).

C. NUMERICAL EXPERIMENTS

1. Atmospheric Models

The PWC model uses wind stress for atmospheric forcing. The winter period of 07-21 January 1999 was selected for this study based on the availability of verification field data and the atmospheric wind variability provided by the passing of winter weather systems through the model domain. Five ocean numerical experiments are conducted for a different time period using wind stress forcing supplied by NOGAPS and COAMPS with variable horizontal grid spacing. Two additional COAMPS-45 km grid runs are conducted to compare the impact of the assimilation of real versus synthetic QuikSCAT observations (Table 2.1).

Table 2.1 Numerical Experiments

RUN	MODEL	TIME	FORCING
1	PWC	07-21 January 1999	NOGAPS - 1.25 degree grid
2	PWC	07-21 January 1999	COAMPS - 45 km grid
3	PWC	07-21 January 1999	COAMPS – 25 km grid
4	PWC	07-21 January 1999	COAMPS – 10 km grid
5	PWC	07-21 January 1999	COAMPS – 45 km grid (with synthetic QuikSCAT)
6	COAMPS 45 km	30 January 2000	Real QuikSCAT
7	COAMPS 45 km	30 January 2000	Synthetic QuikSCAT

The first four numerical experiments study the impact of variable atmospheric model wind forcing on a high resolution ocean model. The hypothesis is that increased wind field resolution will result in higher quality ocean forecasts by producing more realistic ocean structure in the coastal regions. To reduce computation time, in experiment four, the COAMPS 10 km grid is nested within a 30 km outer grid. The 30 km grid covers the entire PWC domain while the 10 km grid covers a smaller area (30° N to 49° N from the coast to 130° W). The fifth experiment includes the assimilation of synthetic scatterometer winds into the 45 km COAMPS grid used in experiment two. The hypothesis for experiment five is that the introduction of higher resolution scatterometer winds to a coarser COAMPS grid will result in an improved forecast and more wind structure detail in coastal areas. Experiments six and seven are used for a comparison of the impact of synthetic QuikSCAT versus real QuikSCAT data on a coarser grid atmospheric model (i.e., COAMPS 45 km). A COAMPS analysis and eight forecasts dumped every three hours are generated twice a day (0000 UTC and 1200 UTC) for the 14-day study period resulting in 252 atmospheric model output files for each of the five experiments (for a total of 1260). The three-hourly NOGAPS wind stress data are provided by FNMOC on a Mercator grid, whereas COAMPS generates wind stress data using a Lambert conformal grid. For each experiment, the three-hourly NOGAPS/COAMPS wind stress data are interpolated to the 1/12 degree (~10 km) PWC model Mercator grid using an Akima spline.

A COAMPS run is initiated from a cold start using NOGAPS for outer boundary conditions and an analysis in which irregularly-spaced, quality controlled data (e.g., radiosondes, aircraft, satellite, ships, etc.) are interpolated to the model's regularly-spaced grid using multiquadratic interpolation. There is no coupling to the ocean model and SST data taken from NOGAPS remains constant for the analysis and entire 24-hour forecast period. An analysis of COAMPS three, six and nine-hour forecasts indicate that dynamic adjustment is reached within three to six hours. Table 2.2 shows an example of COAMPS wind stress input for 08 January 1999. Note that the COAMPS model does not produce wind stresses for the 0000 UTC or 1200 UTC analyses. As a result, the

three-hour forecast (0300 and 1500) is used for the (0000 and 1200, respectively) UTC inputs to PWC.

Table 2.2. COAMPS Wind Stress Input

08/00 Analysis	Not used – steady state reached at 08/0300 hour forecast
08/03 Hour Forecast	08/0000 & 08/0003 UTC wind stress input to PWC
08/06 Hour Forecast	08/0600 UTC wind stress input to PWC
08/12 Hour Forecast	08/1200 UTC wind stress input to PWC
08/12 Analysis	Not used – steady state reached at 08/1500 hour forecast
08/15 Hour Forecast	08/1500 UTC wind stress input to PWC
08/18 Hour Forecast	08/1800 UTC wind stress input to PWC
08/24 Hour Forecast	09/0000 UTC wind stress input to PWC

2. Ocean Model

The ocean modeling system used in this study reflects the operational structure currently in place at NAVOCEANO that consists of a global ocean model (NRL Layered Ocean Model - NLOM) and nested regional ocean model (NRL Coastal Ocean Model - NCOM). In this study, the PWC model serves as the regional model because NCOM was not available until 2000 – one year after the initiation of this research. The PWC model is strictly a sigma coordinate model, whereas NCOM (also based on POM) offers a choice of sigma layers or z-levels, or some combination with sigma layers in shallow water and z-levels in deeper water (Rhodes et al., 2002).

As in the current operational system, there is one-way interaction (NOGAPS/COAMPS wind stress to ocean model) between the atmospheric and ocean models. The ocean data assimilation component of COAMPS for coupling to the existing atmospheric component is now under development at NRL (Hodur et al., 2002). The PWC ocean model grid remains constant (~10 km) for the five numerical experiments. Ocean model spin-up is from January 1992 to January 1999. Each day of the 14-day model runs (period of 08-21 January 1999) uses the previous day's output of current,

temperature, salinity and SSH for startup. SSH and SST are input on a daily basis and there is no interaction with the atmospheric models for heat flux. In the absence of significant precipitation or evaporation, salinity can only be changed in near coastal regions by upwelling/downwelling events and fresh water input from the seven rivers in the PWC model. Data files of PWC temperature, salinity, SSH and current velocity are produced every twelve hours (0000 UTC and 1200 UTC) for a total of 140 ocean model data sets per variable over the 14-day study period.

3. Scatterometer Winds

a. Background

There is extensive research on the sampling characteristics of microwave polar-orbiting satellites (Guymer and Zecchetto, 1991; Lee and Boyle, 1991; Halpern et al., 1994; Boutin et al., 1996; Kent et al., 1998; and Wang et al., 1998). Legler and O'Brien (1985) examined the sampling problems of the scatterometer and methods of assimilation into large-scale atmosphere and ocean models. Their results illustrated the importance of errors resulting from the application of assimilation schemes on scatterometer data. Large et al. (1991) illustrated the aspects of general circulation model sensitivity to high-frequency components in the wind forcing. Barnier et al. (1991) forced a quasi-geostrophic model of an idealized double-gyre ocean basin with combinations of wind stress curl from weather center analyses and simulated scatterometer wind stress curl derived from weather center analyses. Their study concluded that scatterometer winds seem appropriate for providing forcing to mid-latitude ocean models and may not require prior assimilation into meteorological models despite their patchiness and irregular resolution. Barnier et al. (1994) used scatterometer winds to drive a primitive equation model of the Indian Ocean to study the impact of irregular sampling. Milliff et al. (1996) demonstrated that circulation patterns and energetics of a quasi-geostrophic model is sensitive to the high wavenumber spectral content in scatterometer wind data. Chin et al. (1998) developed numerical techniques to capture these wavenumber characteristics to transform the band-like sampling of

scatterometer data into regularly gridded wind fields required by ocean general circulation models. Grima et al. (1999) and Milliff et al. (1999) conducted sensitivity studies of general ocean circulation models forced by satellite wind stress fields and determined that they are particularly efficient in capturing abrupt changes (e.g., wind bursts) that may be important in ocean dynamics. Finally, Kelly et al. (1999), and Chen et al. (1999a; 1999b) used scatterometer observations to study their impact on improving tropical ocean modeling and El Niño prediction.

NASA launched a Ku-band scatterometer, QuikSCAT, in 1999 to fill the gap created by the loss of data from the NASA scatterometer (NSCAT) onboard the Advanced Earth Observing Satellite (ADEOS) in 1997. Although the satellite platform shares similar orbital parameters with ERS-2, the QuikSCAT scatterometer conical scan has a continuous 1800 km swath that covers 93% of the global ocean in a single day with 25 km gridpoint separation. The ERS2 (1996) satellite with a C-band (5.3 GHz) scatterometer, a 500 km swath (side scan), and 50 km spatial resolution, provides winds over 41% of the global ocean daily. In conjunction with an orbital period of 101 minutes, ERS2 yields a 2800 km track separation distance of adjacent orbits at the equator. This results in ERS2 data that is four hours outside the COAMPS 0000 UTC and 1200 UTC analysis windows and that is inadequate for coastal coverage in the PWC domain (Figure 2.3). The QuikSCAT footprint reduces the satellite track separation at the equator by 36% to approximately 1000 km and provides the required nodal crossing times, spatial and temporal coverage of the PWC domain for the period of interest (Figure 2.4).

b. Synthetic Scatterometer Winds

The fifth experiment run uses 25 km resolution QuikSCAT synthetic scatterometer wind stress as input to the COAMPS Model on a 45 km grid. Since QuikSCAT data was not available until June 1999, synthetic QuikSCAT winds were generated using software provided by the Aerospace Corporation (Stodden and Galasso, 1996, this software is used by the United States Air Force space program). The position and velocity of a satellite at a particular time are calculated from user-defined initial

conditions using embedded propagation algorithms. The satellite's initial condition (IC) consists of a set of six orbital parameters and an epoch date. Four of these parameters determine the temporal and spatial sampling characteristics of a satellite: inclination, eccentricity, altitude, and repeat period (Verron, 1990; Verron and Cloutier, 1996; Parke et al, 1987). When these and the constants describing Earth's gravity are known, the prediction of position and velocity is a function of elapsed time. This determines a time sequence by which independent ground tracks within the repeat period are filled in, together with the angle between crossing ground tracks (i.e., ascending and descending tracks). The Satellite Orbital Analysis Program (SOAP) contains a full package of orbital physics (Stewart, 1994) and uses orbital parameter values generated by the North American Defense Command (NORAD) to reproduce the sampling characteristics of the QuikSCAT satellite.

The COAMPS 25 km wind stress fields are used to create the QuikSCAT synthetic data because they approximate the resolution of QuikSCAT observations and have similar errors (~ +/- 20 degrees in wind direction and 1.4 m/s and 2 m/s in wind speed for QuikSCAT and COAMPS, respectively). The SOAP software generates ground tracks and subsatellite points with the required 25 km separation along the satellite heading. Using each subsatellite position as a node, 72 satellite swath points are symmetrically created around the node on a line perpendicular to the satellite heading. The 72 swath points have a 25 km separation and produce a 1800 km synthetic QuikSCAT swath. All distance, longitude and latitude values are calculated using the World Geodetic System ellipsoid of 1972 and geospacial formulas contained in the American Practical Navigator (Bowditch, 1995). COAMPS 25 km wind stress data are matched to the synthetic track points by the "nearest neighbor" method and inserted into a 45 km COAMPS domain as observations using a plus/minus time window of 2.5 hours around the analysis times of 0000 UTC and 1200 UTC (Figure 2.2).

Real satellite data contain many types of error including biases, correlated errors and gross errors due to transmission. In some cases, it is difficult to anticipate specific types of error before a satellite system is really operational. For example, no rain contamination or instrument errors are added to the synthetic wind stress. Real

QuikSCAT data sets have rain flags attached (Draper and Long, 2002) that filter out a significant number of data points. These flags are derived from two algorithms that determine the rain rate and are set to "on" in regions where a NWP model has forecast significant (rain rate > 2 km*mm/hr) cloud/rain amounts. (The rain flag algorithms are more fully described in the documentation on the NASA QuikSCAT web site (http://podaac.jpl.nasa.gov/quikscat).

The synthetic QuikSCAT observations are obtained by using "temporally static" COAMPS wind stress fields that comprise a "snapshot" of the entire COAMPS domain during each transit period. During real QuikSCAT data acquisition, there are continuous changes in the wind field occurring forward, beneath and behind the satellite footprint. This is a potential source of error that is not accounted for in the synthetic data. In this study, synthetic data is not filtered using rain flags and observations are removed that contain land values, light winds (< 5m/s), and points falling outside the COAMPS 2.5-hour analysis window. In recent studies of errors in coastal winds measured by QuikSCAT, the removal of light winds (< 5 m/s) from the satellite data provided the most improvement, whereas the removal of rain flagged satellite data provided the least (Pickett and Wenqing, 2001).

In order to evaluate whether the synthetic scatterometer data is overly optimistic and/or substantially different than later obtained in operations, two 45 km domain COAMPS runs are performed (See Table 2.1) using real and synthetic QuikSCAT winds. The runs are initialized at 0000 UTC for 30 January 2000 for a 24 hour period ending 0000 UTC 31 January 2000 using a COAMPS 45/15/5 km nested configuration. This time period corresponded to a good wind case (i.e., storm passage) in January 2000. The first run assimilates real QuikSCAT data into a COAMPS 45 km grid. The second run uses synthetic QuikSCAT winds generated from a COAMPS 25 km grid. Figure 2.3 is an example of real versus synthetic QuikSCAT winds for 29 January 2000. Note the real QuikSCAT (Figure 2.3a) data void within ~50 km of the coast (e.g., Monterey Bay to Canada) due to the removal of land contaminated observations. In addition, there is a 200 km lag between the synthetic and real QuikSCAT swaths (Figure 2.3). In a real space environment, the Earth's gravity field and atmosphere drag cause

perturbations in the QuikSCAT orbit that is not accounted for in satellite simulations which results in a position offset between real and simulated QuikSCAT satellites. Figures 2.4 and 2.5 highlight the 12-hour forecast surface stress results of experiments six and seven for 30 January 2000. Note that there are no significant differences between the synthetic and real QuikSCAT runs for 30 January 2000.

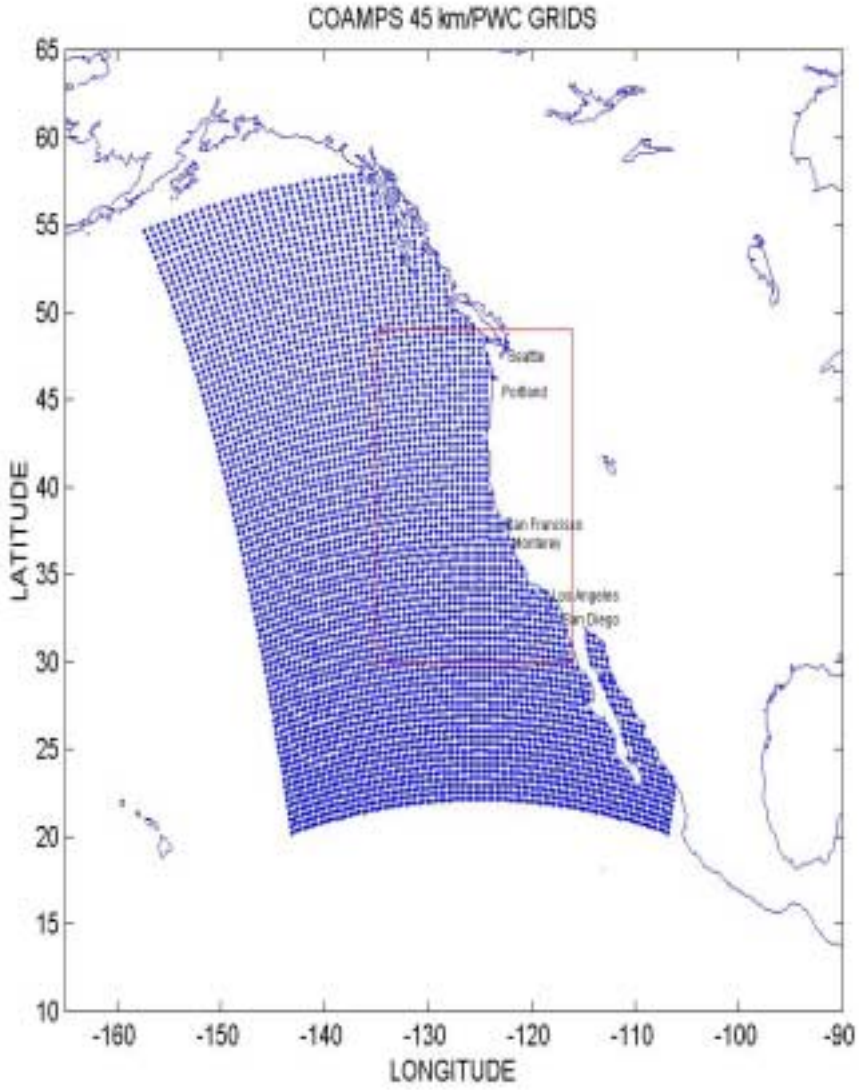

Figure 2.1. COAMPS/PWC domains.

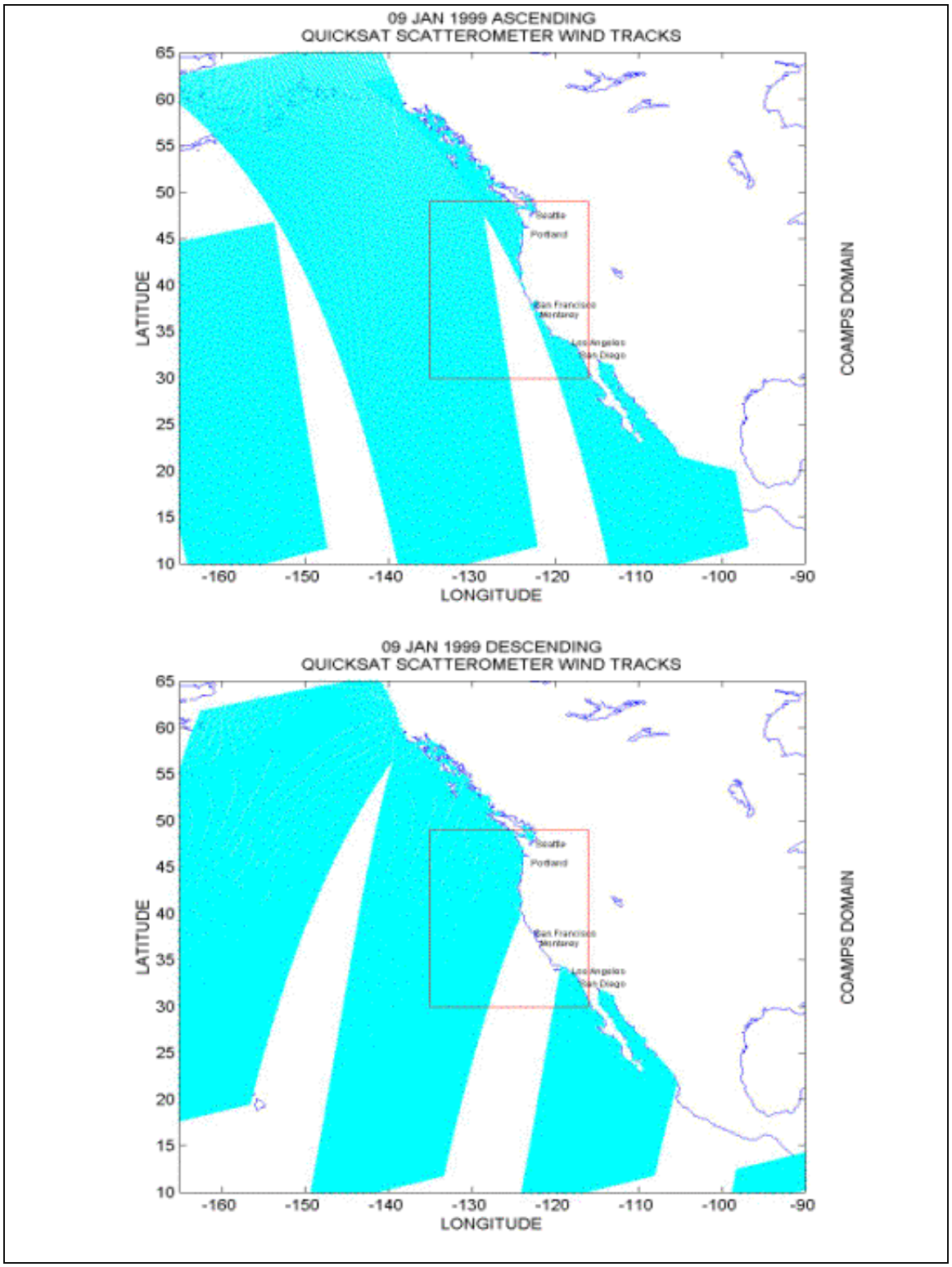

Figure 2.2. 09 January 1999 synthetic QuikSCAT swaths.

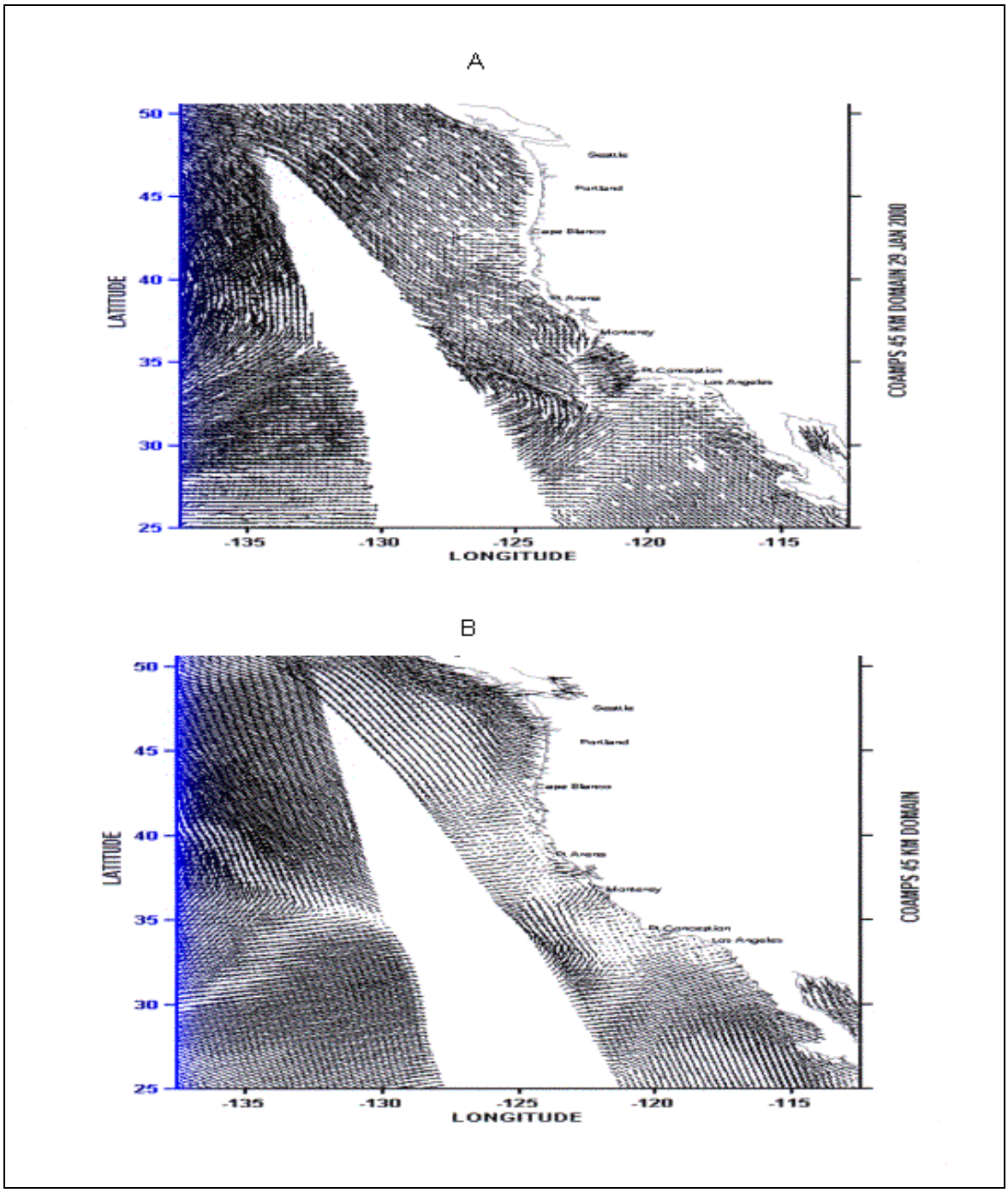

Figure 2.3. (A) Real and (B) synthetic QuikSCAT winds for 29 January 2000.

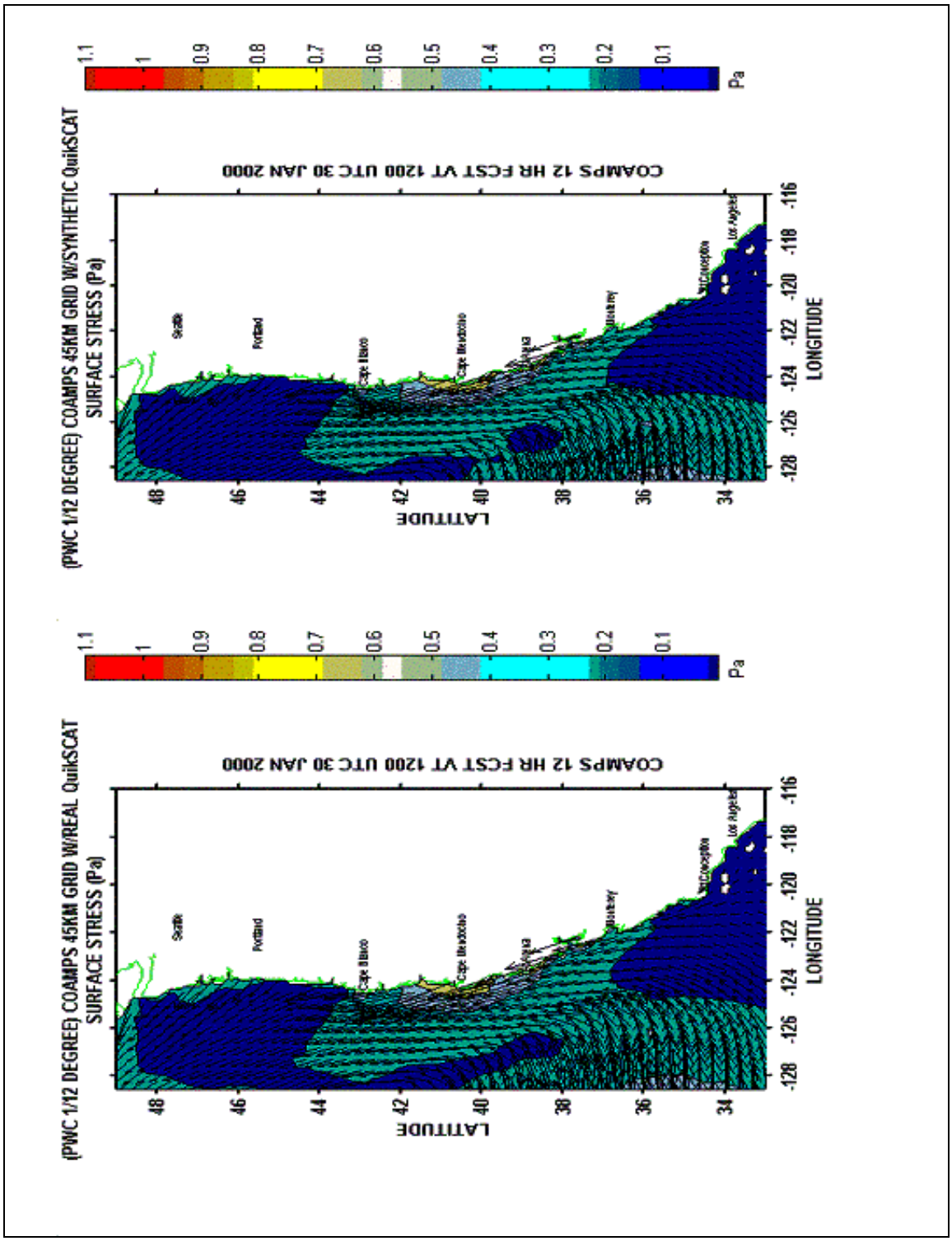

Figure 2.4. Real/synthetic QuikSCAT winds (1200 UTC 30 Jan 2000).

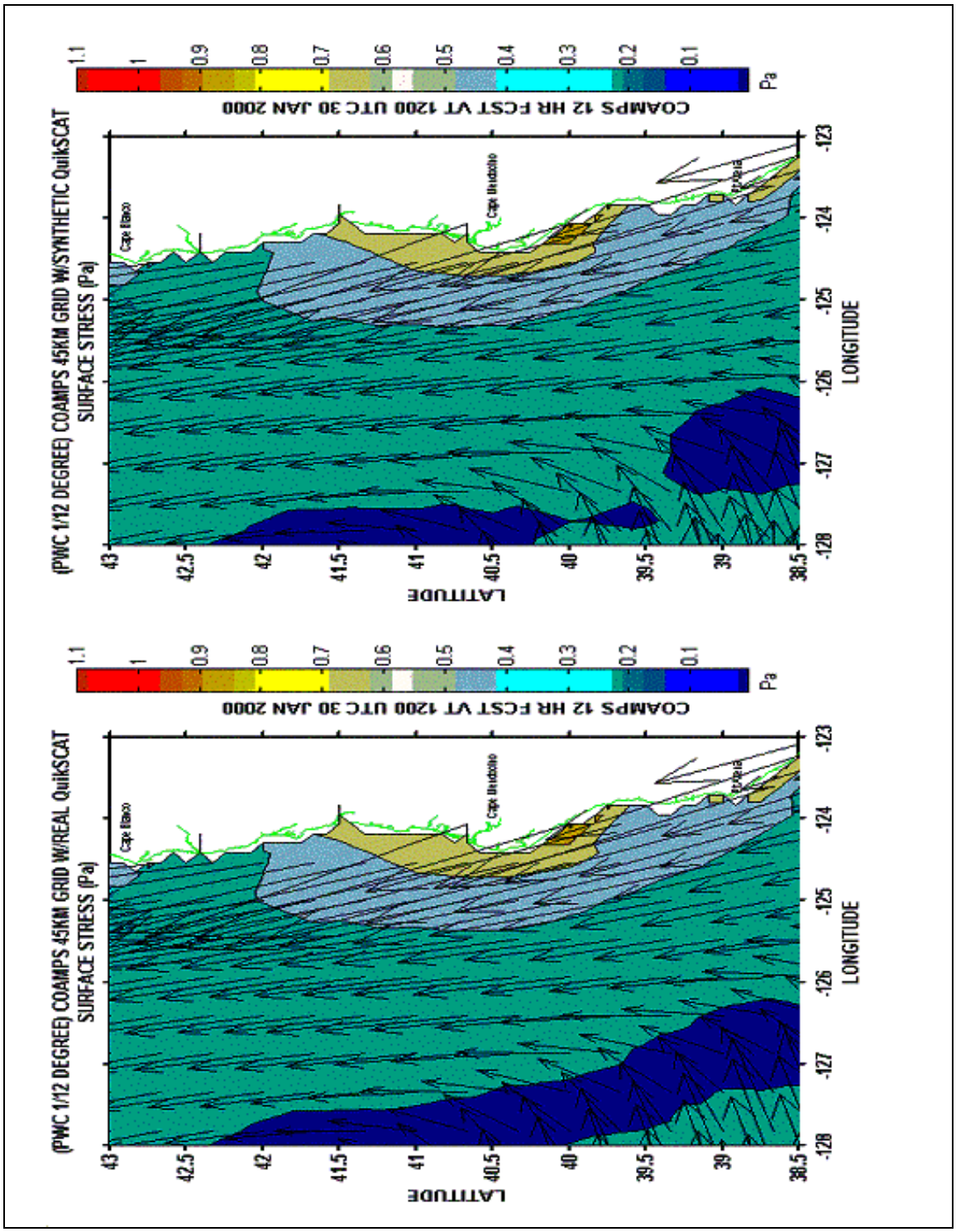

Figure 2.5. Same as Figure 2.4, except for Cape Mendocino.

III. DATA ANALYSIS

The focus of this research is on the forecast accuracy of a regional ocean model for coastal ocean currents with increasing horizontal resolution of the atmospheric forcing. This is accomplished through a comparison of the atmospheric/ocean model runs using statistical analysis and observational field data.

A. STATISTICAL METHODS

1. Accuracy measures

Mean Error (ME) and Root Mean Square Error (RMSE) are standard measures of error and model forecast skill. For "between model" run comparisons, the Student's t-test and Analysis of Variance (ANOVA) are used in quantifying significant statistical differences. Mean Error (ME) is the difference between the average forecast and average observation:

$$ME = \frac{1}{n}\sum_{k=1}^{n} FE = \bar{y} - \bar{o} \tag{3.1}$$

where $FE = (y_k - o_k)$ is the forecast error and (y_k, o_k) is the kth of n pairs of forecasts and observations. The ME expresses the bias of the forecasts. Forecasts that are on average too high will exhibit ME > 0 while forecasts that are on average too low will exhibit ME < 0. The root mean square error (RMSE) also has the same physical dimension as the forecasts and observations :

$$RMSE = \sqrt{MSE} \tag{3.2}$$

where the Mean-Squared Error (MSE) is the average squared difference between the forecast and observation pairs:

$$MSE = \frac{1}{n}\sum_{k=1}^{n}(y_k - o_k)^2 \tag{3.3}$$

MSE increases from zero for perfect forecasts through larger positive values as the discrepancies between forecasts and observations become increasingly large. ME and RMSE is calculated for the comparison of model and buoy observations.

2. Student t-test and Analysis of Variance (ANOVA)

The t-test statistic is given by:

$$z = \frac{\bar{X}_1 - \bar{X}_2}{\left[\left(S_1^2 + S_2^2 - 2\rho_{1,2}S_1S_2\right)/n\right]^{1/2}} \tag{3.4}$$

where ρ is the Pearson correlation between the model domain space means $\bar{X}_1$ and $\bar{X}_2$. ANOVA is the square of the t-test statistic (z^2) and provides a measure of the strength of data regression (F-ratio = regression sum of squares/MSE). For independent samples, ρ = 0. Atmospheric/ocean data often do not satisfy the independence assumption (e.g., serial correlation, persistence) which can lead to an underestimate of the variance and an inflated value of the test statistic. However, the effect of serial correlation in the data can be properly represented either using an "effective" sample size to determine sample variance for equation 3.4, or by using large sample sizes (Wilkes, 1995; Emery and Thomson, 1998). In this study, atmospheric (three-hourly) and ocean (12-hourly) samples of the entire domain (n>greater than 30,000) are used in the statistical analyses.

The null hypothesis determines if there is a significant difference in the mean of the distribution of a prognostic variable (i.e., current, temperature, SSH, etc.) between two model runs. In this study, the null hypothesis is that the sampling distribution <u>is not the same</u> for the PWC ocean model runs due to variable NOGAPS/COAMPS wind forcing. The same null hypothesis is used for the comparison between the COAMPS 45

km/COAMPS 45 km (without scatterometer) runs. Parametric tests such as the Student's t-test and ANOVA (F-distribution) assume that the study samples come from normally distributed populations. The Student's t-test is considered a 'robust' method in that it can give good results when the study sample populations are not normally distributed. In the central limit theorem, it is assumed that large sample sizes (n > 30) approach a Gaussian distribution (A detailed treatment of these statistical methods is provided by Wilks, 1995).

3. Empirical orthogonal functions (EOF)

EOF analysis is perhaps the most useful for screening multivariate data. EOFs identify patterns that maximize the variance in a field by exploring the joint space/time variations of the variables in the data set (i.e., currents, temperature, etc). The data from these locations at a given observation time are arranged in a one-dimensional vector where each location is assigned a number from 1 to K, and the data matrices [X] and data anomalies [X´] are dimensioned (n x K) or (time x space). The *m*th EOF is obtained as the projection of the data vector **X'** onto the *m*th eigenvector where ***m* = 1…..M.** Each of the **M** eigenvectors contains one element pertaining to each of the K variables, $x_k^{'}$. In this study, K ~ 25,000 model gridpoints and M = 14 observations (days). For **n** observations, there will be **n** values **(n = K)** for each e_{km} where **M < n**:

$$u_m = u_m(t) = e_m^T x' = \sum_{K=1}^{K} e_{Km} x_K' \qquad (3.5)$$

Each eigenvector element can be plotted on a map at the same location as its corresponding data value and displayed with smooth contours. These maps (current speed, SST, SSH) depict clearly which locations are contributing most strongly to the respective EOF components. Modes 1 and 2 (m=1,2) usually contain the most variance. The maps also represent uncorrelated modes of variability of the field (i.e., currents, temp, etc.) from which the EOF was extracted (Lorenz, 1956; Harms and Winant, 1998; Frankignoul and Duchene, 1989; Von Storch and Frankignoul, 1998; Wunsch, 1996). (A detailed discussion of EOF computations is provided by Emery and Thompson,1998).

4. Autocorrelations and Crosscorrelations

Two-dimensional plots (buoy and PWC current velocity) and geographical plots (PWC current velocity) of autocorrelations are computed by substituting lagged data pairs into the formula for the Pearson correlation:

$$r_k = \frac{\sum_{i=1}^{n-k} \left[(x_i - \overline{x}_-)(x_{i+k} - \overline{x}_+) \right]}{\left[\sum_{i=1}^{n-k} (x_i - \overline{x}_-)^2 \sum_{i=k+1}^{n} (x_i - \overline{x}_+)^2 \right]^{1/2}} \tag{3.6}$$

where Equation 3.6 is the autocorrelation function and the subscripts "-" and "+" indicate sample means over the first and last n-k data values, respectively. The lags (k) are computed for 12, 24, 36 and 48 hours. For wind stress data, autocorrelation coefficients greater than or equal to 0.195 (5% level) and 0.254 (1% level) are considered significant for 107 degrees of freedom (N-2). "N" equals 109 three-hourly wind stress observations. For current speed, coefficients greater than or equal to 0.374 (5% level) and 0.478 (1% level) are considered significant for 26 degrees of freedom and "N" equals 28, 12-hourly observations of surface current speed. Geographical plots of crosscorrelations (wind stress/surface current) are computed by the formula using the Pearson correlation:

$$r_k = \frac{\sum_{i=1}^{n-k} \left[(x_i - \overline{x}_-)(y_{i+k} - \overline{y}_+) \right]}{\left[\sum_{i=1}^{n-k} (x_i - \overline{x}_-)^2 \sum_{i=k+1}^{n} (y_i - \overline{y}_+)^2 \right]^{1/2}} \tag{3.7}$$

where Equation 3.7 is the cross-correlation function that determines how well wind stress "y" and surface current velocity "x" linearly co-vary in time or in space. For current speed, crosscorrelation coefficients greater than or equal to 0.374 (5% level) and 0.478 (1% level) are considered significant. The "integral time scale" can be derived from the correlation function as follows:

$$T^{*} = \frac{\Delta\tau}{2}\sum_{i=0}^{N'}\left[r(\tau_i) + r(\tau_{i+1})\right] \tag{3.8}$$

where $N' < N$ and τ = lag time step. The integral time scale T^* gives a measure of the dominant correlation time scale within or between a data series. For times longer than T^*, the data become decorrelated. (See Emery and Thompson (1998) and Wilks (1995) for a detailed discussion.)

B. WIND STRESS CURL, VORTICITY AND EKE

1. Wind Stress Curl

The method of Enriquez and Friehe (1995) is used to calculate the vertical component of the curl of the wind stress:

$$(\nabla x\tau)_z = \frac{1}{R\cos\varphi}\left[\frac{\partial\tau_y}{\partial\lambda} - \frac{\partial}{\partial\varphi}(\tau_x\cos\varphi)\right] \tag{3.9}$$

where R is the radius of the earth, λ and φ are geographic latitude and longitude, respectively, and τ_x and τ_y are the eastward and northward components of the surface stress provided by NOGAPS and COAMPS interpolated to the PWC grid. A finite-difference scheme is then applied, such that for grid point (i,j), the vertical component of the curl that includes the curvature of the surface of the earth is given by:

$$(\nabla x\tau_{i,j})_z = \frac{1}{R\cos\varphi_{i,j}}\left[\frac{(\tau_y)_{i+1,j} - (\tau_y)_{i-1,j}}{2\Delta\lambda} - \frac{(\tau_x\cos\varphi)_{i,j+1} - (\tau_x\cos\varphi)_{i,j-1}}{2\Delta\varphi}\right] \tag{3.10}$$

2. Vorticity

The dynamics of the regional ocean circulation can often be diagnosed in terms of vorticity that can be used to determine divergence and ultimately vertical velocities. The vertical component of relative vorticity is given by:

$$\xi = \frac{\partial v}{\partial x} - \frac{\partial u}{\partial y} \tag{3.11}$$

For the ocean model, a finite-difference grid scheme using the mid-point between u and v components is applied to the PWC Arakawa C grid to calculate relative vorticity:

$$\xi_{i,j} = \frac{V_{i,j} - V_{i-1,j}}{dx_j} - \frac{U_{i,j} - U_{i,j-1}}{dy_i} \tag{3.12}$$

3. Eddy Kinetic Energy (EKE)

EKE in the PWC model at the ocean surface at each grid point by subtracting a time-mean from the current velocity components:

$$EKE = \frac{1}{2}\left[(u')^2 + (v')^2\right] \tag{3.13}$$

$$u' = u - \overline{u}$$

$$v' = v - \overline{v}$$

where the depth-integrated mean of the current velocity component is:

$$(\overline{u}, \overline{v}) = \frac{1}{\sigma}\int_{\sigma}^{0}(u, v)d\sigma \tag{3.14}$$

The coordinate σ (sigma) is the vertical coordinate. To achieve the highest resolution in coastal (shallow water) areas, the vertical mean flow is calculated using sigma coordinates. In the PWC ocean model, sigma is defined:

$$\sigma = \frac{z - \eta}{H + \eta} \tag{3.15}$$

where H(x,y) is the bottom topography, η is the sea surface elevation, H +η = total depth and σ = -1 at depth = H.

C. FIELD DATA

1. Cruise Data

The period of this study was selected to take advantage of the hydrographic data collected during a California Cooperative Fisheries Investigations (CalCOFI) Central California cruise between 06 and 20 January 1999. Using a Seabird 911 plus conductivity, temperature and depth (CTD) instrument, the Research Vessel Point Sur performed 159 CTD casts and 101 XBT drops along with continuous wind observations and Acoustic Doppler Current Profiler (ADCP) data collection. The ship's track was designed to maximize cross-shore measurements (Figure 3.1). The ADCP measurements start at 20 m depth with a maximum depth of 412 m. CTD and XBT data collections start at 1 m depth with a 1 m separation between levels.

2. CODAR

High frequency radar measurements are useful for quantifying tidal flow patterns, submesoscale eddies, coastal buoyancy currents, and estuarine-shelf exchange processes (Haus et al, 1997). Shore-deployed Coastal Ocean Doppler Radar (CODAR) measure surface currents in the radial direction over a limited area using microwave energy backscattered by surface waves. NOAA operates two high frequency (HF) radar sites on the shore of Monterey Bay, one near the center of the Bay at Moss Landing, and one at the southern end of the bay at Pacific Grove (Figure 3.2). These instruments are of the CODAR design and provide useful coverage to ~22 km offshore (Neal,1992). The CODAR system computes the surface current velocity with a horizontal range resolution

of 2 km and RMS errors of +/- 2 to 3 cm/s. (A detailed discussion of the utility of CODAR measurements to observe two-dimensional current fields is provided by Paduan and Rosenfeld,1996; Paduan and Cook, 1997; Haus et al., 1997; and Nuss et al., 1998).

3. Moored Buoys

Atmospheric and /ocean model output is also compared to field data using wind and ocean surface/subsurface current velocity data from moored buoys and scientific cruises. For comparison to buoy observations, atmospheric and ocean model fields are matched to individual NOAA buoys using the nearest neighbor method. Because PWC grid spacing is 10 km, only those buoys that are less than 10 km from the nearest COAMPS/NOGAPS grid points are used for the scalar accuracy comparisons.

The National Data Buoy Center (NDBC) maintains an array of moored buoys on the Pacific West Coast (Figure 3.3). The parameters reported include wind speed and direction. For model-to-observation comparisons, the wind speed data from twenty-three buoys (See Appendix A, Table A.1) is converted to wind stress using the method of Large and Pond (1981). Continuous wind measurements are six 10-minute average values of wind speed (m/s) and direction (in degrees clockwise from North) reported each hour. NDBC also uses Acoustic Doppler Current Profilers (ADCP) to measure current velocity from a limited number of stations. Currently, three NDBC stations measure ADCP data: stations 46023 (Point Conception, CA), 46054 (Santa Barbara, CA) and 46062 (Point San Luis, CA). Data are in the form of both eastward and northward current velocities for 20 depth levels. The first level occurs at 25 m depth and the last at 329 m depth with a 16 m separation between levels (See Appendix A, Table A.2).

The Monterey Bay Aquarium Research Institute (MBARI) operates three moorings to obtain weather and oceanic data in Monterey Bay (Figure 3.2). The M1 and M2/M3 moorings are located in 1000 and 1800 m of water depth, respectively. The nearshore M1 mooring lies in the path of a persistent upwelling plume and is sensitive to changes in the upwelling regime. The offshore M2 mooring lies at the eastern margin of the California Current. M3 is located near the mouth of Monterey Bay. Buoy

deployments are an ATLAS-like mooring at the M2/M3 sites and a PROTEUS-like mooring at M1. The primary difference between ATLAS and PROTEUS is that the latter has a four leg tower and bridle to accommodate deployment of an ADCP. ATLAS collects and stores meteorological and ocean temperature information once every ten minutes. The ADCP is programmed to take a measurement once every 15 minutes and has a bias typically on the order of 0.5 to 1.0 cm/s. (A detailed discussion of ADCP instruments and their sources of error is provided by Emery and Thompson, 1998).

D. INTERPOLATION ISSUES

Maps of SST, SSH, wind stress, currents, vorticity, and eddy kinetic energy (EKE), correlations and empirical orthogonal functions (EOF) are used to locate areas of significant statistical differences between ocean/atmospheric model runs. NOGAPS and COAMPS wind stress fields are interpolated to the PWC domain using their original horizontal grid spacing or the PWC grid spacing. Cubic spline interpolation of model wind stress to the PWC grid (~10 km) simulates the ocean model interpolation (Akima spline) and provides for an "ocean model view" of the atmospheric forcing. For a fair comparison of results, maps are displayed using the COAMPS 10 km grid geographic dimensions (30° N to 49° N from the coast to 130° W).

The reader is cautioned that contour plots interpolated to the PWC grid may distort the interpretation of the results due to the erroneous extension of land values to grid points over the ocean. The PWC grid is used for the mean plots in order to approximate what the ocean model will "see" when the wind stress is interpolated to the ocean model application grid. Recent studies show that extra care must be used when mapping wind stress and heat fluxes to the ocean model grid so that large land-ocean gradients do not contaminate the values over the ocean. Data processing for the PWC grid requires interpolation and the blending of those data to complete the model domain. Traditional (unconstrained) interpolation from the atmospheric model's native grid can yield unexpected results when interpolation overextends land values into the ocean (DeRada et al., 2002).

In NOGAPS MVOI, the optimal estimator is linear and consists of a weighted sum of all the observations within a specified range of each grid point. The objective mapping procedure produces a smoothed version of the original data field that will tend to underestimate the true version. Near boundaries, MVOI includes observations from outside the analysis domain. In data void areas, MVOI increases its smoothing length scale to retain scales larger than the data-void region. For COAMPS model runs, the multiquadric analysis has a small tendency to continue the gradient defined by the nearest observation when data are a large distance from the boundary. Thus the extrapolation effect is less severe in the multiquadric assimilation than for MVOI and smoothly analyzes the scales represented by observations in a particular region of the domain while not producing undesired results in another region (Nuss and Titley, 1994).

DeRada et al. (2002) used COAMPS 81, 27 and 9 km wind stress taken in July in the Central California region to demonstrate the effects of inter-grid interpolation on an atmospheric model. The wind stress maps showed extensive areas of possible land contamination. DeRada et al. (2002) used a weighted-average bilinear interpolator with ocean-to-land relaxation developed by NRL Monterey to bring out the desired features. The method fits a bilinear surface through existing data points where the value of an interpolated point is a combination of the values of the four closest points. Further research is needed to characterize the impact of seasonal land-sea differences on interpolation. In this study, winter land-sea thermal constrasts are significantly reduced compared to spring and summer and consequently less likely to cause problems.

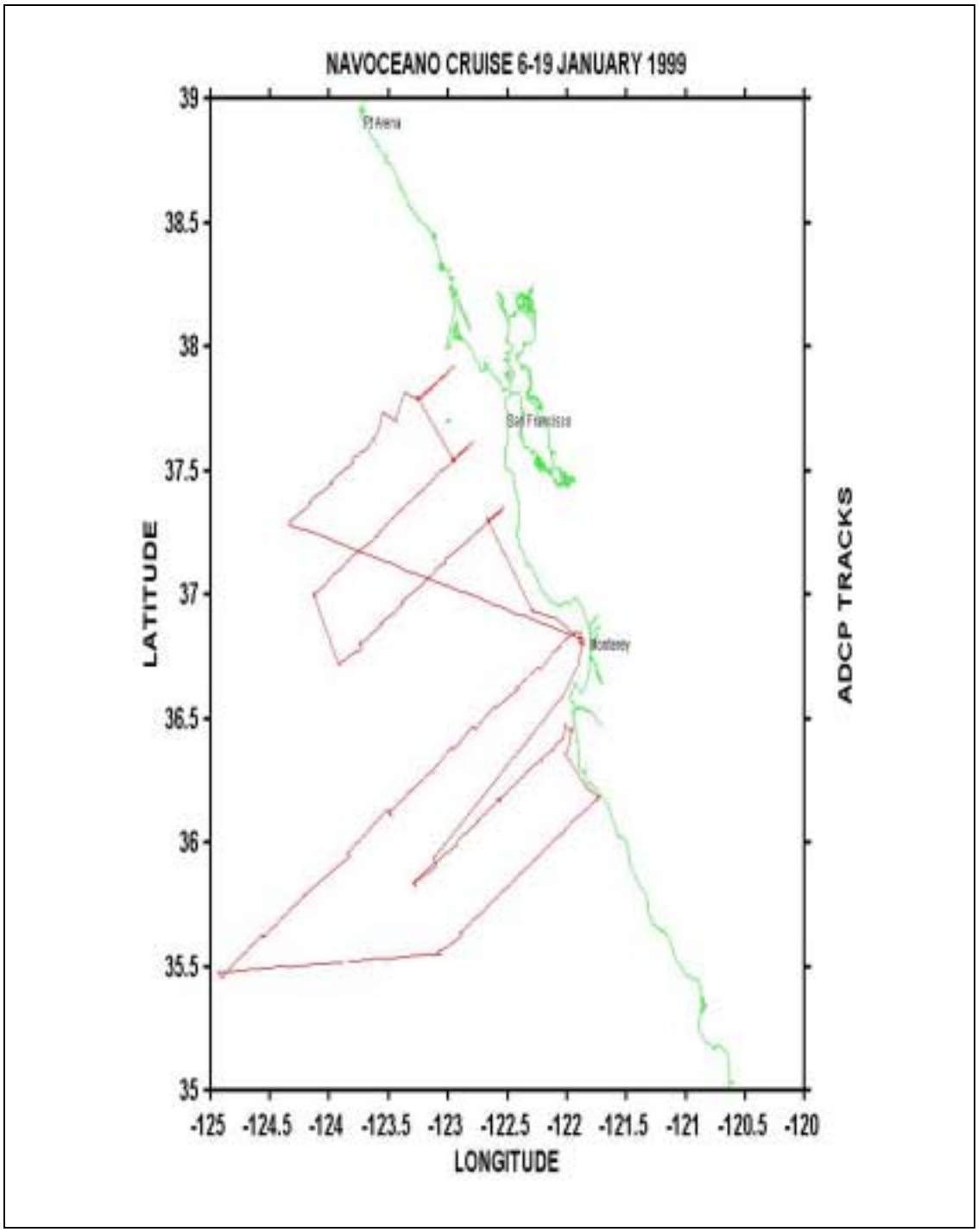

Figure 3.1. Actual CenCal CalCOFI tracks for the period of 06-20 Jan 1999.

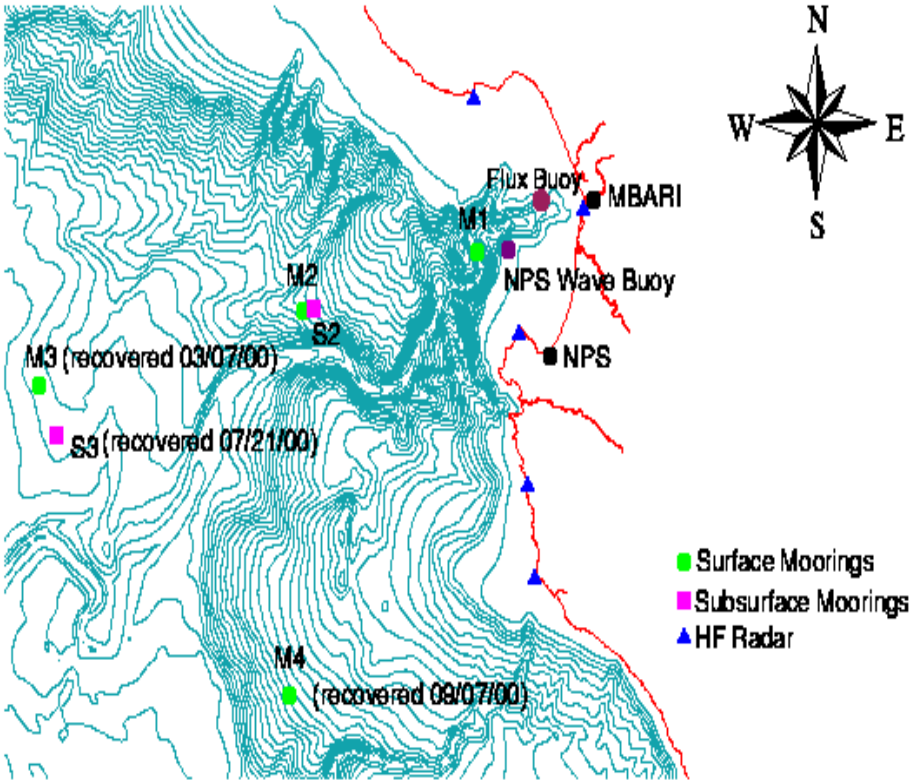

Figure 3.2. Monterey Bay CODAR Sites and MBARI moorings.

Figure 3.3. Pacific West Coast NDBC Moored Buoys.

THIS PAGE INTENTIONALLY LEFT BLANK

IV. PHYSICAL ENVIRONMENT

The PWC domain covers part of an eastern boundary current system known as the California Current System (CCS). The scales and dynamics of the ocean circulation along the Pacific West Coast are set by several characteristics of the physical environment: (1) strong wind stress forcing, (2) large alongshore scales for both the wind field and the bottom topography, (3) a relatively narrow and deep continental shelf, (4) a relative absence of major rivers and (5) a relative simplicity of coastline structure. The coastline between the Strait of Juan de Fuca (48°N) and the tip of Baja California is relatively straight but interrupted at several locations by substantal promontories. The largest bend in the coastline is between Point Conception (35° N) and San Diego (33°N), also known as the Southern California Bight, that is characterized by narrow shelves (width << 10 km) and an offshore region punctuated by a number of deep (depth > 500 m) basins (Allen, 1980; Hickey, 1998).

A. COASTAL METEOROLOGY

There is a strong relationship between the spatial and temporal patterns of wind stress curl and the seasonal variability of large-scale currents in the CCS. Batteen (1997) showed that wind forcing may be the most important generative mechanism for the currents and the intense and complex meander, eddy, jet, and filament structures in the CCS. Along-shelf wind stress is important for the formation of coastal jets while alongshore structure in the wind stress is important for undercurrent formation. For the Pacific West Coast, the spatial scales of the wind field are greater than 1000 km and 500 km in the alongshore and cross-shore directions, respectively, with significant spatial structure in both directions (Hickey, 1998).

The near-surface wind flow in the coastal environment is influenced by both large-scale and mesoscale wind phenomena. During winter, the North Pacific High and transient high-latitude low pressure systems dominate the climate of the western coast of

the United States. When the North Pacific High is dominate, the associated large-scale pressure pattern produces a northerly gradient wind flowing parallel to the coast towards the equator. During storm passages, the North Pacific High weakens and the equatorward directed winds change to poleward direction, particularly north of San Francisco. Local wind forcing usually dominates, especially in regions where winter storms are accompanied by strong poleward directed winds that increase in the direction of propagating waves. Off northern California, where the wind stress is generally strongest (e.g., see Bakun and Nelson, 1991), both local and remote forcing are important over periods of several days. The poleward wind stress increases to the north throughout the region while the equatorward wind stress reaches a minimum (Hickey, 1998).

Coastal upwelling is characterized by cyclonic wind stress curl near the continent, and anticyclonic further offshore, while the wind stress is predominantly oriented toward the equator. The maximum stress occurs some distance offshore, the decay toward the coast gives rise to the cyclonic curl, and the offshore decay leads to the anticyclonic curl. At most locations, minimum equatorward wind stress or maximum poleward wind stress occurs with downwelling at more northern latitudes in fall and winter (Huyer, 1983; Large et al., 1991).

B. COASTAL OCEANOGRAPHY

The large-scale (>500 km alongshore scale) currents include the equatorward California Current (CC), the wintertime-poleward Davidson Current (DC); the poleward California Undercurrent (CUC) which flows over the continental slope beneath the equatorward upper layers; and the Southern California Counter Current (SCC) or Eddy (SCE) if the current rounds Point Conception. (A detailed description of the CCS is provided by Strub et al., 1987; Lynn and Simpson, 1987; Huyer et al., 1983, 1991; Batteen, 1997; Hickey, 1998 and Collins et al., 2000).

The CC is equatorward year-round offshore from the shelf break to a distance ~1000 km from the coast. Strongest at the sea surface, the CC extends over the upper 500 m of the water column with seasonal mean speeds of 10 cm/s. South of Point

Conception a portion of the CC turns southeastward and then shoreward and poleward. This feature is known as the Southern California Counter Current (SCC) during the periods when the flow successfully rounds Point Conception or the Southern California Eddy (SCE) when the flow recirculates within the Bight (Hickey, 1998).

The CUC is a relatively narrow feature (~10-40 km) that is poleward over the continental slope from Baja California to Vancouver Island. It has a seasonal maximum in winter, coincident with the seasonal development of the Davidson Current in regions north of Point Conception. The CUC can be continuous over distances of at least 400 km along the slope with a jetlike structure and jet core located just seaward of and below the shelf break. Peak speeds observed are ~30-50 cm/s and strongest at depths of ~100-300 m from the surface (Hickey, 1998; Collins et al., 2000). The Davidson Current is strongest in winter, as is the SCC, and is poleward from Point Conception (35°N) to at least Vancouver Island (50°N). Over the shelf, there is also a strong tendency for poleward flow throughout the water column. This poleward flow is broader (~100 km in width) and sometimes stronger than the corresponding subsurface poleward flow in other seasons, and extends seaward of the slope (Hickey, 1998; Collins et al., 2000).

The primary forcing mechanism for the current field over the shelf is the alongshore component of wind stress. The variability of atmospheric storms and synoptic scale wind events induce current fluctuations with typical scales of 3-10 days. Regions seaward of the shelf are dominated by jets (core speeds exceeding 50 cm/s at the surface, widths of 50-75 km), eddies, and in some locations, propagating disturbances with typical scales of 10-40 days. Wind-driven signals in the Southern California Bight and northern Baja have much smaller along-shelf scales (20 km versus 500 km), weaker amplitudes and weaker seasonal variations than in the region north of the Bight (Hickey, 1998). In the CCS, few filaments and eddies are produced by poleward-directed currents. Coastline irregularities are generally required to trigger instabilities to allow coastal jets to separate from the shelf (Batteen, 1997). Satellite data (Hickey, 1998) suggest that coastal filaments are usually associated with a coastal promontory with the strongest coastal filaments appearing to separate from the shelf near coastal promontories and generally moving equatorwards.

The CCS includes one major river plume (the Columbia), several smaller estuaries and (primarily in the north) numerous submarine canyons. Within ~300 km of the coast, some of the fresher water in the upper 20 m of the water column is associated with the Columbia River plume (Batteen et al., 1995). The plume responds almost instantaneously to changes in wind speed or direction and appears to be governed by Ekman layer dynamics (~20-50 cm/s, depth of 5 m) rather than by changes in ambient geostrophic along-shelf flow. In winter, the plume has a dramatic effect on the Washington coast, producing time-variable currents as large as the wind–driven currents. The effects are confined primarily to the inner shelf for poleward wind conditions or to the upper 10 m or so of the water column for equatorward wind conditions. The plume is mostly unidirectional within the low-salinity bulge that emanates from the river mouth. Farther downstream, the currents tend to parallel salinity contours, suggesting a geostrophic momentum balance (Hickey, 1998).

Barotropic tidal currents on the shelf are typically ~5 cm/s, mixed with predominately semidiurnal constituents, and are mostly oriented along the local bathymetry. Tidal currents seaward of the continental slope are semidiurnal and strongly barotropic with amplitudes less than 4 cm/s. Barotropic tides that interact with bottom topography can generate internal (baroclinic) tides. Baroclinic tidal currents are primarily semidiurnal and substantially greater than those of the barotropic tide (5-10 cm/s). In the vicinity of submarine canyon floors, the internal tide can generate current velocities of ~15-20 cm/s (Petruncio, 1993). On the shelf, the internal tidal currents can dominate the variance of the weaker cross-shelf currents but usually do not dominate the alongshelf current variance (Hickey, 1998; Steger et al, 1998).

V. ATMOSPHERIC MODEL RESULTS

A. STATISTICAL TESTS

The statistical data set consists of ten NOGAPS (NGP)/COAMPS (CMP) model run combinations, each containing 109 three-hourly wind stress observations, and 28 observations of current speed, SST, SSH, and salinity. At the 95% and 99% significance level, only the wind stress and surface current speed show significant statistical differences between experiment runs (not shown). The F-distribution (ANOVA) has similar results with large F-ratio values >100 (no statistical difference) for salinity, SSH and SST and F-ratio values ~ zero (significant statistical difference) for wind stress and current speed. In the ocean and atmospheric results, the NOGAPS versus COAMPS runs have the most number of days of significant statistical difference. For the COAMPS versus COAMPS runs, the 45 km horizontal grid runs with synthetic scatterometer (COAMPS 45 km/Q) and without synthetic data (COAMPS 45 km) have the least number of days of significant difference followed by COAMPS 45 km/COAMPS 25 km, COAMPS 45 kmQ/COAMPS 25 km, and COAMPS 45 km/COAMPS 10 km.

These results indicate that with increasing atmospheric model horizontal resolution, wind stress and surface current speed will undergo a significant statistical change. However, the impact of inserting higher resolution scatterometer data on a coarser atmospheric model horizontal grid is relatively small statistically compared to increasing the horizontal grid resolution. In comparing QuikSCAT swaths to the three-hourly wind stress observations, the statistical results of the comparison between COAMPS 45 km and COAMPS 45 km/Q are independent of QuikSCAT swath coverage. For example, there is no siginifcant statistical difference between COAMPS 45 km and COAMPS 45 km/Q on 07 January 1999, However, simulated QuikSCAT swaths show good coverage of the model domain for that day. Similarly, there are small statistical differences between COAMPS 45 km/Q and COAMPS 25 km because the synthetic

observations are derived from the COAMPS 25 km data. In the following sections, this study will examine the underlying causes of the statistical differences.

B. WIND STRESS

The atmospheric model wind stress is in good agreement with previous studies that used aircraft measurements to characterize the spatial variation of the low-level wind and wind stress over the northern California shelf in winter (Enriquez and Friehe, 1995). The wind stress features characterize the variability of winter storms and the Pacific High. Meteorological activity is divided into seven days with essentially no storm activity followed by storm passages every two days through the northern domain (Figure 5.1). The first and second modes of EOF account for ~58 % of the explained variance of the wind stress (Figures 5.2, 5.3). Together with the mean wind stress, the first mode of EOF respresents a pattern of poleward winds north of Point Arena, and northwesterly and westerly winds south of Point Arena (Figure 5.4). In Figure 5.2, the positive EOF coefficients match the pattern of low pressure centers moving onshore along the Oregon and Washignton coasts. The negative EOF coefficients represent the the equatorward directed wind pattern that dominates the coastal environment south of San Francisco. The range of mean equatorward and poleward wind stress for all atmospheric model experiments (not shown) varies from ~ 0.05 to 0.15 Pa and 0.15 to 0.5 Pa, respectively. The highest wind stress values are located north of Cape Blanco to Canada (~ 0.2-0.5 Pa). Horizontal gradients of wind stress are predominantly cross-shore for equatorward wind stress and along-shore for poleward wind stress (Figure 5.4).

The significant statistical differences are most likely the result of mean wind stress differences caused by smoothing of the observations as the horizontal grid spacing increases from COAMPS (10 km) to NOGAPS (~139 km). The mean wind stress increases with increasing horizontal resolution with a range of 0.05 Pa to 0.15 Pa. Using a drag coefficient of 1.4×10^{-3}, the differences in wind stress equates to ~ 4-6 m/s in wind speed which is outside the standard error of 2 m/s and 1.4 m/s for model and scatterometer winds, respectively. The insertion of synthetic scatterometer observations

with relatively higher values (i.e., COAMPS 25 km wind stress) would nudge the COAMPS 45 km/Q run to a statistically different, but not significant operational impact. The mean wind stress values were taken offshore and outside of what NOGAPS considers as land (~139 km).

1. Wind Structure Resolution

On daily maps (not shown) with or without land masking, NOGAPS provides less structure detail than COAMPS, especially in the coastal areas associated with capes and promontories (e.g., Cape Blanco, Cape Mendocino, Point Arena and Point Conception). In NOGAPS results, areas of relatively high wind stress cover large areas (e.g., Cape Mendocino to Los Angeles) with no connection to coastal topography. The COAMPS results have a similar trend . However, the wind stress structure is better defined with increasing horizontal resolution. The COAMPS 10 km clealy shows a connection between coastal topography and areas of high wind stress that resemble expansion fans. Abrupt spatial and temporal variations in marine layer depth and velocity around California coastal bends are associated with supercritical flow. Along the western United States, areas of high wind stress (i.e., expansion fans) are created as a result of supercritical flow interaction in the marine boundary layer (MABL) between closely spaced coastal capes (Winant et al., 1988; Haack et al. 2001).

The principal requirements for supercritical flow are that the MABL be capped by a strong inversion, that it can be maintained as a material interface, that the Froude number be greater than one, and that there exists coastal topography comparable to the height of the MABL (Winant et al., 1988). The supercritical flow response is determined by the Froude number, speed of the incoming flow, and the bend angle of the cape or promontory. Supercritical flow occurs when the Froude number (ratio of fluid speed to the phase speed of internal gravity waves) is greater than unity. The Froude number is defined as follows:

$$Fr = V/(g`h)^{1/2} \qquad (5.1)$$

where g` = $g\Delta\theta/\theta$ is reduced gravity, $\Delta\theta$ is the potential temperature jump across the inversion, and h, V and θ are the fluid depth, speed, and potential temperature, respectively. The spring and summer seasons provide ideal conditions for supercritical flow with northerly winds characterized by a strong low-level inversion and a correlation of the wind spatial structure with the coastal topography. A typical Rossby radius of deformation is ~ 295 km with a horizontal length scale ~150-300 km. The MABL decreases from 1250 m offshore to 400 m nearshore with wind speeds greater than 8 m/s (~ 0.1 Pa using a drag coefficient of 1.4×10^{-3}).

In winter, the strong marine inversions and land-sea temperature differences of spring and summer are significantly reduced (Skogsberg, 1936; Bakun and Nelson, 1991; Round, 1993; Foster, 1993). However, early January 1999 (7-13 January) had unusual summerlike conditions. In Figure 5.5, COAMPS 45 km (07 January 1999) shows significant offshore areas of high wind stress with core values of 0.2. The maps are displayed on the PWC grid ($1/12^0$) and use land masking prior to interpolation and contouring. A similar image for COAMPS 10 km has core wind stress values of 0.35 Pa (Figure 5.6). Generally, the 45 km and 25 km grids show high stress flow parallel to the coastal topography and no connection to any cape or promontory. There is also no discernable difference between the 45 km grid and the 45 km grid with QuikSCAT.

COAMPS 10 km shows well-defined areas of high wind stress associated with capes. Haack et al.(2001) found similar results in the summer season using COAMPS nests of 45, 15, and 5 km. In Figure 5.6, the actual bending of the wind flow at Cape Mendocino is clearly visibile along with the typical meridional and zonal scales for an expansion fan. The COAMPS 25 km grid has similar features to the 45 km grid but with more structural detail. Due to its large grid spacing, NOGAPS does not show any near-coastal areas of high wind stress (not shown). However, COAMPS 10 km also shows areas of high wind stress activity in upcoast wind situations when transient storms cause a "split" into poleward and equatorward coastal wind stress. For example, wind stress on 19 January (not shown) has a division in poleward and equatorward winds in the vicinity of Point Arena. The COAMPS 10 km experiments clearly shows well-defined areas of high wind stress associated with Capes Blanco and Mendocino. Only the COAMPS 10

km horizontal grid provides a definitive picture of both the location of the split in coastal wind regimes and the associated areas of high wind stress. Thus, increasing the horizontal grid spacing provides better-defined structure (Mass et al., 2002). In regard to forecast accuracy, no field observations are used for model validation outside of the buoys, which are discussed in Chapter VI.

2. Wind Stress Curl

Using equation (3.11), maps of the wind stress curl are created on a PWC grid ($1/12^0$). No land masking was used prior to contouring in order to examine potential errors due to interpolation. The NOGAPS mean curl of wind stress (not shown) is an order of magnitude smaller (10^{-4} vs. 10^{-3}) than the values seen in the COAMPS runs. Generally, the NOGAPS wind stress curl values are closer to monthly averages (Nelson (1977) taken from monthly averaged stresses (0.03 – 0.05 Pa (100 km)$^{-1}$), compared to values (0.2-1.5 Pa (100 km)$^{-1}$) obtained from aircraft measurements (Enriquez and Friehe, 1995). This is a further indication that the higher resolution COAMPS is producing higher values of wind stress compared to NOGAPS. If the real environment has no significant features (i.e., offshore and mesoscale) that are resolvable by the lowest horizontal resolution model (NOGAPS), it is possible that the difference in horizontal grid spacing will create higher gradients in the higher resolution model (COAMPS). This would explain the higher COAMPS values of wind stress and wind stress curl.

The mean wind stress curl shows a seaward increase in the magnitude of the equatorward wind stress vector south of Point Arena that produces a predominantly positive curl (Enriquez and Friehe, 1995). North of Cape Blanco, the seaward increase in the poleward wind stress component produces a negative curl onshore and a positive curl far offshore in NOGAPS (not shown). Approaching the coast, daily and mean NOGAPS maps (not shown) show large (~ 100-200 km) areas of positive or negative wind stress. As the horizontal grid spacing descreases (i.e., COAMPS), the large areas of wind stress curl narrow in size and begin to show distinct features associated with coastal topography.

COAMPS 45 km (Figure 5.7) has areas of weakly positive wind stress curl along the Oregon/Washington coast and in the SCB associated with capes and promontories. The most significant feature is a very pronounced area of positive curl in the vicinity of Cape Blanco (~0.02 Pa/km). This feature appears unphysical and is not seen in the COAMPS 25 km and 10 km runs. There is no difference between the maps of COAMPS 45 km and COAMPS 45 km with QuikSCAT, and QuikSCAT synthetic wind stress has a 25 km resolution. In Figure 5.8, the COAMPS 10 km wind stress curl matches the locations and horizontal scales of the expansion fans previously seen in the wind stress (Figure 5.6). Since COAMPS 10 km has comparable horizontal resolution to the PWC model, the anomalous Cape Blanco feature seen in COAMPS 45 km is most likely a result of interpolation error (land contamination). Using COAMPS 81, 27, and 9 km nests, DeRada et al.(2002) found similar but more significant interpolation errors in a summer study of heat fluxes. Winter air-sea horizontal gradients are weaker compared to the summer, thus reducing the number of unphysical features created by interpolation errors.

C. COMPARISON TO OBSERVATIONS

The wind data from twenty-five buoys (See Appendix, Table A.1) is converted to wind stress using the method of Large and Pond (1981) for buoy and model comparison (Note that wind observations from the MBARI buoys are unavailable for the period of this research). NOGAPS and COAMPS horizontal grid data are interpolated from their native grids (no land masking) to the PWC ocean model grid using the nearest neighbor method, to find the shortest distance between the PWC gridpoint and buoy location. Generally, the model grid points fell within 6 km of the buoy locations. The "distance to buoy (km)" columns (Table A.1) contain the uninterpolated (non-PWC grid) NOGAPS and COAMPS gridpoint distances to the buoys. The majority of the NOGAPS and COAMPS uninterpolated gridpoints fall within half of the horizontal grid resolution for that particular model run.

NOGAPS and COAMPS underestimate and overestimate the wind stress, respectively. In Figure 5.9, wind stress increases with increasing horizontal resolution, and COAMPS 45 km/Q is indistinguishable from COAMPS 45 km. The lowest and highest buoy wind stress values occur in the periods 07-13 January 1999 and 14-21 January 1999, where the latter period coincides with frequent storm passages. Buoys located north of Point Arena typically show southerly wind stress throughout both periods. South of Point Arena the buoy wind stress shifts from northerly in the first seven days to southerly in the latter period. In almost all cases, NOGAPS has the lowest wind stress values of the atmospheric model runs while COAMPS 10 km usually has the highest wind stress.

The buoys located in open ocean (46005,46006,46059) are in good agreement with the models (Figure 5.10). However, NOGAPS and COAMPS have difficulty with the land stations along the Oregon/Washington coast (TTIW1, DESW1, NWPO3, CARO3), especially during the relatively lower wind stress conditions prior to storm passage (Figure 5.11). However, the models are in good agreement with land stations located along the California coast (PTAC1 and PTGC1) throughout the study period (Figure 5.12). As before, NOGAPS and COAMPS underestimate and overestimate the wind stress, respectively. This finding is further supported by an error analysis of selected buoys. Note the high wind stress for COAMPS 25 km compared to COAMPS 10 km in Figure 5.12 (PTGC1). This may be the result of land contamination where a COAMPS 25 km land gridpoint containing a relatively higher wind stress value is interpolated to a PWC ocean gripoint.

The higher resolution runs have the lowest errors in locations near the coast. For buoys 46023 (Pt. Arguello) and C-MAN station PTGC1 (Pt. Arguello), the COAMPS runs have the lower RMSE compared to NOGAPS (Figure 5.13). Buoys 46023 and 46053 (Santa Barbara, East) are located 11 km (~ one PWC gridpoint) and ~ 8 km from land, respectively (See Appendix, Table A.1), yet NOGAPS follows COAMPS 25 km with the lowest RMSE followed by NOGAPS. Thus, the proximity of the model grid to the buoy cannot explain why the lower resolution model sometimes outperformed the

model with the smaller grid spacing. For example, the COAMPS 10 km gridpoint is located 51 km closer to buoy 46053 compared to NOGAPS.

NOGAPS mean error (ME) is consistent in showing the tendency to underestimate wind stress with 23 of 26 buoys showing negative NOGAPS ME values (Figure 5.14). In COAMPS, the ME is more variable with the majority of results showing positive ME values. The RMSE and ME for COAMPS 45 km and COAMPS 45 km/Q are similar while COAMPS 25 km often shows an opposite bias (ME) compared to both COAMPS 45 km and COAMPS 45 km/Q. This result is noteworthy because COAMPS 25 km is the source of synthetic satellite observations for COAMPS 45 km/Q, and the insertion of the synthetic data into the 45 km grid failed to significantly bias the results towards COAMPS 25 km.

Overall, no direct relationship can be determined between the model gridpoint distance from the buoy position and forecast error. The majority of cases show only small differences in the forecast skill between COAMPS 45 km and COAMPS 45 km with QuikSCAT. The RMSE of the U and V components of wind stress do not indicate any particular trend with regard to model/buoy co-location (not shown). For example, the U and V components of RMSE for COAMPS 25 km is greater for the C-MAN station PTGC1 compared to buoy 46053 although the COAMPS 25 km gridpoint is located nearer to PTGC1 (9 km versus 14 km). In addition, for one-third of the buoys, NOGAPS had the lowest RMSE.

E. DISCUSSION AND SUMMARY

With the exception of COAMPS 45 km with synthetic QuikSCAT, the same observation data is inserted into the NOGAPS and COAMPS models. All COAMPS numerical experiments use NOGAPS for outer boundary conditions, and all atmospheric data are plotted on both their native grids and interpolated to the PWC ocean model grid for comparison. In regard to the PWC interpolated atmospheric plots, the increase in the magnitude of wind stress, and in some cases, the persistence of wind stress with increasing model horizontal resolution may be the result of the better handling of smaller

scale phenomena by the smaller grids, the reduction in the smoothing with the reduction in grid spacing, and more over-water versus over-land points for the higher resolution experiments. However, the differences in the resolved coastline geometry between the variable horizontal grids may also play a significant role in the differences between numerical experiment results. In winter, the land-sea thermal contrasts are significantly reduced but the difference in land-sea roughness (i.e., drag coefficient) remains. Traditional interpolation schemes do not always yield expected results when interpolating along a coastline where over-land values can erroneously be extended to grid points over the ocean. Therefore, the extension of land values over the ocean may play a role in the higher wind stress results as horizontal grid spacing decreases.

There are significant statistical differences between atmospheric model predictions due to changes in the horizontal grid spacing. The differences can take the form of domain-wide increases in wind stress and structures associated with coastal topography. The most significant difference occurs between NOGAPS and the COAMPS runs with COAMPS having the higher wind stress. A smaller but similar trend of higher wind stress with increasing resolution is found between the COAMPS runs. With regard to wind structure, the COAMPS 25 km and COAMPS 10 km runs have significant skill (evaluated subjectively) in detecting small scales of variability associated with capes and promontories. Under the proper meteorological conditions, COAMPS 10 km shows the structure of expansion fans in the vicinity of Cape Blanco, Cape Mendocino, Point Arena and Point Conception.

Ascending and descending satellite tracks show consistent and good QuikSCAT coverage of the coastal areas over the 14-day period. However, the insertion of synthetic scatterometer data into a lower horizontal resolution model has the smallest statistical difference. The difference between COAMPS 45 km and COAMPS 45 km with synthetic QuikSCAT wind stress can be attributed to the insertion of higher wind stress values from the synthetic scatterometer using COAMPS 25 km wind stress as satellite observations. As in the COAMPS 45 km predictions, there is a significant difference between the COAMPS 45 km with QuikSCAT and the COAMPS 25 km experiment. This indicates that there is a limit to the effect of the insertion of high resolution,

"perfect'" observations into a coarser grid model. Increasing the number of scatterometer satellites, and better temporal/spatial coverage, may improve the forecasts of coarser grid models to some limiting point.

Atmospheric model comparisons to buoy wind stress show good agreement with a tendency for NOGAPS and COAMPS to underestimate and overestimate wind stress amplitude, respectively in addition to a small direction bias to the right of the real wind stress. In general, the higher resolution results have the lowest errors in locations near the coast. The insertion of synthetic QuikSCAT data into the COAMPS 45 km experiment produces no significant improvement in forecast accuracy or difference between COAMPS 45 km without QuikSCAT compared to buoy wind stress and current. This result is not unexpected in that surface observations influence only a very thin layer of the model atmosphere and usually have little value in initializing atmospheric models compared to atmospheric profiles. Multiple satellites with higher spatial and/or temporal resolution (i.e., multiple QuikSCAT satellites with ~ 10 km horizontal resolution) may be required in the future to resolve the spatial limitations of scatterometers within 25 km of the coastline. However, adding more platforms won't help the basic problem that surface observations are not allowed in two-dimensional multiquadric/MVOI to influence a layer of the atmosphere. Better improvement might be realized if a data assimilaion scheme were able to allow QuikSCAT observations to influence the lower atmosphere through some depth, in a physically consistent method so that the thermal fields correctly balance the mass fields.

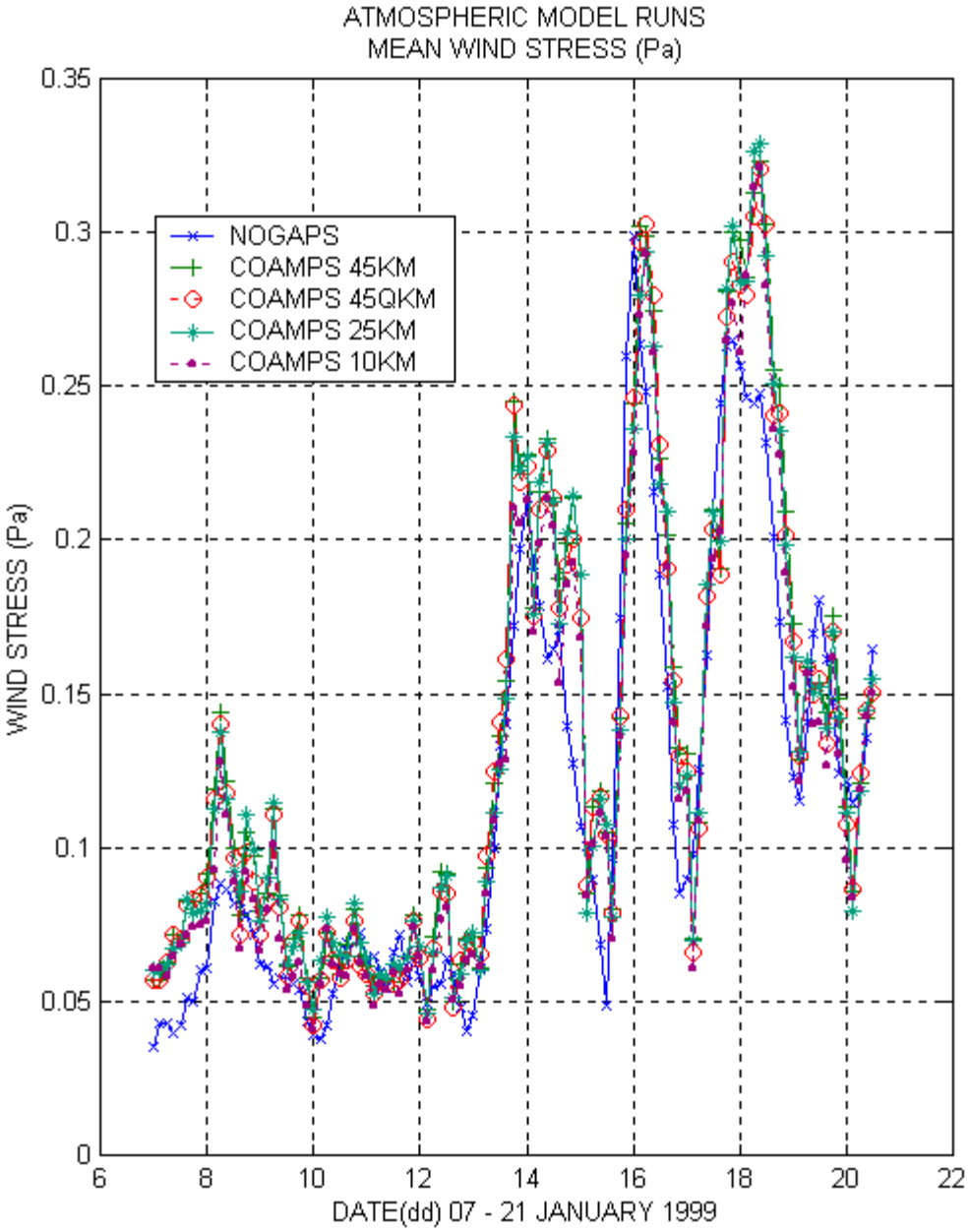

Figure 5.1. NOGAPS/COAMPS wind stress for 07-21 January 1999.

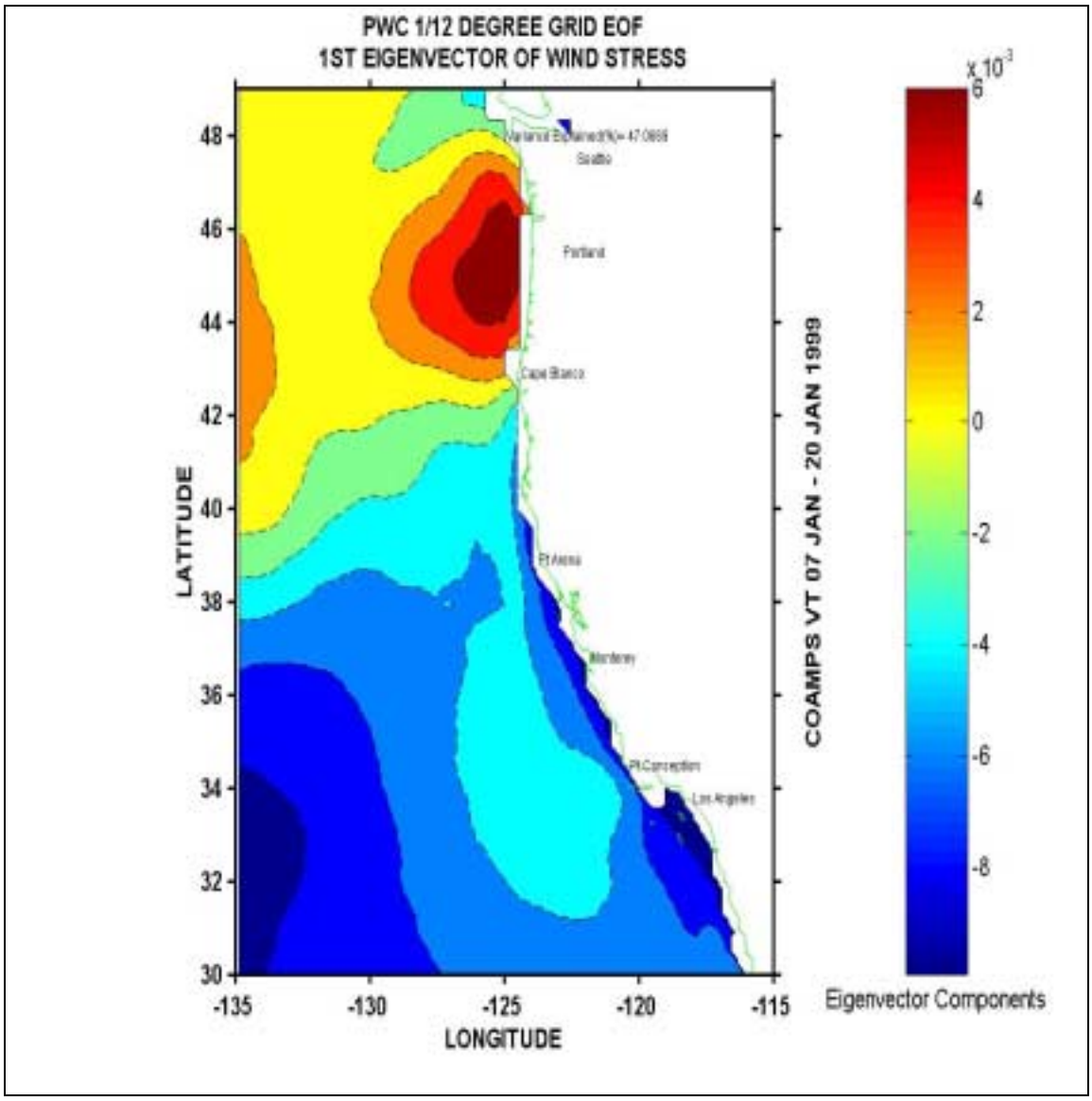

Figure 5.2. First EOF of wind stress for 07-21 January 1999.

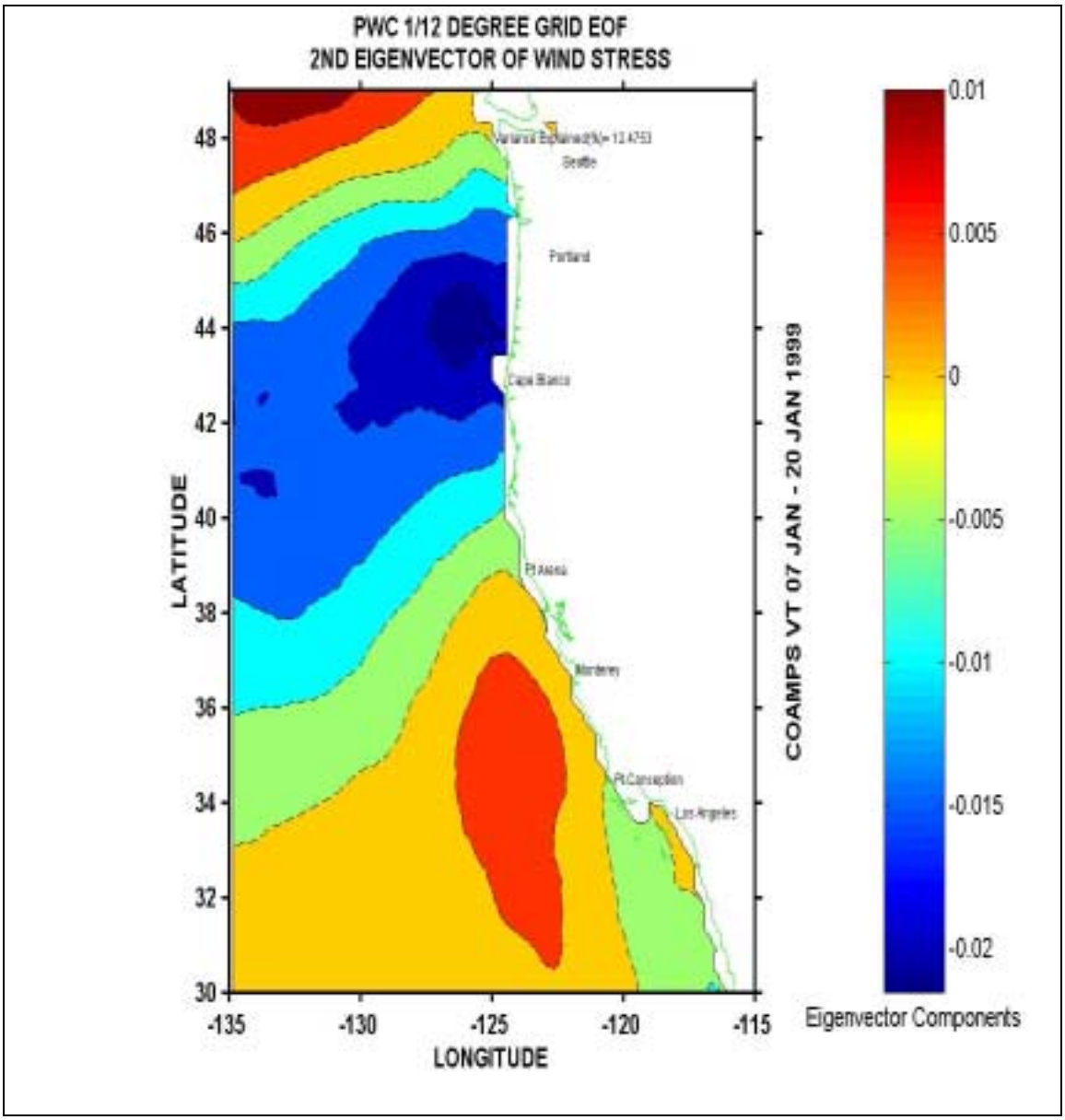

Figure 5.3. Second EOF of wind stress for 07-21 January 1999.

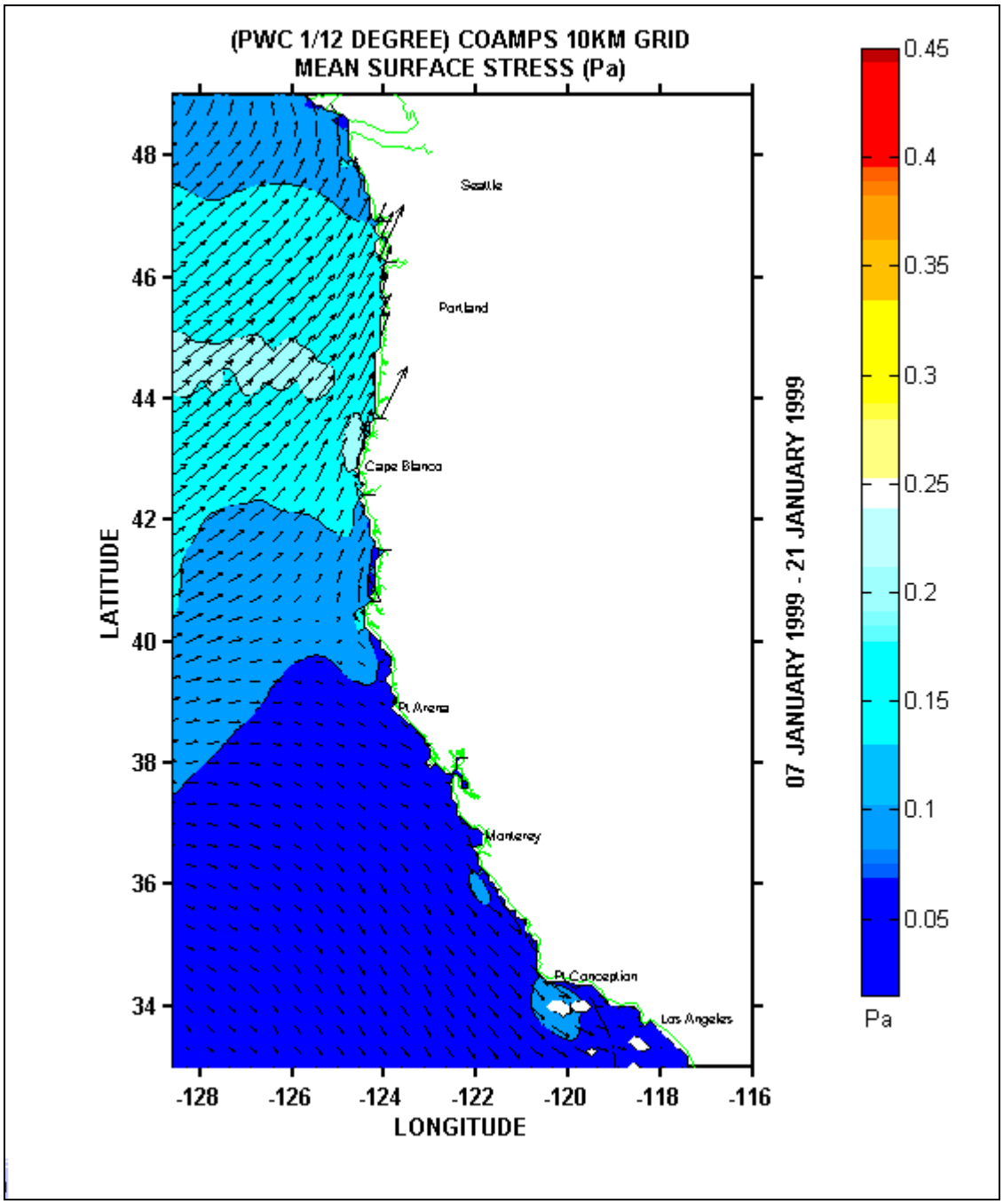

Figure 5.4. COAMPS 10 km mean wind stress for 07-21 January 1999.

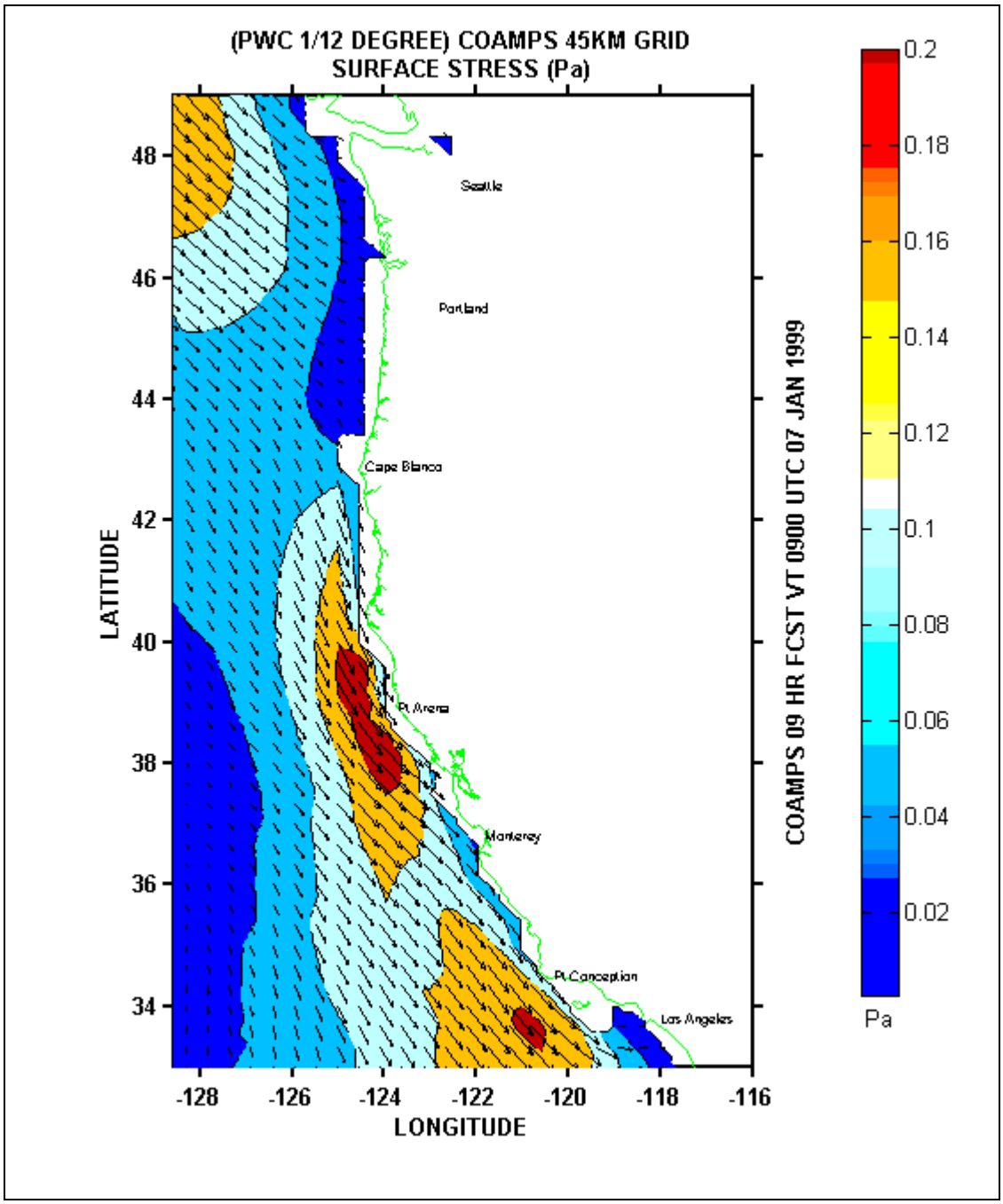

Figure 5.5. COAMPS 45 km wind stress (0900 UTC, 07 Jan 1999).

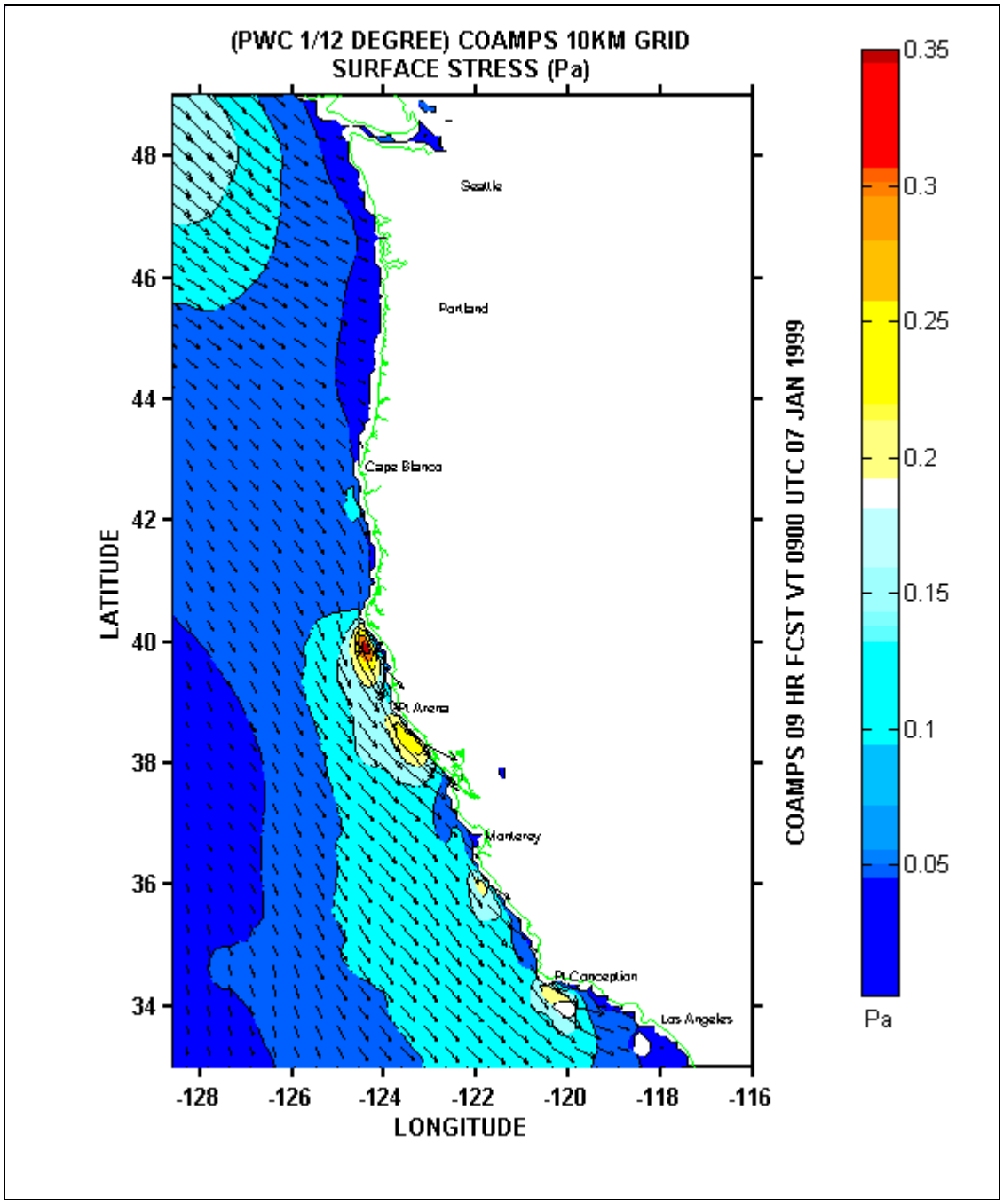

Figure 5.6. Same as Figure 5.8, expect for COAMPS 10 km.

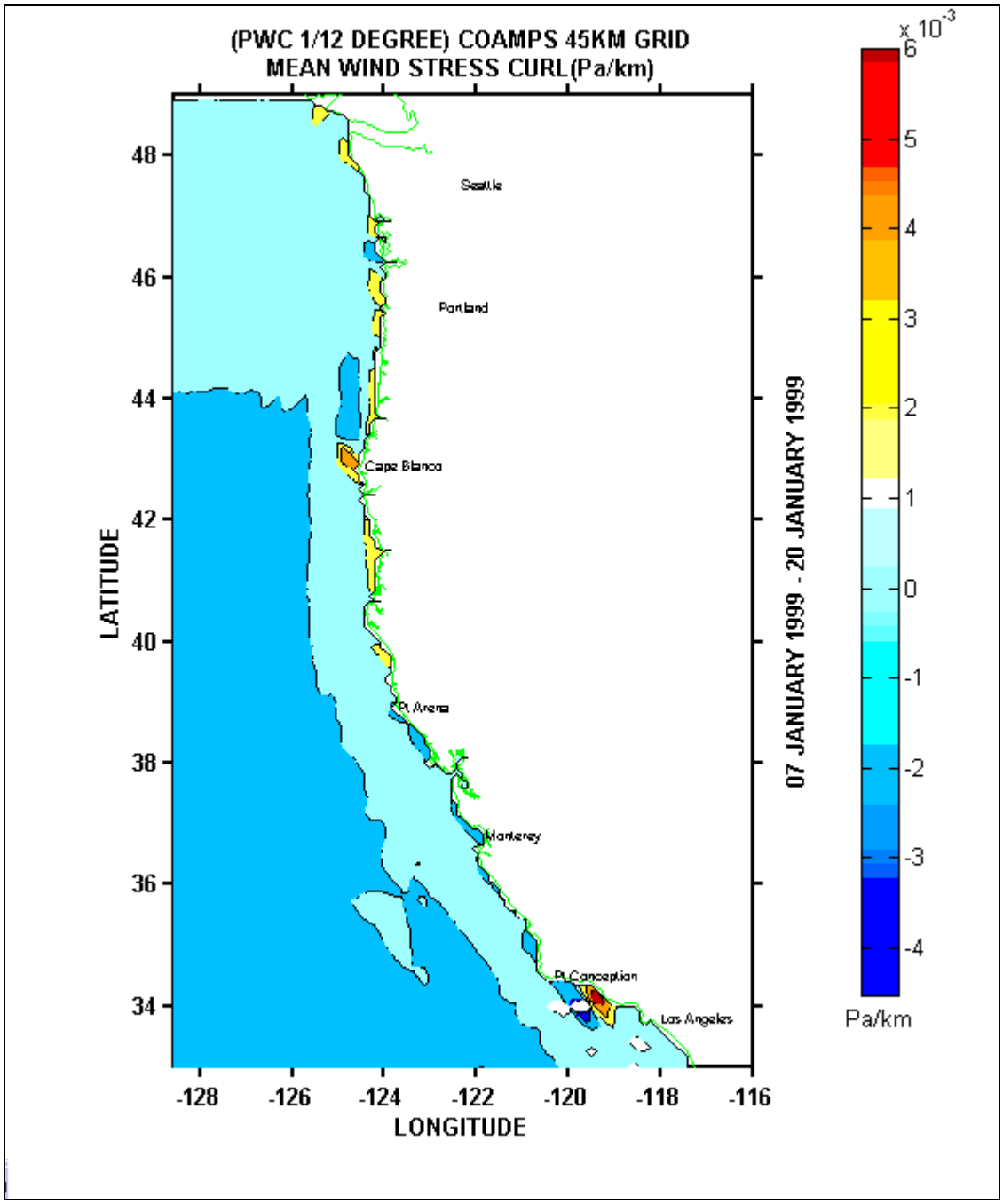

Figure 5.7. COAMPS 45 km mean wind stress curl (07-21 Jan 1999).

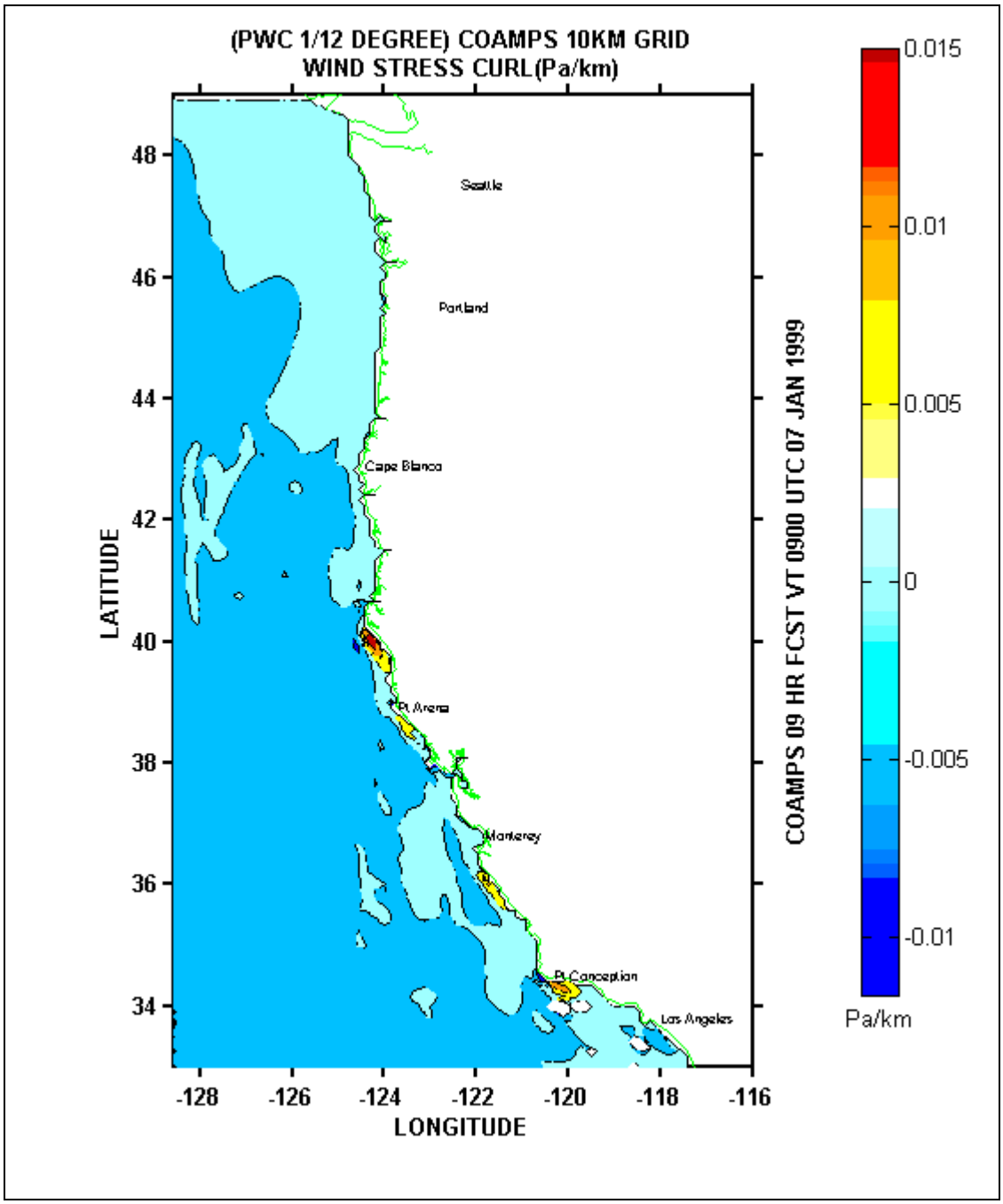

Figure 5.8. COAMPS 10 km wind stress curl (0900 UTC, 07 Jan 1999).

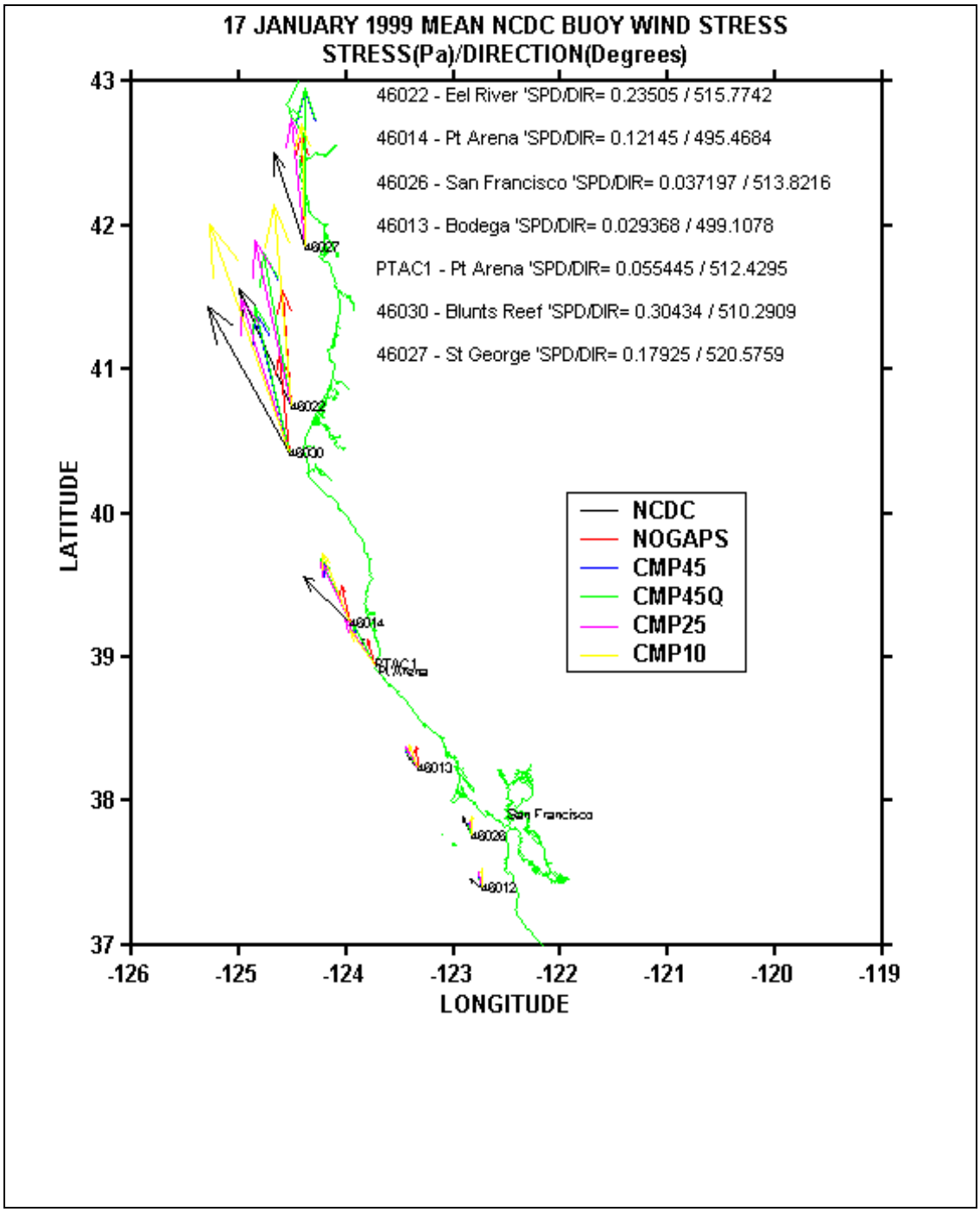

Figure 5.9. Buoy wind stress - San Francisco to St. George (17 Jan 1999).

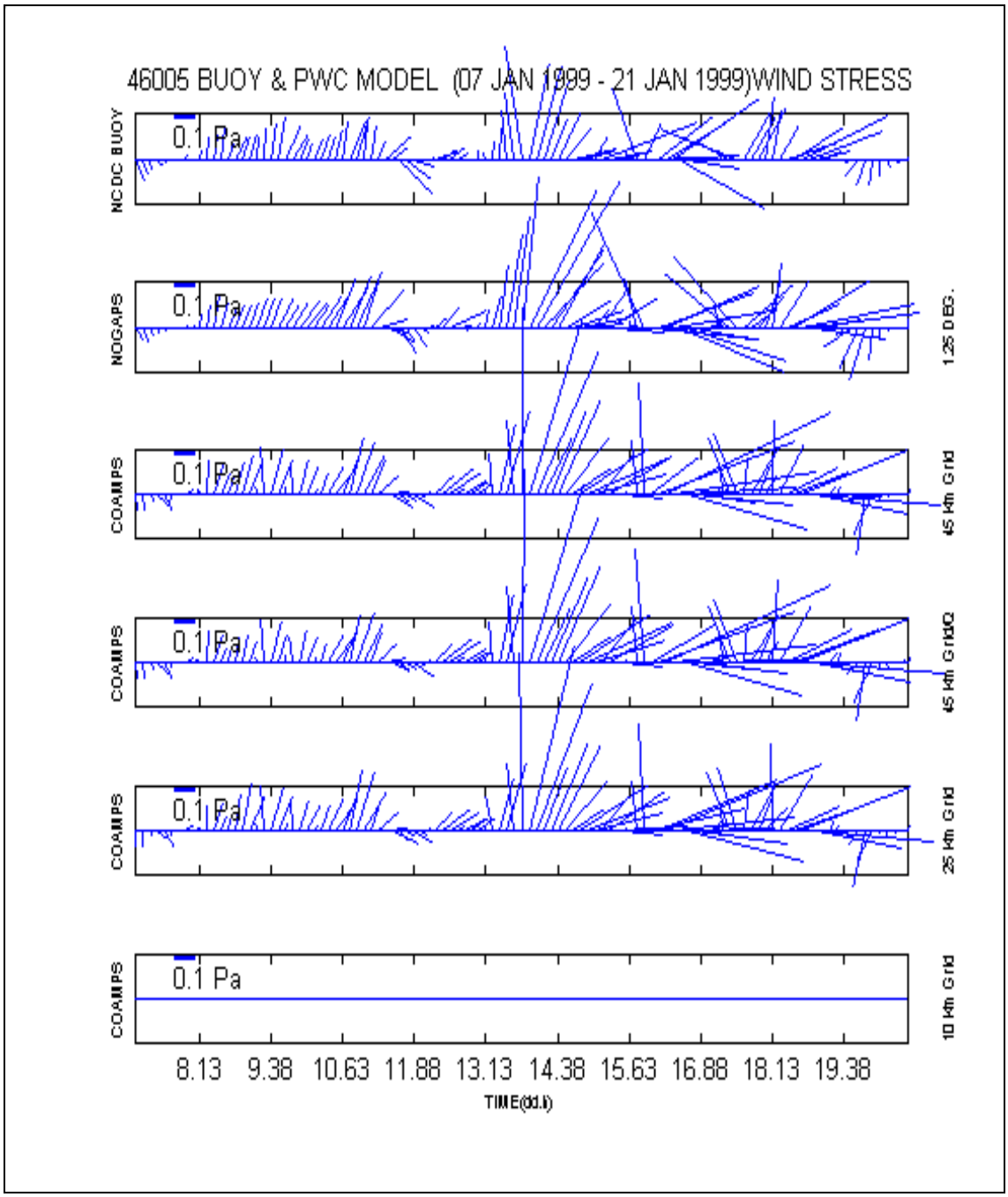

Figure 5.10. NDBC buoy 46005 (Washington) wind stress versus.

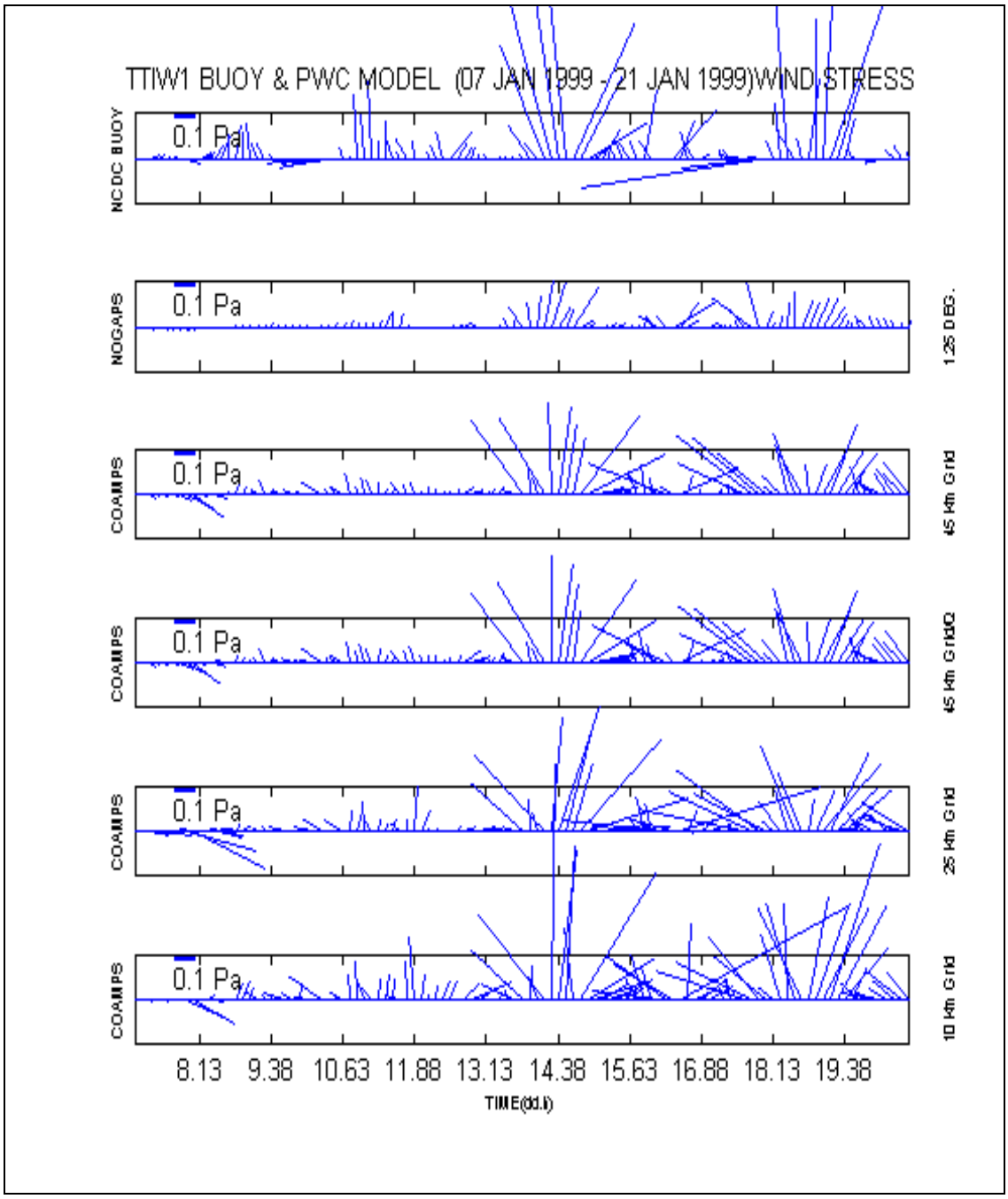

Figure 5.11. C-MAN station TTIW1 (Tatoosh, Island) wind stress.

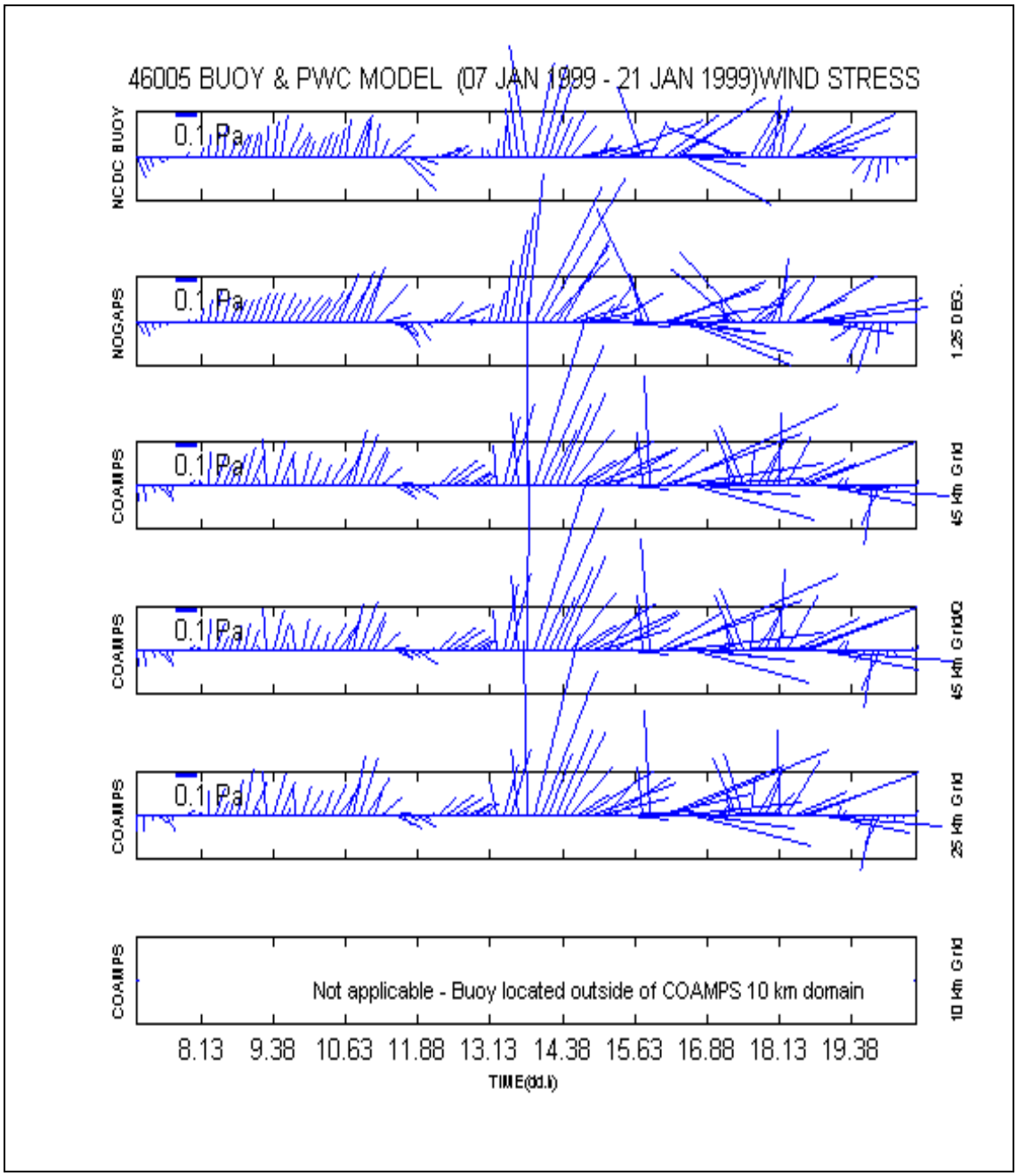

Figure 5.12. PTGC1 (Point Arguello, CA) wind stress.

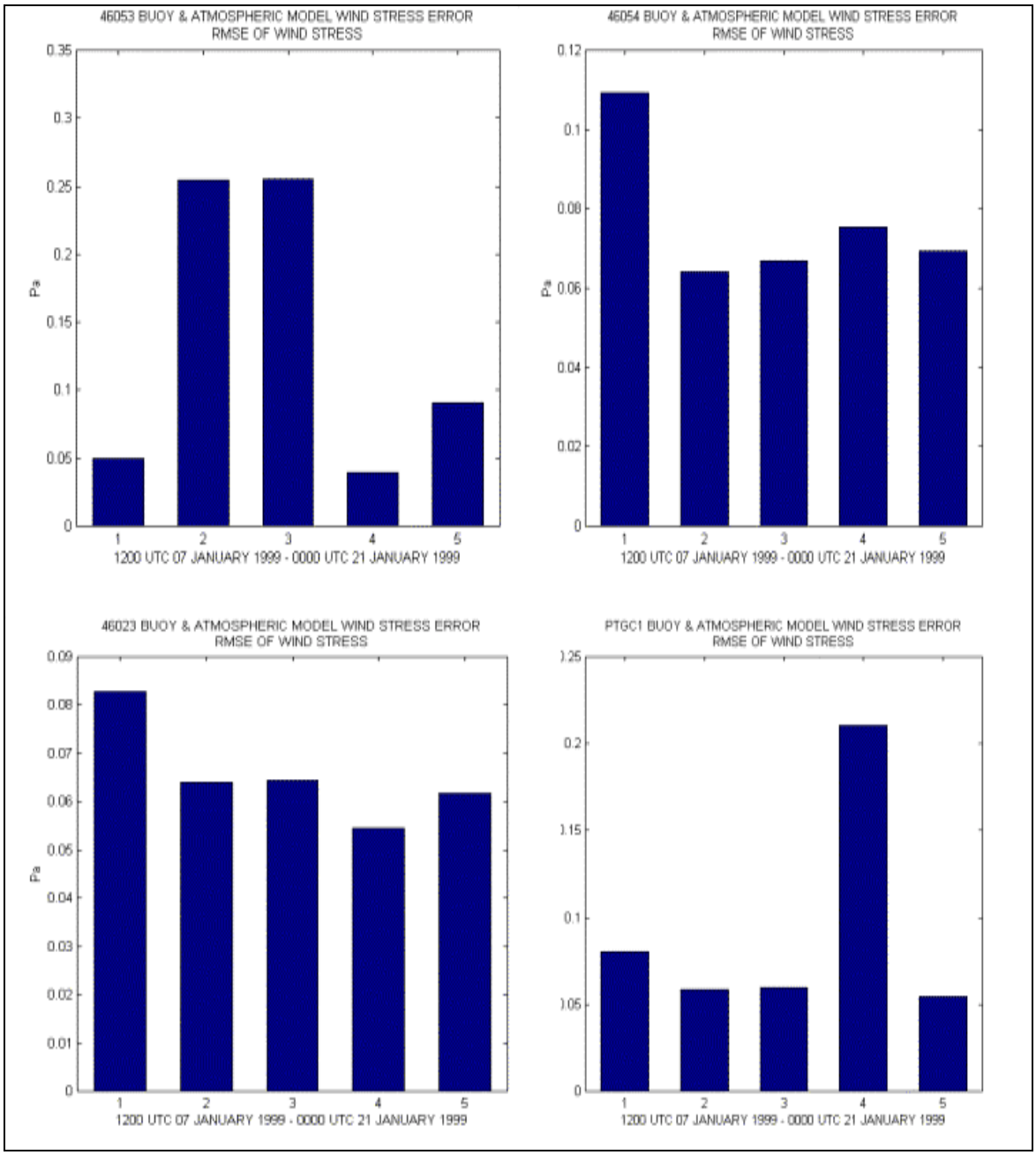

Numbers (1,2,4,4,5) indicate atmospheric model runs (NOGAPS, CMP 45 km, CMP 45 km/Q, CMP 25 km and CMP 10 km).

Figure 5.13. Buoy wind stress RMSE (46053, 46054, 46023, PTGC1).

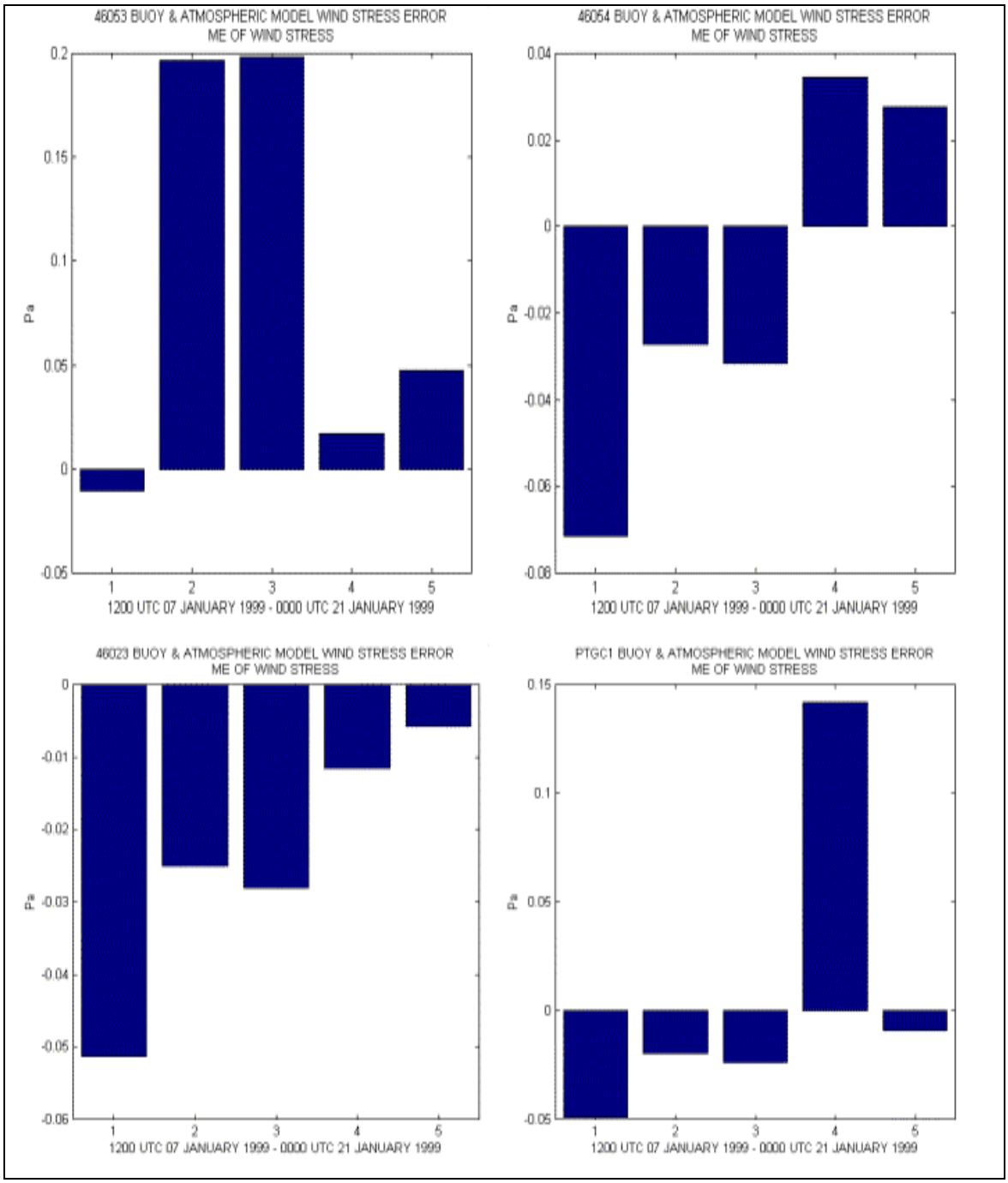

Figure 5.14. Same as Figure 5.12, except for mean error (ME).

VI. OCEAN MODEL RESULTS

A. OCEAN CURRENT

1. Surface Current Velocity

Maps of the mean current velocity overall are in good agreement with the expected variability and features of the CCS (Figure 6.1). All ocean models show extensive variability with meanders and numerous eddy features. A large meander (20-30 cm/s) flows westward just off Monterey Bay. In the Southern California Bight, the SCC can be seen rounding Point Conception, and in the northern region of the domain, the highest current speeds (~50 cm/s) run northward from Cape Blanco to Canada (Garfield et al., 2000). These features are consistent in all model runs. In Figure 6.2, peaks in mean current speed correspond to peak periods in mean wind stress (Figure 5.1) on 8, 14, 16 and 18 January 1999.

The first (Figure 6.3) and second (Figure 6.4) EOFs of current speed account for over 42% and 13% of the variance, respectively. Both eigenvectors show the area north of Cape Blanco having the highest variance in conjunction with the high wind stress and currents caused by storm passages. The most significant differences occur between the NOGAPS and COAMPS runs. Generally, the number of current vectors exceeding 50-60 cm/s increases between NOGAPS and COAMPS forcing runs along the Washington coast. Thus, like wind stress, the dominant trend is for the current speed to increase with increasing model resolution. The COAMPS models show an average 5 cm/s increase in surface current speed over NOGAPS in the offshore domain. Near the coast, the area with the highest difference (~10-20 cm/s) is located in a relatively narrow (~20 km) region along the coast from Canada to Cape Blanco. Similar differences are found between the NOGAPS/COAMPS 45 km and NOGAPS/ COAMPS 45 km/Q runs (not shown).

In comparisons of COAMPS versus COAMPS, there is no discernible difference between COAMPS 45 km and COAMPS 45 km/Q, while there is some similarity between the COAMPS 25 km and COAMPS 10 km runs. The COAMPS 45 km run has relatively higher current speeds (+1.5 cm/s) offshore of Washington and San Francisco, while the COAMPS 45Q run has relatively higher current speeds (+ 3 cm/s) north and south of Cape Blanco and in the Southern California Bight. Over most of the domain, COAMPS 45 km/Q, COAMPS 25 km and COAMPS 10 km all show relatively higher currents speeds of ~5-15 cm/s over COAMPS 45 km. In particular, COAMPS 45 km/Q and COAMPS 25 km have higher (15-30 cm/s) current speeds north of Cape Blanco and in the Southern California Bight. Finally, COAMPS 10 km shows a relative increase in current speed (10-15 cm/s) over COAMPS 45 km, COAMPS 45 km/Q and in an area that runs south of Cape Blanco to San Francisco (not shown).

A good example of the difference between NOGAPS and COAMPS wind forcing is provided in the Southern California Bight. Evaluating the PWC model depth-integrated alongshore momentum equation, Gan and Allen (2002) show the setup of an alongshore pressure gradient forces northward currents during relaxation of southward upwelling-favorable winds. In their studies, intensified nonlinear effects accompany the acceleration of the flow around the capes which influences the local alongshore pressure balance. During equatorward wind flow and southward wind-driven currents, lower pressure off a cape and higher pressure downstream of it generate a northward pressure gradient south of the cape. Strong onshore geostrophic currents related to the northward pressure gradient help produce colder upwelled water in the lee of the capes. As the equatorward winds decrease or increase, northward currents are formed near the coast. The individual terms of the model depth-integrated alongshore momentum equation are not evaluated in this study. However, the numerical experiments exhibit similar patterns seen in the studies by Gan and Allen (2002) and Winant et al..(2003). In the COAMPS 10 km run (Figure 6.5b), the currents never round Point Conception but form the Southern California Eddy (SCE) by developing a cyclonic circulation within the Bight. COAMPS 45 km/45 km w/QuikSCAT and COAMPS 25 km also show the SCE (not shown) as a result of higher wind stress compared to the NOGAPS. However, using NOGAPS

forcing (Figure 6.5a), the SCC can be seen rounding Point Conception. Normally, the formation of the SCC occurs in late fall or early winter (November-December). However, the unusual summer-like conditions results in the SCC forming in January 1999 (Winant et al., 2003). Similar results occur in the mean SST where the NOGAPS forced current (Figure 6.6) and high SST moves northward and around Point Conception to within 100 km of Monterey Bay. Using COAMPS 10 km forcing, the high SST remains in the SCB (Figure 6.7).

The COAMPS experiments provide a better definition of eddies compared to NOGAPS. For example, where there is a semi-enclosed circulation (anticyclonic or cyclonic), the COAMPS predictions have a tendency to transform the circulation into a complete eddy feature. Off Cape Mendocino, Pullen (2000) used a nested version of the PWC (9 km, 3 km, 1 km) using NOGAPS wind forcing during the 1996-1997 winter season. The PWC 3 km nest showed an anticyclonic eddy west of Cape Mendocino. The same feature appears in this study; however, the NOGAPS experiment shows the feature semi-enclosed while in the COAMPS experiment it becomes an anticyclonic eddy (Figure 6.8). Note that the COAMPS wind stress in this study used a 10 km resolution PWC ocean model and formed the same feature as a 3 km resolution model using NOGAPS wind forcing. Thus, the higher resolution of COAMPS wind stress in this study was able to form the same feature in a coarser ocean model (~10 km) over a two week period as a higher resolution ocean model (~ 3 km) using NOGAPS wind stress over a one year period (Pullen, 2000).

Finally, the depth-integrated velocity provides a clear depiction of the DC. In the NOGAPS run (Figure 6.9) the highest current speeds in the DC are associated with capes and promontories, and the Washington/Oregon coast. In the COAMPS 25 km run (Figure 6.10), these areas experience a significant increase (20-30 cm/s) in current speed. This result reflects the higher wind stress forcing of COAMPS 25 km compared to NOGAPS. A similar trend is present for the other COAMPS runs (not shown), and current speed increasing with increasing atmospheric model horizontal resolution.

2. Eddy Kinetic Energy (EKE) and Vorticity

The distribution of mean and eddy kinetic energy (EKE) is an important measure of model dynamics and can be related to several model-specific issues such as horizontal resolution, sub-gridscale dissipation, formulation of advection operators, etc (Haidvogel, 1999). There is a distinct difference in EKE between the NOGAPS and COAMPS model runs (Figure 6.11). The COAMPS runs show significantly higher EKE (400-450 $cm^2\ s^{-2}$) compared to NOGAPS (100 $cm^2\ s^{-2}$) in a well-defined area running along the coast south of Cape Blanco to Canada. As previously mentioned, EOF analysis and depth integrated current locate the highest wind stress and currents along the Oregon/Washington coast due to winter storm landfall. Thus, the lower NOGAPS forced EKE can be contributed to relatively lower wind stress that causes lower current speed and EKE in this area.

Like EKE, vorticity is also an important measure of model dynamics. Arthur (1965) used the vorticity equation in discussing the calculations of vertical motion in eastern boundary currents. The vorticity equation can be rewritten as:

$$f\frac{\partial w}{\partial z} = \frac{D\xi}{Dt} + \beta v - \frac{1}{\rho}\frac{\partial}{\partial z}\left(\frac{\partial \tau_y}{\partial x} - \frac{\partial \tau_x}{\partial y}\right) \qquad (5.2)$$

(1) (2) (3) (4)

Term 2, the total derivative of relative vorticity, is significant when the flow has appreciable curvature as near capes and points. Natural coordinates are used to define relative vorticity:

$$\xi = \frac{V}{R_s} - \frac{\partial V}{\partial n} \qquad (5.3)$$

(1) (2)

where R_s is the radius of curvature, V is the north-south velocity component and n is the unit vector normal to the direction of flow. Using the relative vorticity (Equation 5.3) and terms 2 and 3 of Equation 5.2, it can be shown that terms 2 and 3 tend to cancel

poleward of capes but equatorward they will combine to intensify upwelling for equatorward flow. In the case of poleward flow, terms 2 and 3 combine poleward and cancel equatorward. The model results provide examples of these phenomena in the vicinity of capes and promontories.

Maps of mean vorticity are virtually identical to Figure 6.12. However, Figure 6.13 depicts the areas of positive vorticity in agreement with the findings of Arthur (1965) where term 2 in Equation 6.2 (horizontal shear) is not negligible. Due to frequent storm passages, the wind stress increases towards land, creating positive wind stress curl and vorticity along the Oregon and Washington coasts. In the vicinity of Cape Blanco, terms 2 and 3 of Equation 5.2 combine as a result of the poleward flow around the cape. Similar results are seen near Cape Mendocino, where COAMPS forms an area of positive vorticity south of the Cape due to cyclonic curvature, and south of Monterey Bay due to poleward flow around a point. In the SCB, the positive vorticity located south of Point Conception is a combination of horizontal shear and positive wind stress curl. Generally, the results indicate a conservation of mean vorticity regardless of wind forcing. In addition, there is little evidence of interpolation error as all model results have similar structure.

B. COMPARISON TO OBSERVATION

The buoys equipped with ADCP include 46023 (Pt. Arguello, CA), 46064 (Santa Barbara, CA - West), 46062 (Pt. San Luis, CA), and MBARI (M1,M2, and M3). Tidal currents (barotropic) were calculated for each buoy location using classical tidal analysis (Pawlowicz et al., 2002). The calculated tidal current velocity is ~ 5 cm/s, reaching a maximum of ~10 cm/s, with no discernible difference detected when the buoy currents are detided (See Appendix, Figures A.1, A.2). Geographic location, water depth, distance from land, and distance to the nearest PWC and atmospheric model gridpoints are provided in Table A.1.

All model predictions underestimate the buoy 46023 current magnitude by ~ 20 cm/s with a maximum difference ~ 30 cm/s (Figure 6.14). There is agreement with the

buoy 46023 current direction (NE-NW) until 13 January before (with the exception of COAMPS 25 km) the model current reverses direction. Similar to the model results for buoy 46023, the model underestimates the current speed for buoy 46054 (Figure 6.15). All Buoy 46054 model predictions have a N-NW direction while the buoy direction alternates between SW (07-10 January), N-NW (10-12 January), SW (12-16 January) and NW-NE (17-21 January). The final NOAA ADCP Buoy, 46062 (Pt. San Luis, CA), is located 12.4 km offshore in a water depth of 378.9 m (Figure 6.16). The nearest PWC gridpoint is located 2.7 km from buoy 46062. NOGAPS, COAMPS 45 km, COAMPS 25 km and COAMPS 10 km gridpoints are located 24.5, 18.2, 6.7 and 2.7 km from the buoy 46062, respectively. Note that NOGAPS and COAMPS 25 km gridpoint distances are approximately one-half the magnitude seen in the previous buoys. All model experiment results underestimate buoy 46062 current speed, but are in good agreement with buoy 46062 current direction (NW-NE) between 07-16 January 1999. After 16 January, NOGAPS, COAMPS 45 km and COAMPS 10 km predictions show some flow in the SE direction.

MBARI buoys M1, M2, M3 are located 17.3, 34.5 and 39.3 km from land in waters depths of 1600, 1800, and 3000 m, respectively. Note that COAMPS 45 km has the nearest gridpoints to buoys M1 (1.7 km) and M2 (3.3 km), and farthest gridpoint to M3 (9.9 km). NOGAPS and COAMPS 10 km are almost collocated at M2 (4.7/4.6km) while COAMPS 25 km has the largest gridpoint distance at M1 (9.8 km). This is an example of how the various horizontal COAMPS grid orientations may not guarantee a direct relationship between horizontal grid size and horizontal resolution in the coastal region. The model predictions underestimate the MBARI buoy current speed by 10-15 cm/s, and model current direction is mostly southward. In contrast, MBARI current direction is variable for buoys M1 and M2, and mostly southward for M3 (Figures 6.17-6.19). This result indicates that the CC has a relatively stronger influence on the outer part of Monterey Bay (SE flow at M3) with alternating influence of the CC and local wind forcing taking place within Monterey Bay (e.g., variable current directions at M1 and M2). The southward model currents also imply that the horizontal resolution of the

ocean model and/or atmospheric models may require smaller grid spacing and/or time steps to resolve the conditions in the bay.

In most cases, buoy and model wind stress are opposite (southward) to current flow (northward), especially for the NOAA buoys. MBARI buoy and model wind stress are mostly in agreement with model current direction still opposed to the buoy current direction. The NOAA buoys are located south of Monterey Bay and within 12-26 km of the coast. The northward current flows in opposition to the local wind forcing and implies that the 25-29 m depth velocity is strongly influenced by the DC (Ramp et al., 1997). The MBARI buoys are influenced by the CC, DC and local wind forcing. Located the farthest offshore, the results imply that buoy M3 is strongly influenced by the CC. The variability seen in buoys M1 and M2 is probably a combination of the DC (Ramp et al., 1997) and local wind forcing.

Buoy current autocorrelations (not shown) are in agreement with integral time scales ~12-hours. Buoy wind stress show small, negative cross-correlations (not shown) with model current, except for buoy 46062 which shows high buoy/model current correlations (~0.75). Generally, model current speed RMSE has a range of 7-20 cm/s for water depths of 25-29 m. With the exception of buoy 46023 (Figure 6.20), the COAMPS results have the lowest RMSE (not shown). NOGAPS has the lowest RMSE for buoy 46023.

With the exception of M1 and M2, COAMPS 45 km grid points are located farther from the buoy locations compared to COAMPS 25 km and COAMPS 10 km. However, COAMPS 45 km and COAMPS 45 km with QuikSCAT outperform the other COAMPS predictions in terms of RMSE for buoys 46023, 46062 and M1(Figures 6.20-6.22). COAMPS 25 km and COAMPS 10 km have the lowest RMSE for buoys 46054 and M2, respectively. In the case of M2, COAMPS 45 km gridpoints are located closer to the buoy compared to COAMPS 25 km and COAMPS 10 km. No discernible difference in RMSE is detected between model results for buoy M3. In all cases the model runs underestimate (negative ME) the buoy currents. Thus the RMSE results are another example of how the various horizontal COAMPS grid orientations may not

guarantee a direct relationship between horizontal grid size and horizontal resolution in the coastal region.

C. CODAR

The average depth observed based on the radar operating wavelength, is 0.5 m. Horizontal resolution is 2 km with each CODAR gridpoint representing the center of a 2 x 2 km box. CODAR measurements are recorded every two hours, and each measurement is the result of 26 minutes of radar transmissions. Average surface current velocity and direction rms errors are +/- 2-3 cm/s and +/- 2.5 degrees, respectively. Radar currents are also known to have significant divergences and unrealistic spatial variations of divergence, so the CODAR currents are interpreted with caution (Neal, 1992).

CODAR currents during the period of 07-11 January 1999 have a strong tendency for northward flow outside of Monterey Bay (Figures 6.23,6.24). This patterns shifts to southward flow outside of the Bay only briefly (12-14 January) before returning to northward flow (15-20 January). In contrast, model currents are a reflection of the California Current and are mostly southward outside of the Bay, sometimes changing to eastward into Monterey Bay. Inside Monterey Bay, CODAR has several spatial variations and divergences.

In the previous section, M2 showed mostly NW flow while M1 and M3 had variable current directions. All three buoys show some SW flow by 18 January, especially M1. The MBARI buoys reflect the variability within Monterey Bay that is a result of the combination of local wind forcing and the inflow of the California Current. The most significant difference between the model runs is how they treat the flow in the vicinity of Point Pinos (northward south of Point Pinos turning to northwestward into the Bay). Figures 6.23 shows the difference between model runs on 20 January 1999. The northward flow near Point Piños increases with increasing atmospheric model horizontal resolution. The COAMPS 25 km run on 21 January (0000 UTC) has good agreement with CODAR currents (not shown). This is significant in that the ocean grid remains

fixed while the atmospheric model horizontal resolution increases, bringing closer agreement between the model and CODAR currents.

In previous studies, the circulation in Monterey was found to be strongly influenced by the circulation offshore. It is also connected to the waters offshore at deeper levels through the Monterey Submarine Canyon. The offshore circulation is also complicated by the presence of meanders and eddies. Thus, the oceanic conditions in Monterey Bay can change within just a few days. This could partially explain the differences found between ocean model and CODAR currents. CODAR has a temporal resolution of two hours. Thus, unlike the atmospheric models (three-hourly), the ocean model may be unable to respond to changes that are occurring within two hours. Future research will require wind sampling on the order of one hours (output every two hours), and an ocean model with a horizontal grid ~ 1 km and non-hydrostatic physics for a fair comparison of the ocean model to CODAR.

D. CALCOFI

There is good agreement with the NAVOCEANO cruise ADCP surface currents. Generally, there are small differences in direction and intensity between the model runs. As previously seen in the buoy data and CODAR, the model currents tend to underestimate the actual currents by ~10-15 cm/s and have occasional difficulty predicting the flow direction within Monterey Bay, respectively.

For example, there is agreement between the NOGAPS experiment and CalCOFI field on 10 January (not shown). With both the field data and ocean model revealing a cyclonic eddy located southwest of San Francisco. Just west of the cyclonic eddy, the model current and field data also show eastward inflow into the eddy at 124-123.5^{o} W. Similarly, in Figure 6.24 (COAMPS 10 km run on 13 January), there is strong CC inflow into Monterey Bay from the west and DC inflow from the south in the vicinity of Point Piños. As in the case of CODAR, the oceanic conditions within the bay are not fully resolved. In the only significant difference between the model runs, COAMPS 10 km has the tendency to weaken the DC current along the coast before reaching Monterey Bay.

Bay. On 16 January the ocean model (COAMPS 25 km run) captures the northward DC in the vicinity of Point Piños, anticyclonic turning near 35.6^{o} N, 123-122° W, and CC meander at 123.5^{o} W (Figure 6.25). A similar situation exists on 18 January (COAMPS 45 km w/QuikSCAT run) but the ocean model is unable to resolve the strong (~40-50 cm/s) DC inflow into Monterey Bay. In the ocean model, the DC turns westward without entering the Bay (Figure 6.26).

E. DISCUSSION AND SUMMARY

As in the case of wind stress, there is little difference between the COAMPS 45 km and COAMPS 45 km with QuikSCAT. The higher wind stress provided by the COAMPS experiments is translated to the ocean in the form of higher ocean currents and EKE. EOF and EKE maps shows the majority of the current variance located along the Oregon and Washington coast as a result of winter storms. In terms of ocean structure, the COAMPS wind forcing provides better-defined, closed circulations (eddies). In terms of forecast accuracy, no observations were available to validate the eddy fields. The areas of positive vorticity near capes and promontories are in good agreement with the vorticity equation but may be an artifact of land contamination. Generally, there is no difference in mean vorticity between the model epxeriments.

In Chapter 5, the structures of important mesoscale features often become more realistic (stronger, better defined) as resolution increases. However, objective verification can be degraded by even small timing and spatial errors (Mass et al., 2002). For example, atmospheric models may have systematic tendencies to move fronts too quickly or too slowly. In this study, an additional time error may result from the 3-6 hour requirement for the dynamic adjustment of the wind stress in COAMPS. For example, Table 2.2 shows that the 3-hour forecast is also used for the analysis which may introduce forecast errors as a result of the 3-hour lag in wind stress. Ocean inertial oscillations are often a response to strong or sudden changes in wind forcing on a time scale equal to 1/f (~12 hours), where f is the coriolis parameter. No comparison is made between COAMPS/NOGAPS wind forcasts and buoy observations to see that frontal propagaton

in the models agree with reality. However, because this inertial time scale is approximately equal to the PWC 12-hour output, a systematic bias in frontal propagation speed of 12-24 hours may cause phase differences between buoy and model observations. For example, currents in Monterey Bay are influenced by the DC and CC in addition to local forcing. An error in atmospheric model frontal propagation may be the difference in the shift between equatorward and poleward directed winds and associated anticyclonic and cyclonic surface current flow within Monterey Bay.

The ocean model predictions demonstrate the expected climatological features and variability of the CCS. However, the amplitude of current fluctuation is generally underpredicted (Hickey, 1998; Brink et al., 1994). Comparisons to CalCOFI observations indicate that the ocean model produces a realistic structure but underestimates the current amplitude for all model predictions. In comparisons of model current to ADCP buoys, the model currents also underestimate the observed current amplitude. Generally, the ocean model current direction reflected the variability of CalCOFI data. Similarly, model currents have better, but still poor, agreement with CODAR observations with higher resolution COAMPS experiments, particularly in revealing the flow around Point Piños into Monterey Bay. This can be the result of insufficient spatial (~10 km) and temporal (three-hourly wind stress) resolution. There may be a need for improved model physics (nonhydrostatic) to resolve the oceanic variability (e.g., baroclinic tides) within Monterey Bay.

A comparison of NOAA buoy data indicates that the direction of the model currents often followed the offshore flow, sometimes in opposition to the observed direction. The impact of detiding buoy data was negligible (~5 cm/s). Thus, the offshore (CCS) and inshore currents (DC) may mask the variability that can be attributed to local wind forcing, bottom topography, baroclinic tides, transient coastal waves, and nonhydrostatic model physics. Within Monterey Bay, the flow at intermediate depths (~25-150 m) and deeper, can be either cyclonic or anticyclonic depending on the conditions of the bay. In either situation, the flow at the surface may be opposite to the flow at depth, indicating the existence of a two-layer system of circulation in Monterey Bay (Breaker and Broenkow, 1994; Rosenfeld et al., 1994). The MBARI buoys M1 and

M2 are reflective of the oceanic conditions within the Bay and the influence of the DC, while M3 reflects the intrusions of the CC. Overall, NOGAPS has the lowest RMSE for buoy 46023 while COAMPS 45 km and COAMPS 45 km with QuikSCAT outperform the other COAMPS runs for buoys 46023, 46062 and M1. COAMPS 25 km and COAMPS 10 km have the lowest RMSE for buoys 46054 and M2, respectively. No discernible difference in RMSE is detected between model experiments for buoy M3. In all cases the model predictions underestimate (negative ME) the buoy currents.

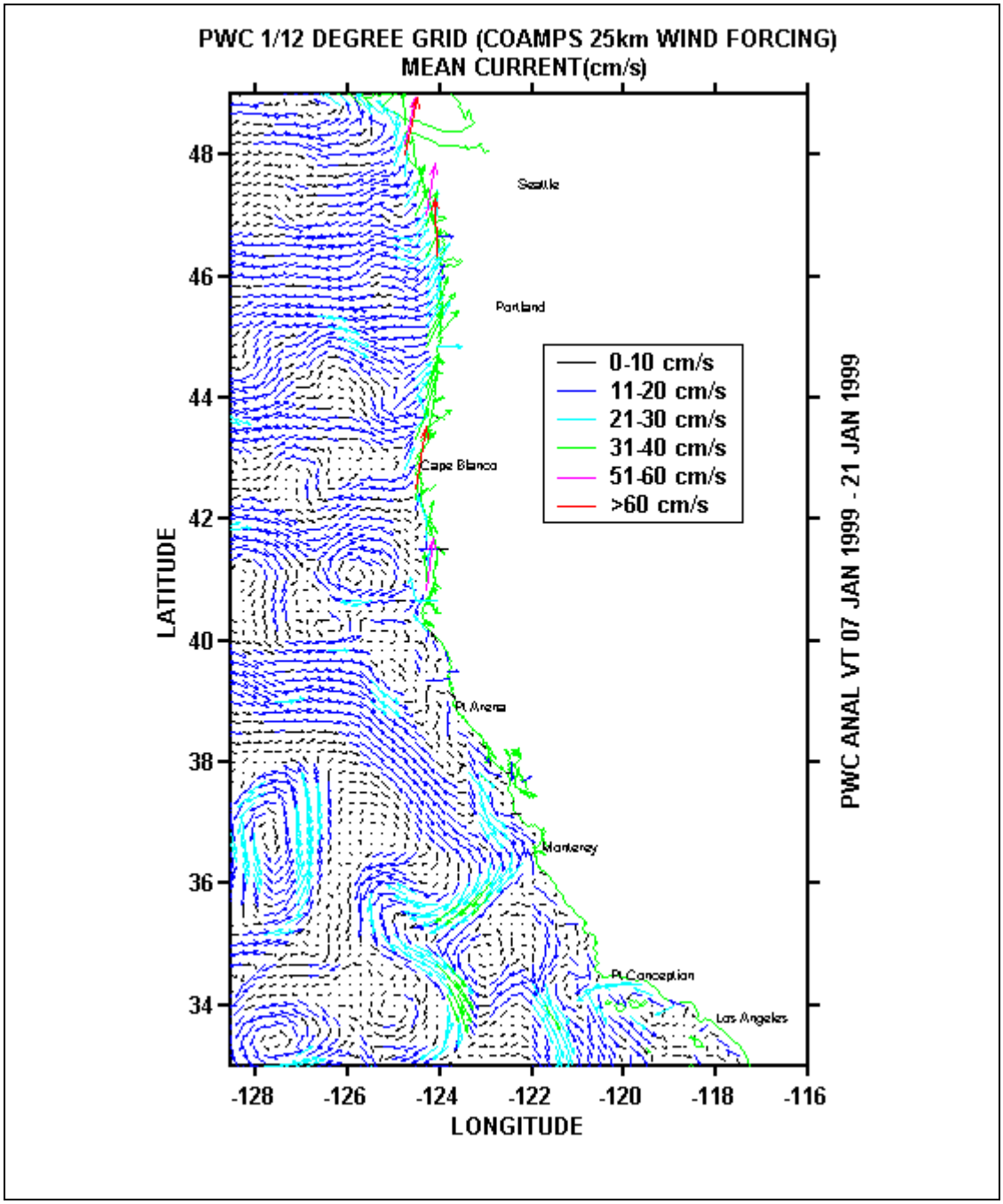

Figure 6.1. COAMPS 25 km mean current speed.

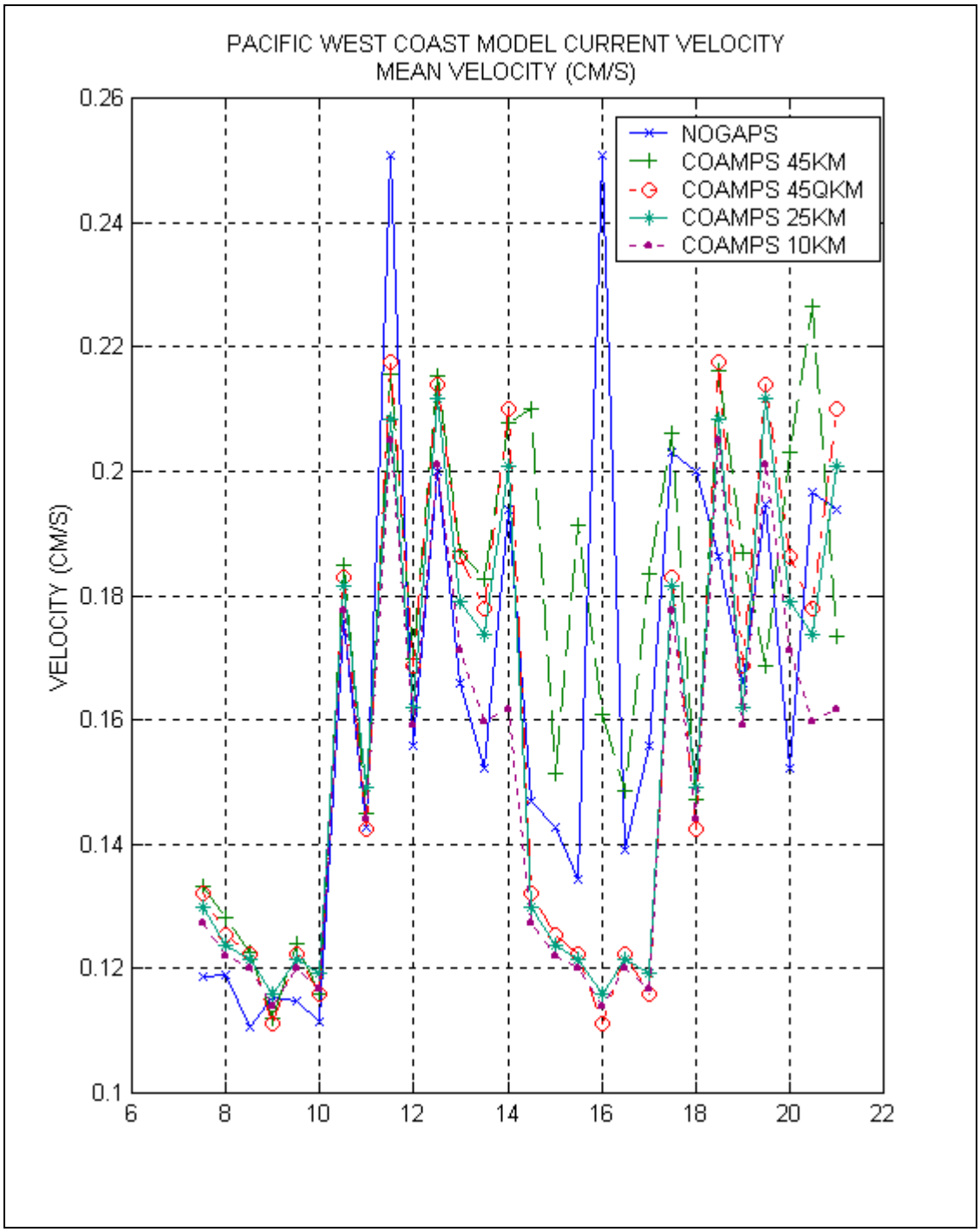

Figure 6.2. PWC mean surface current speed.

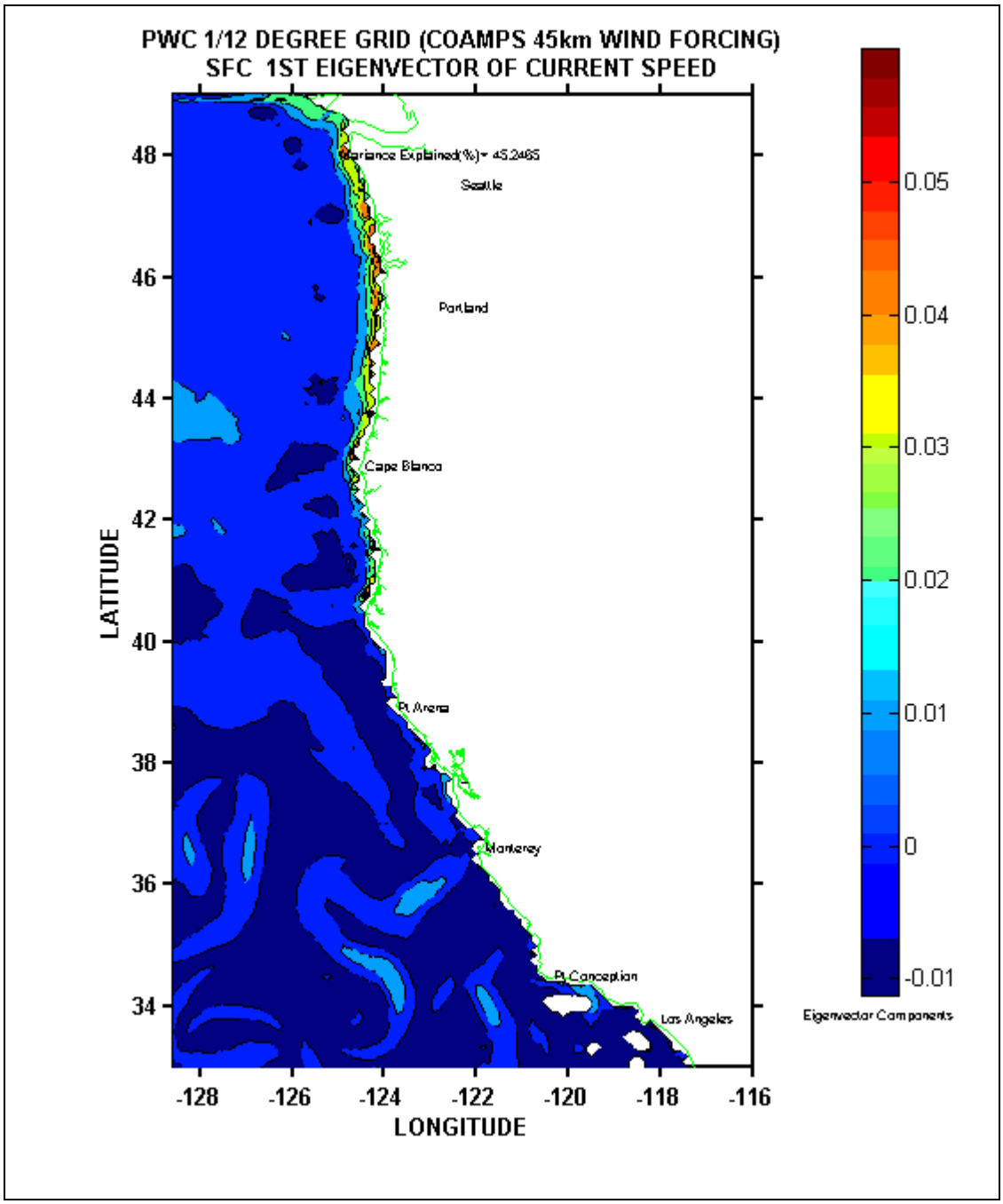

Figure 6.3. COAMPS 45 km first EOF of current speed.

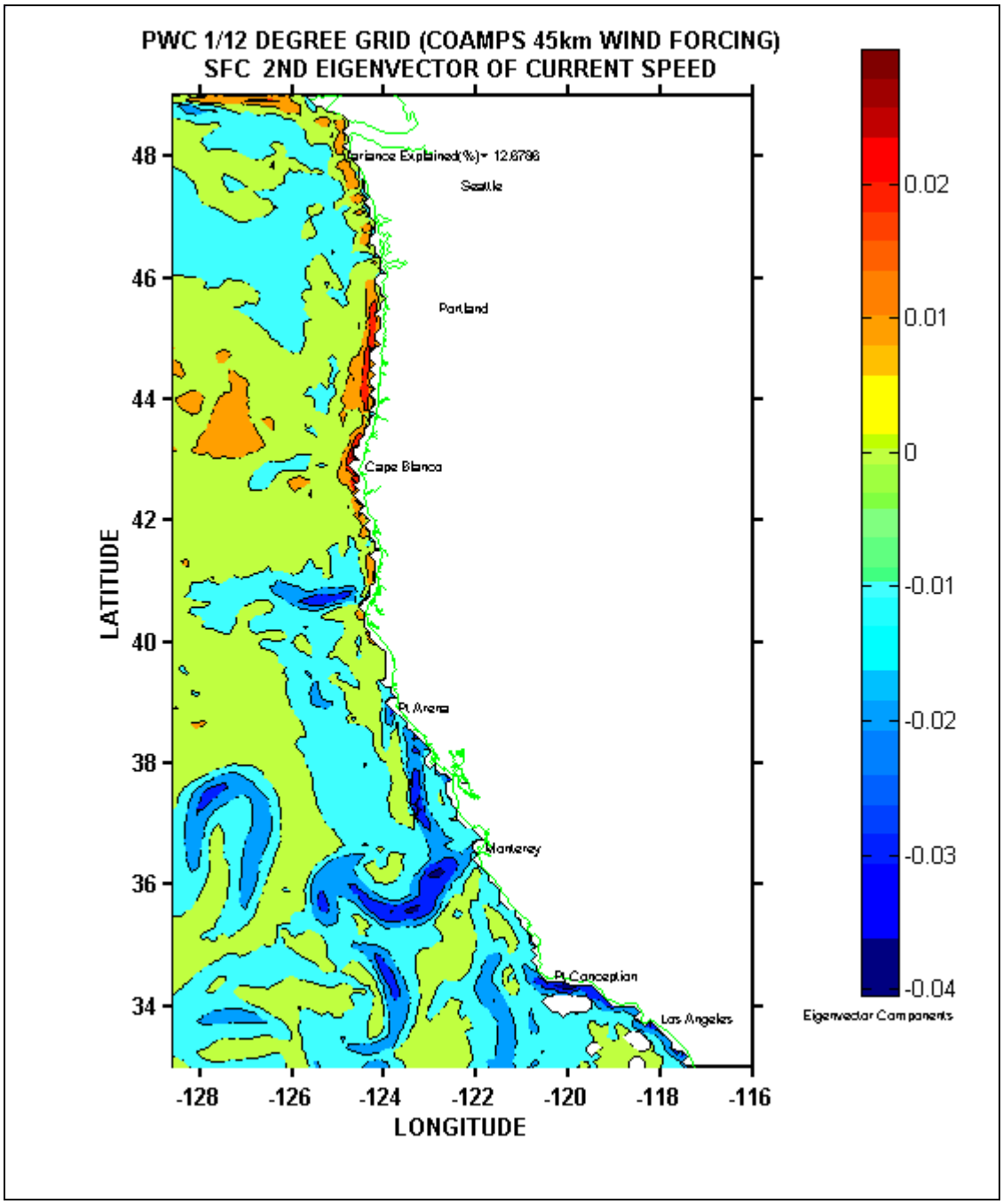

Figure 6.4. COAMPS 45 km second EOF of Current speed.

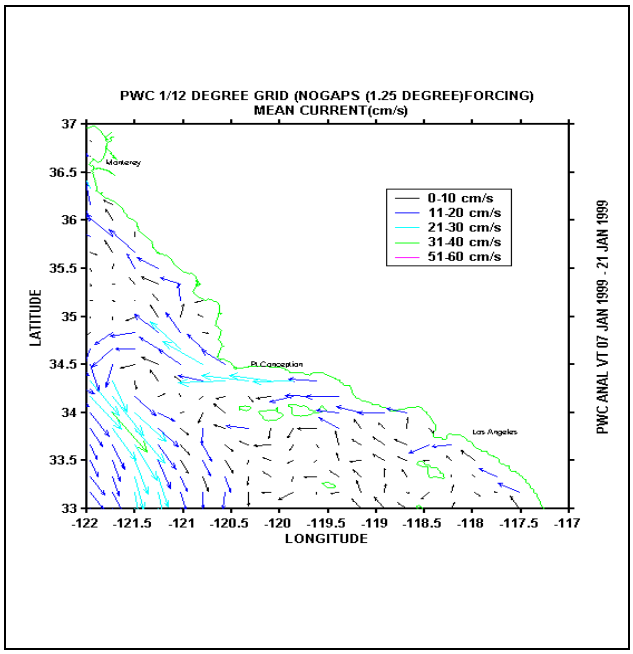

A

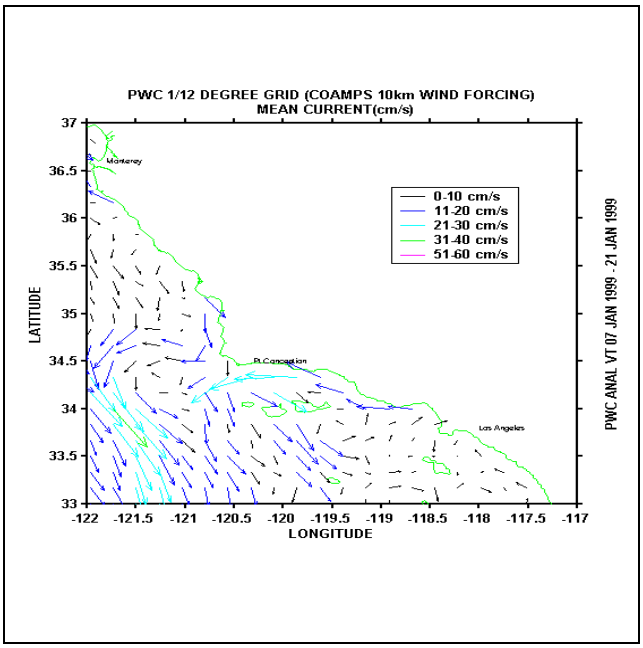

B

Figure 6.5. Southern California Bight (COAMPS 10 km).

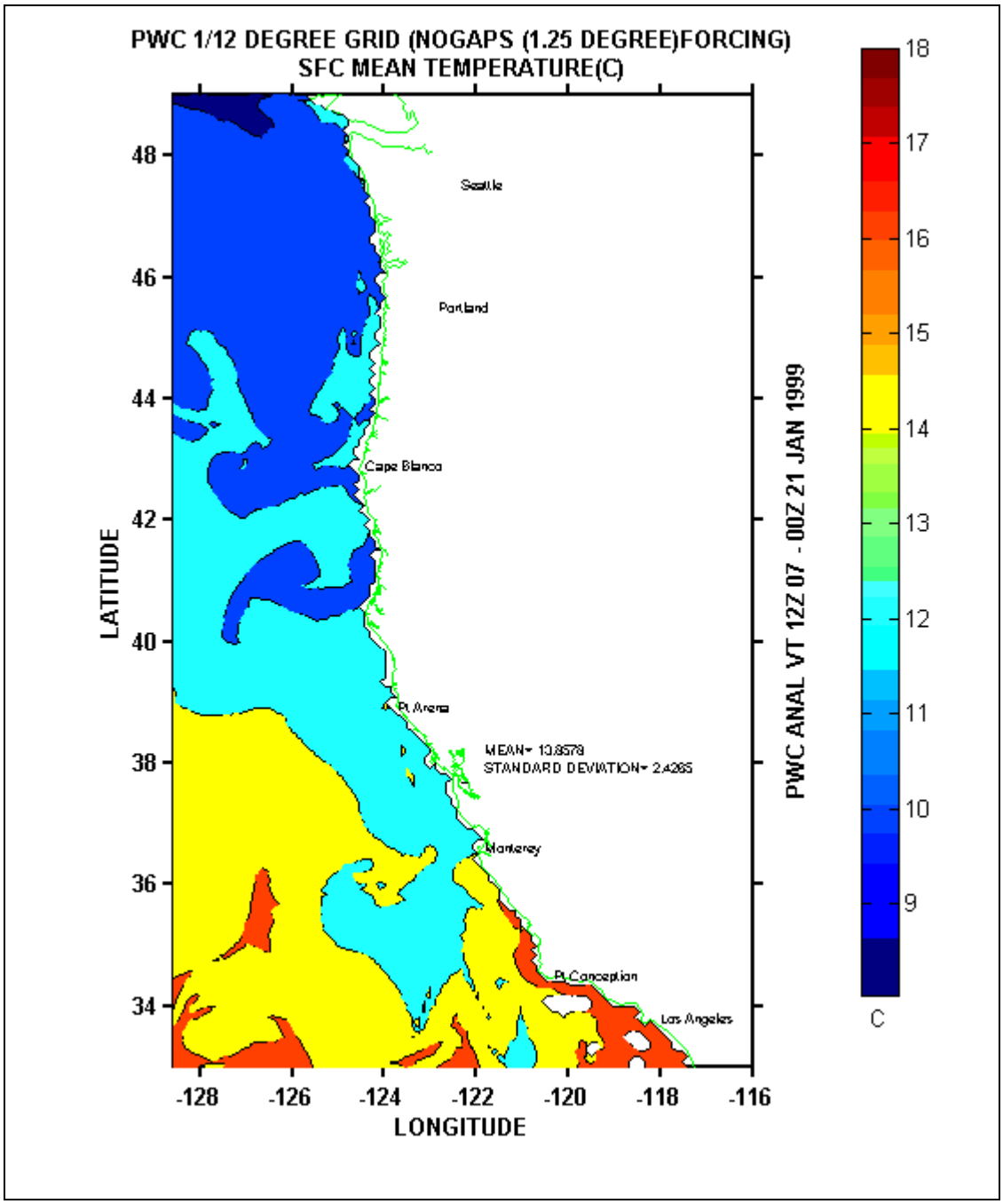

Figure 6.6. PWC SST 07-21 January 1999 (NOGAPS).

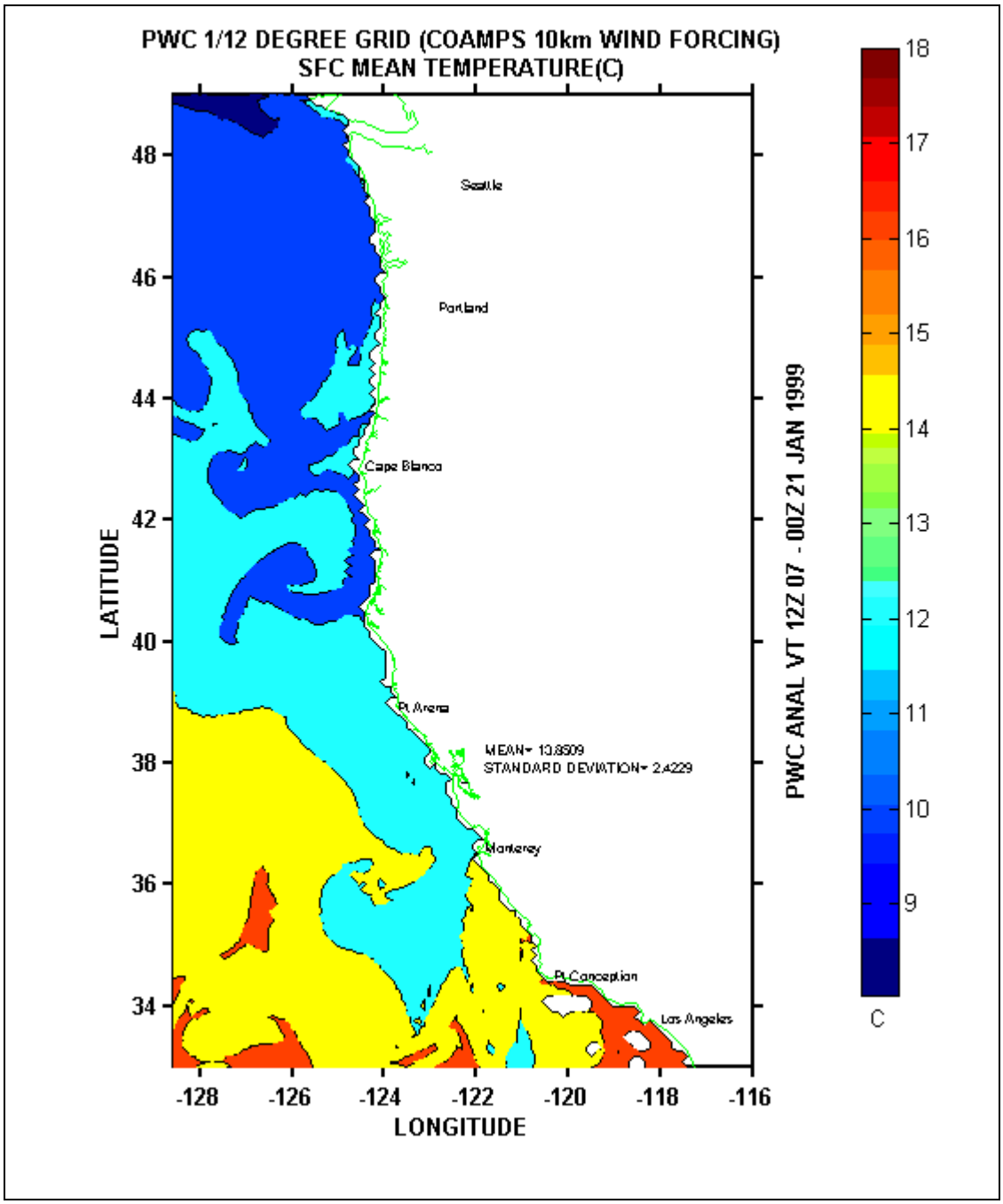

Figure 6.7. Same as Figure 6.6, except for COAMPS 10 km.

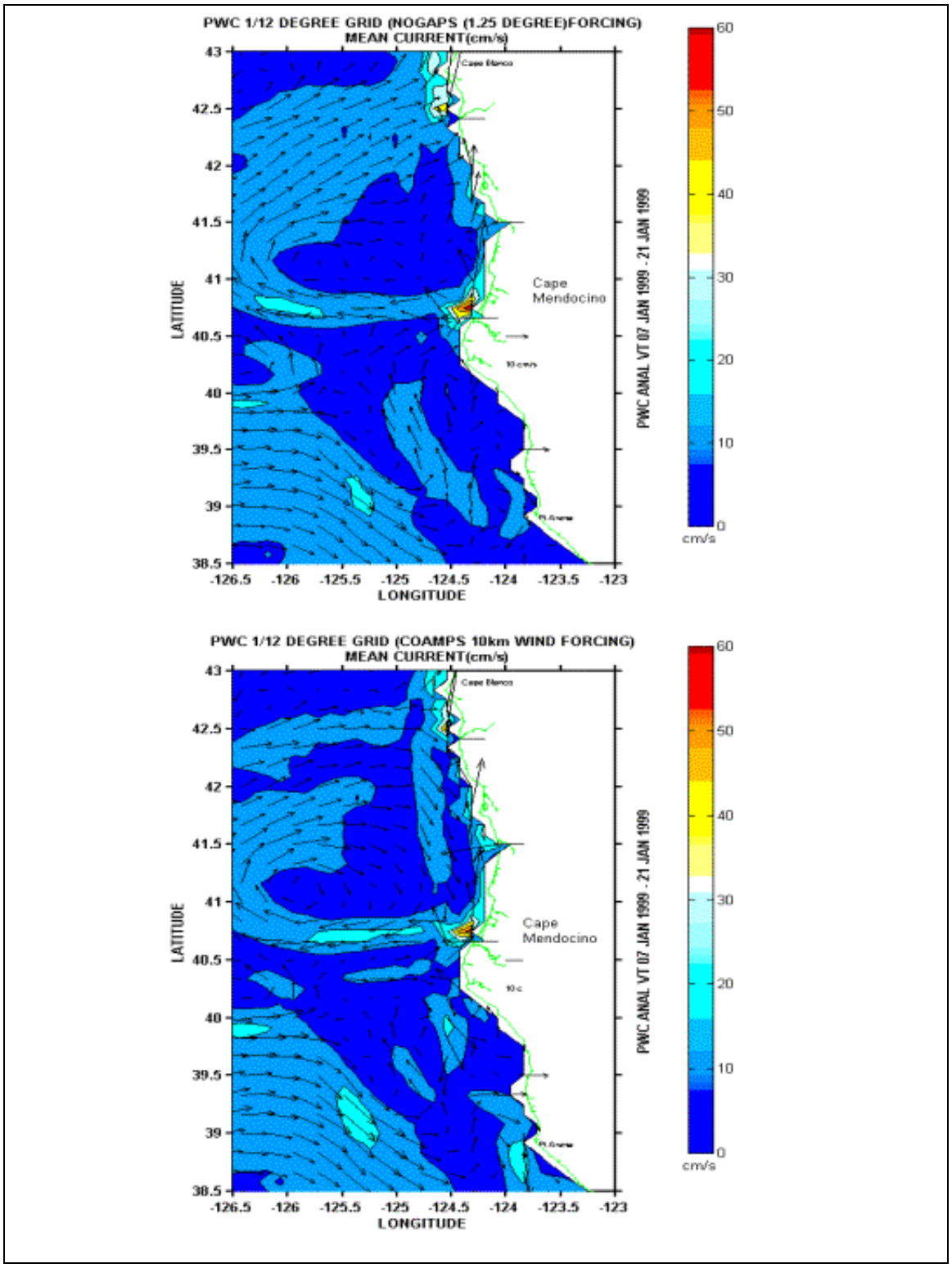

Figure 6.8. Mean current in the vicinity of Cape Mendocino.

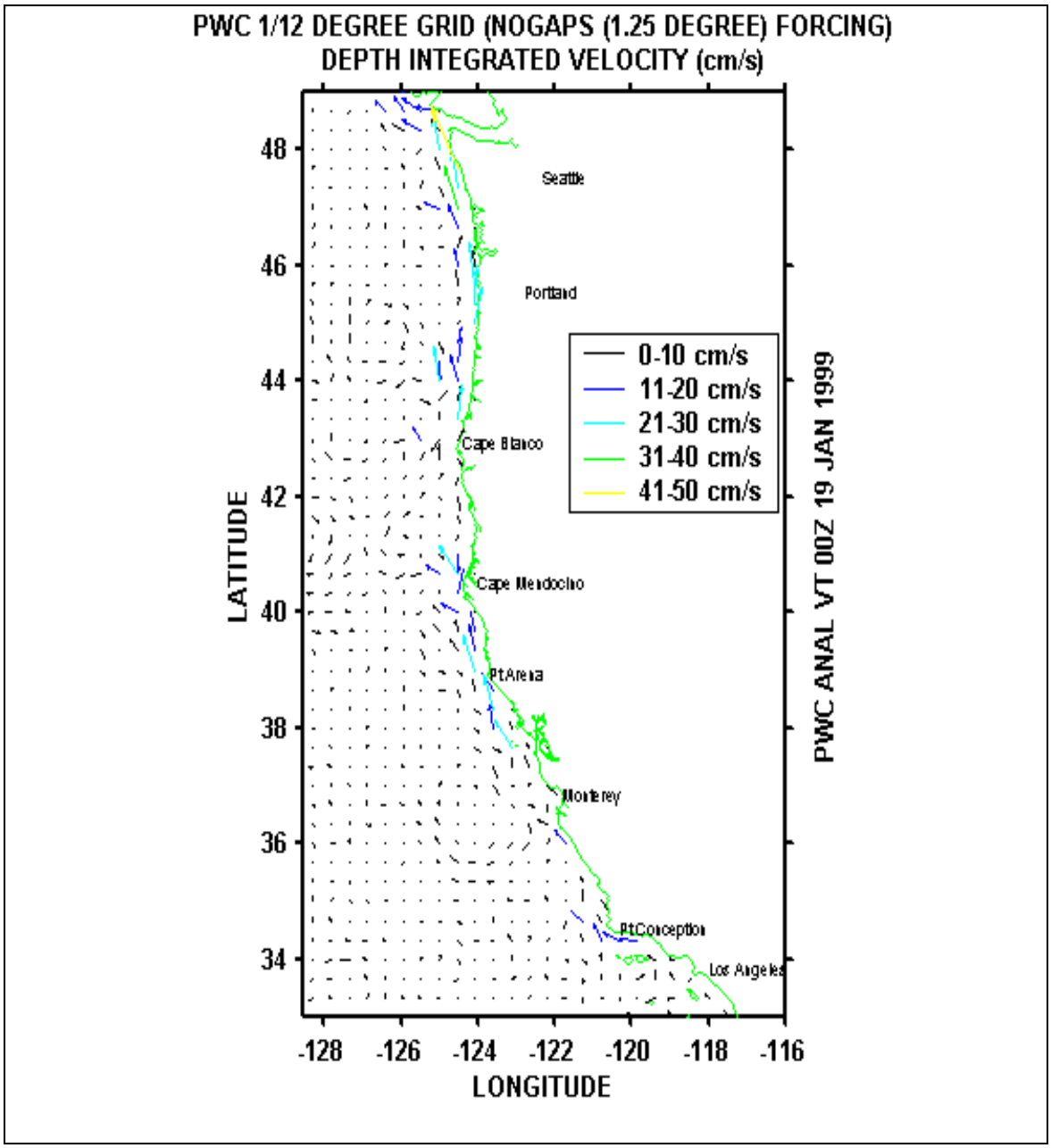

Figure 6.9 Depth integrated current for 00 UTC, 19 January 1999 (NOGAPS).

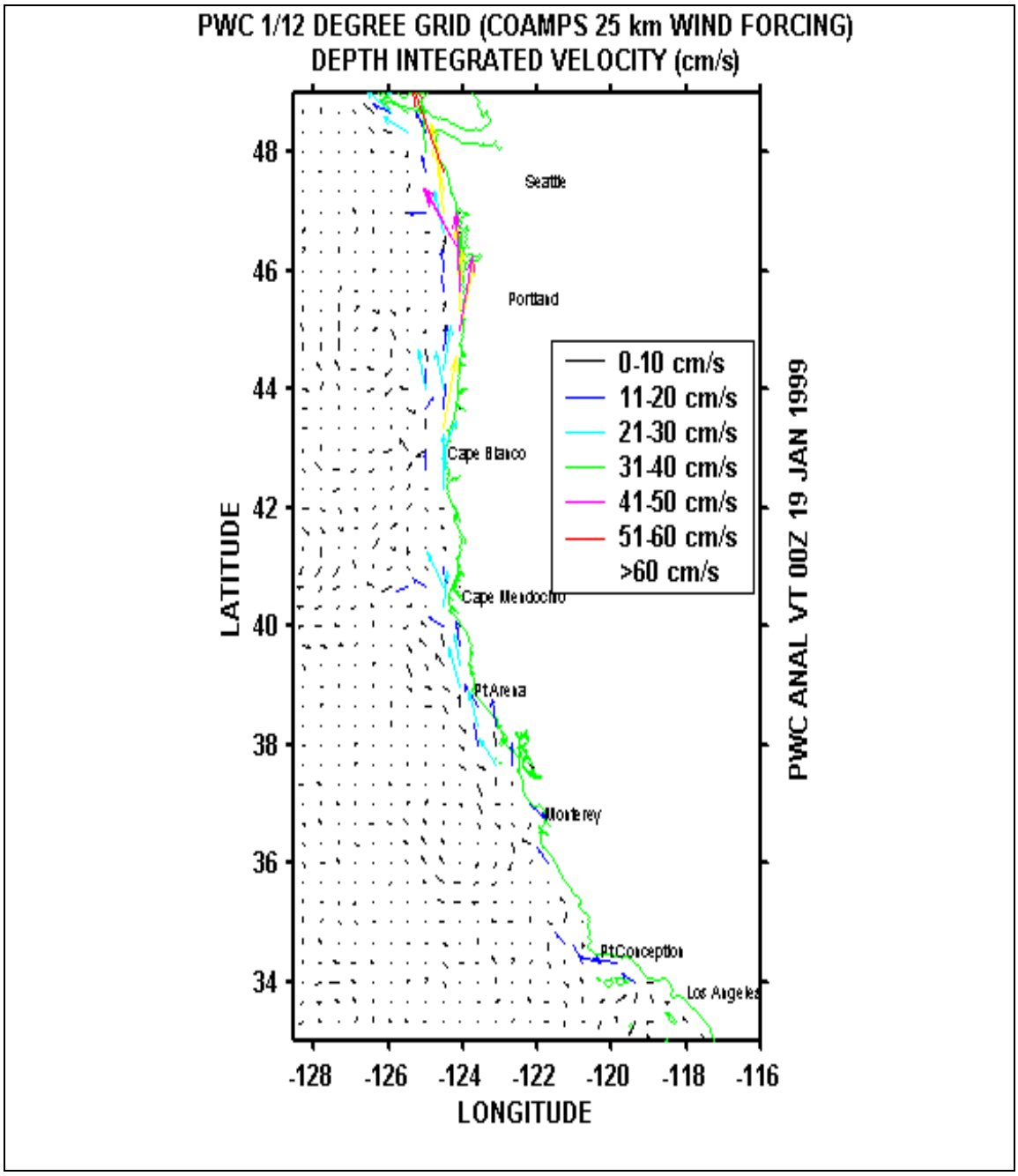

Figure 6.10 Same as Figure 6.9 except for COAMPS 25 km.

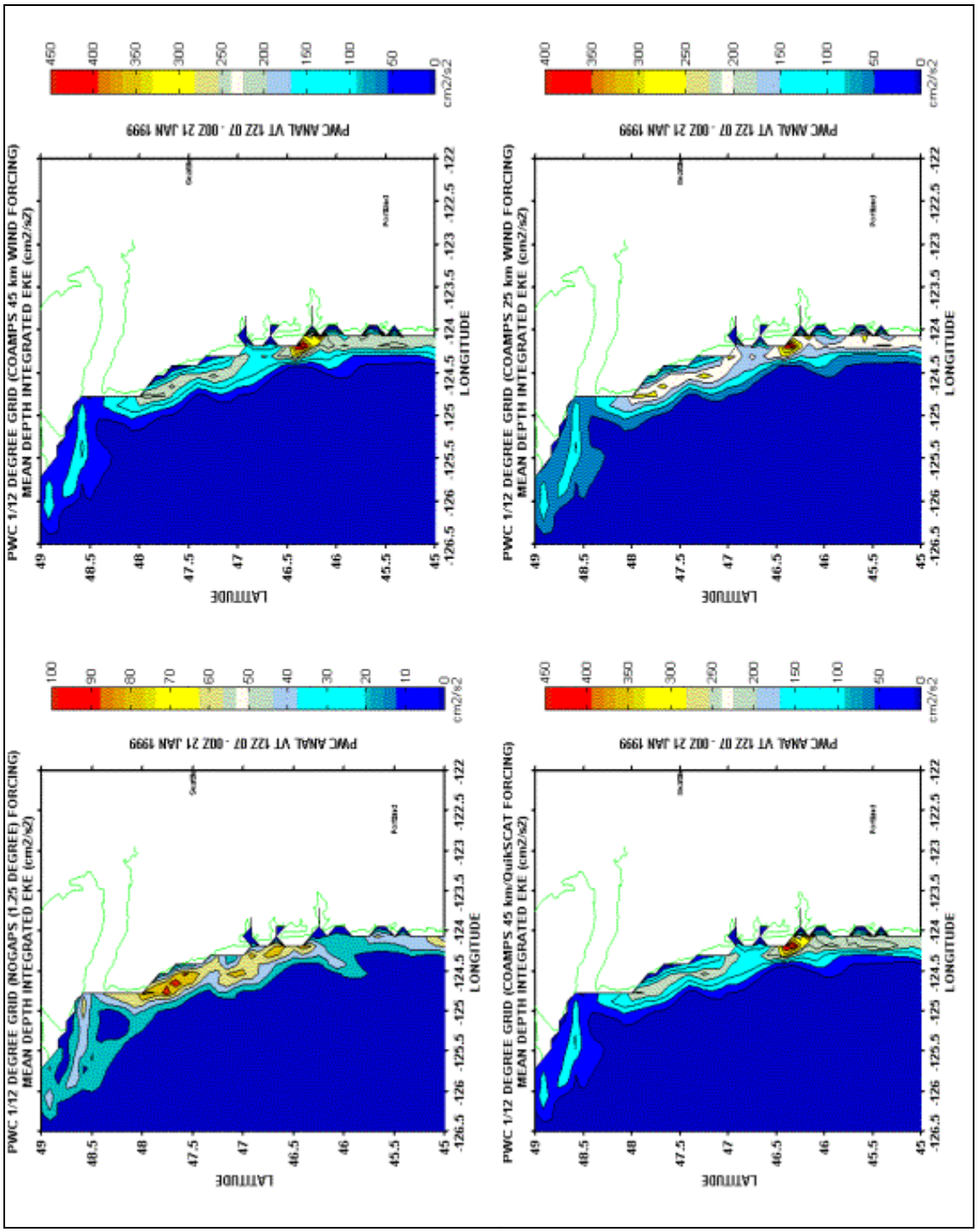

Figure 6.11 Washington coast mean depth integrated EKE .

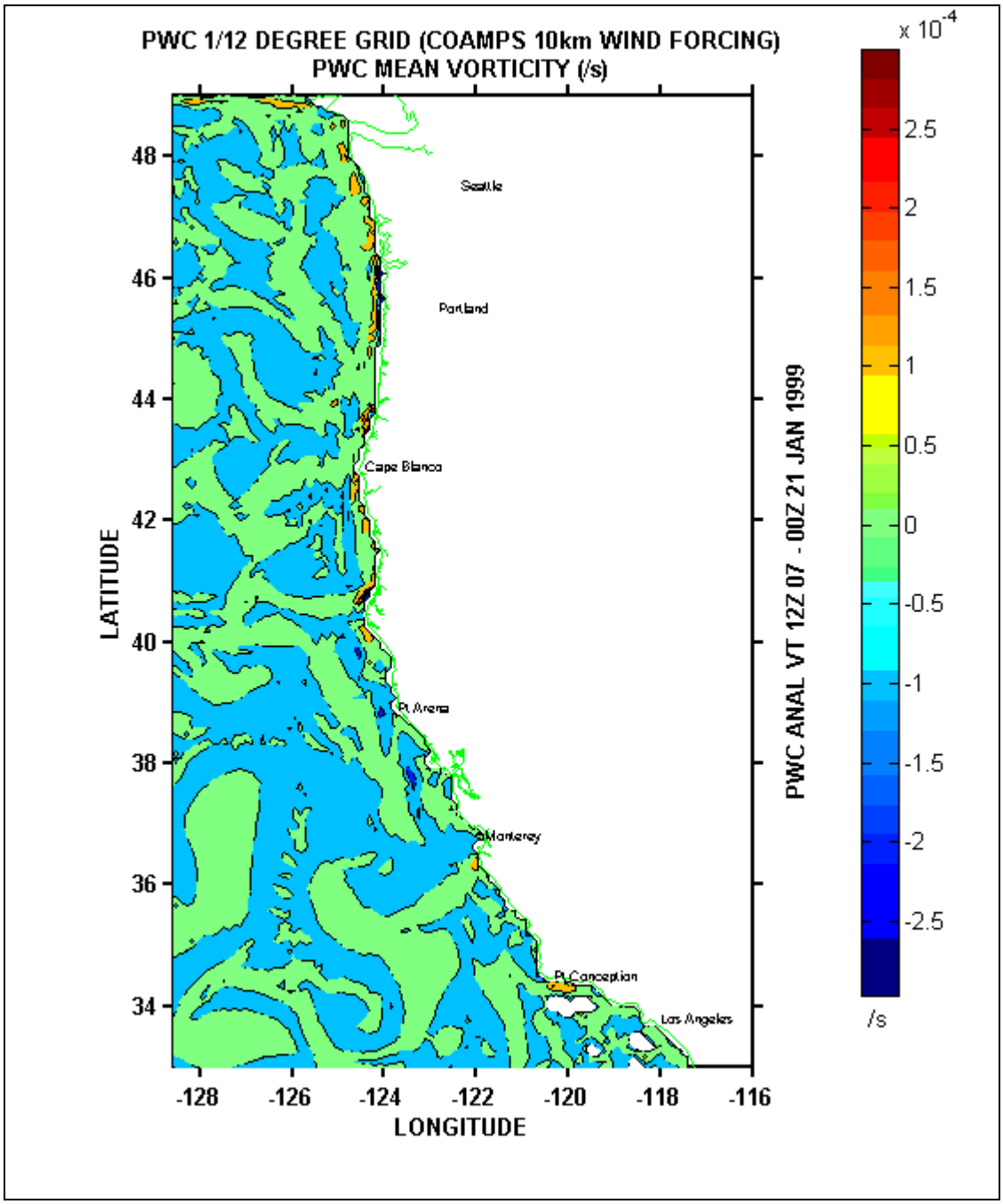

Figure 6.12 PWC mean surface current vorticity (COAMPS 10 km).

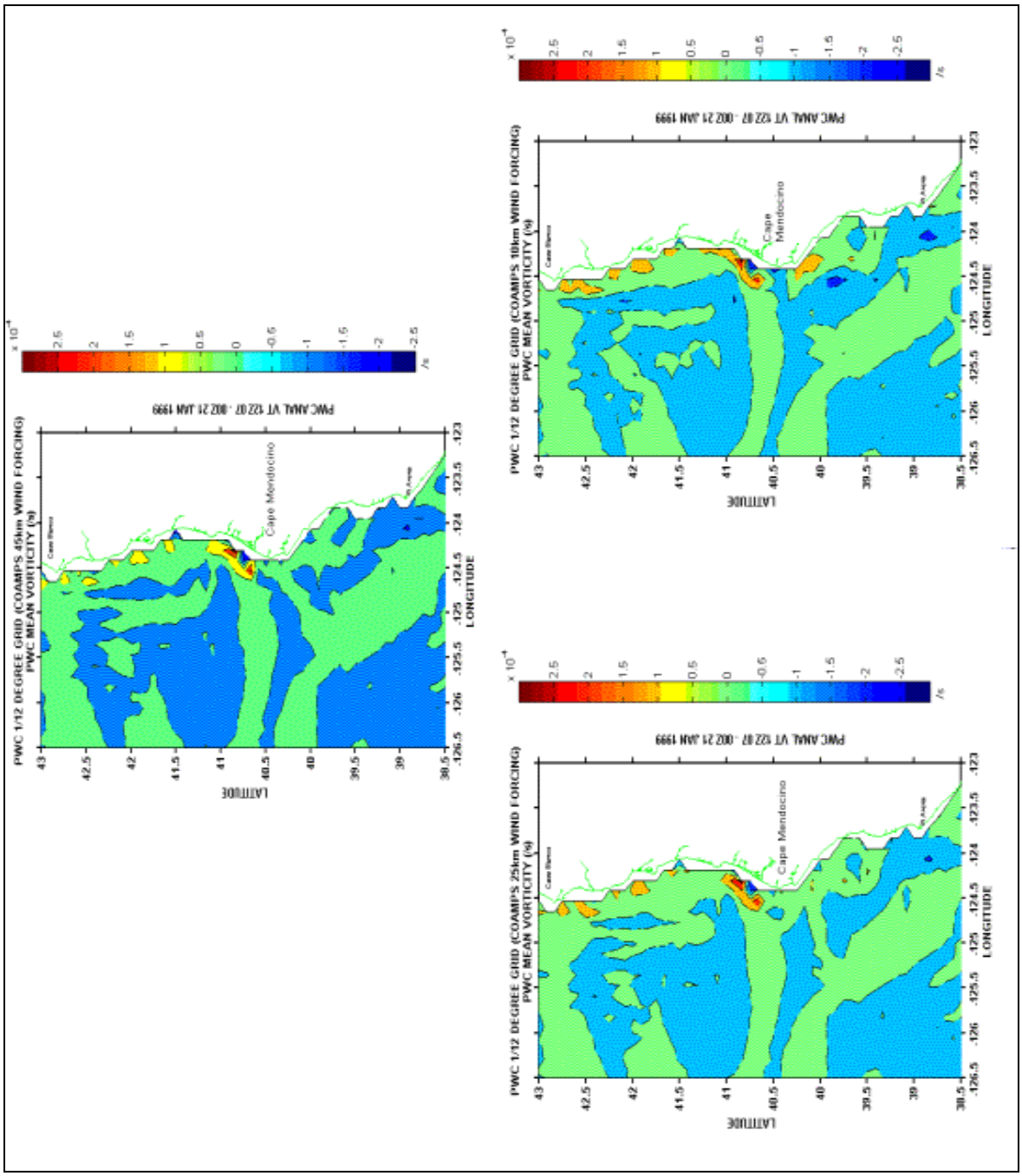

Figure 6.13. Mean current vorticity for vicinity of Cape Mendocino.

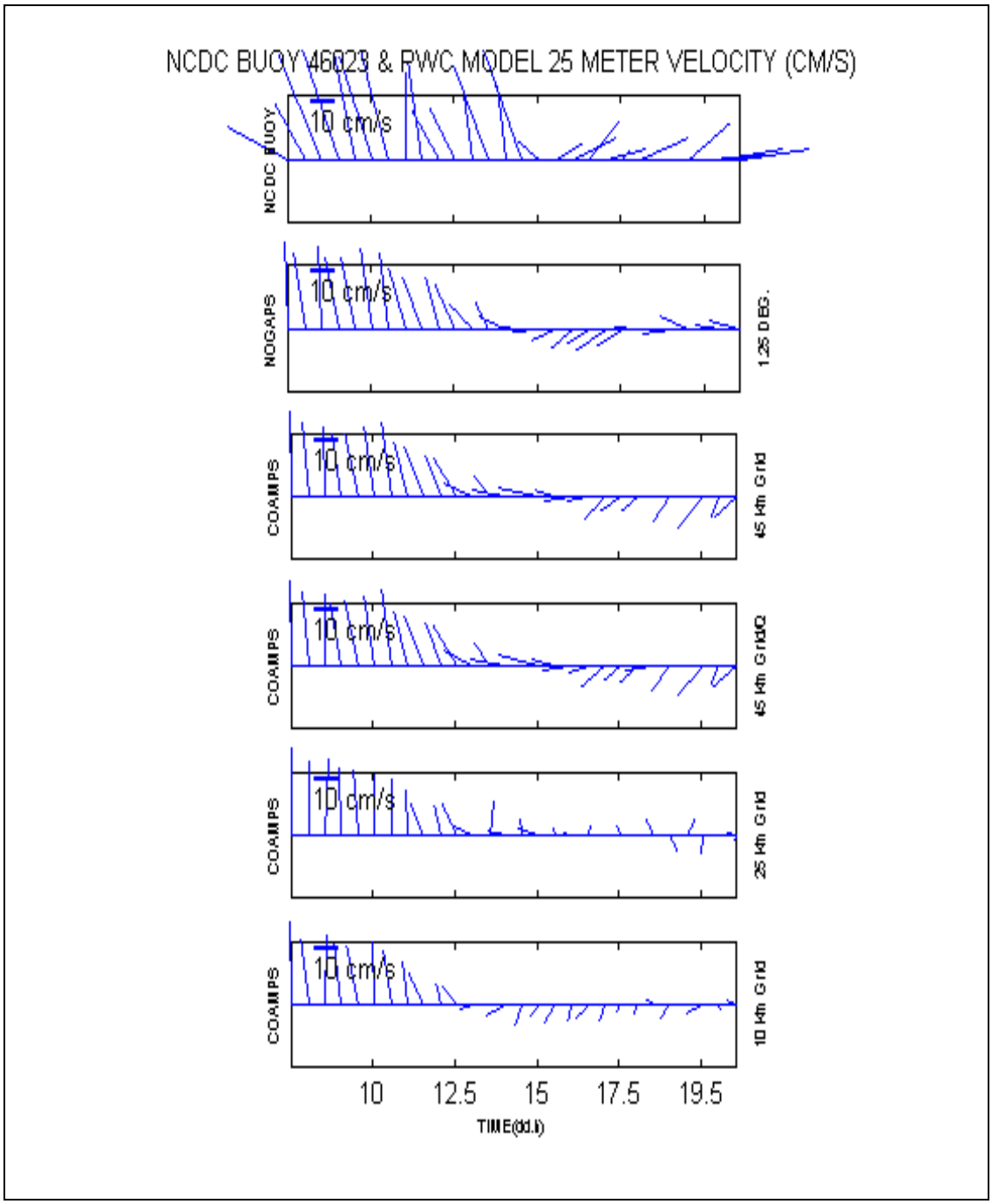

Figure 6.14. NDBC buoy 46023 (Pt. Arguello) ADCP 25 m depth velocity.

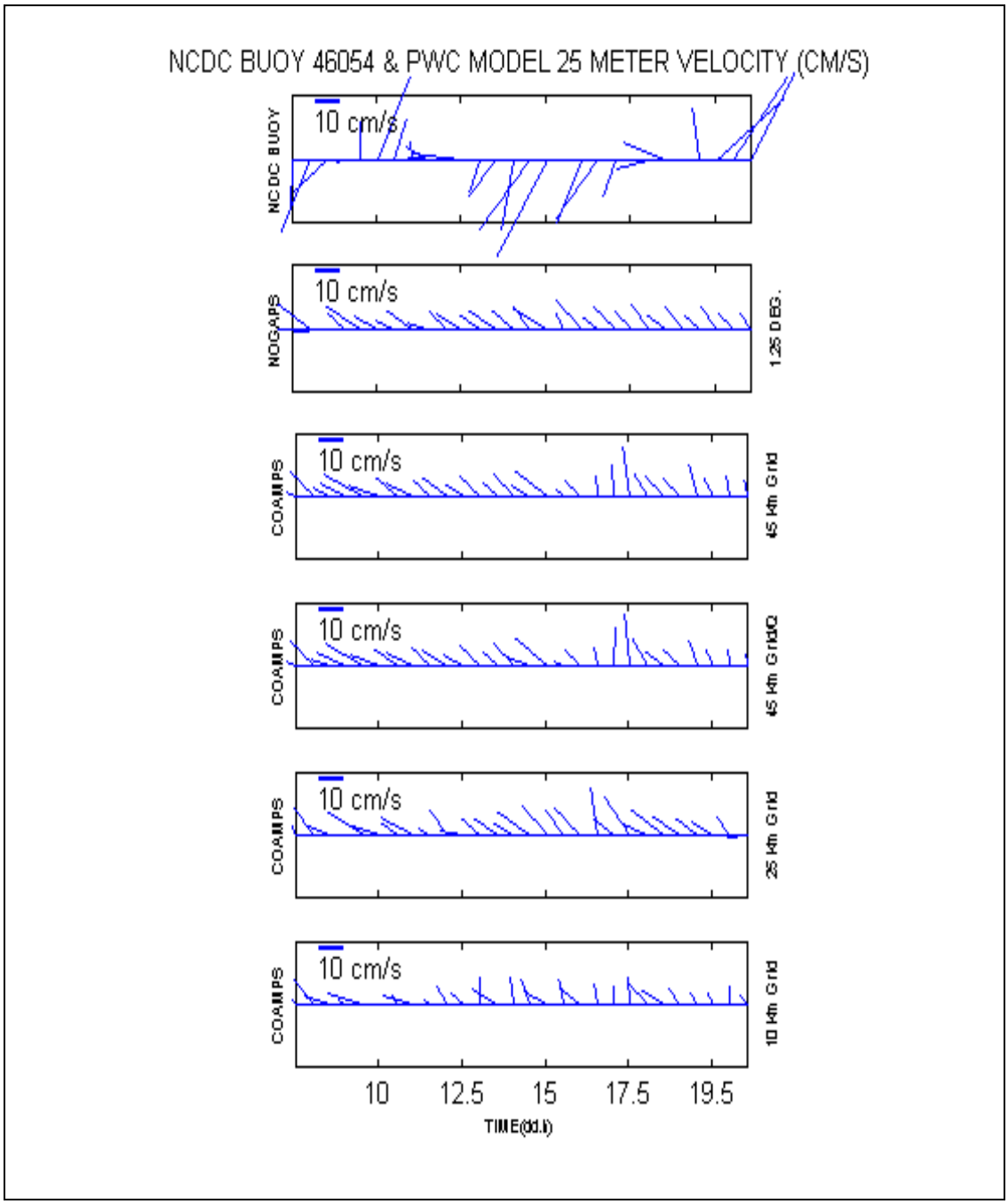

Figure 6.15. Same as Figure 6.15, except for buoy 46054 (Santa Barbara, West).

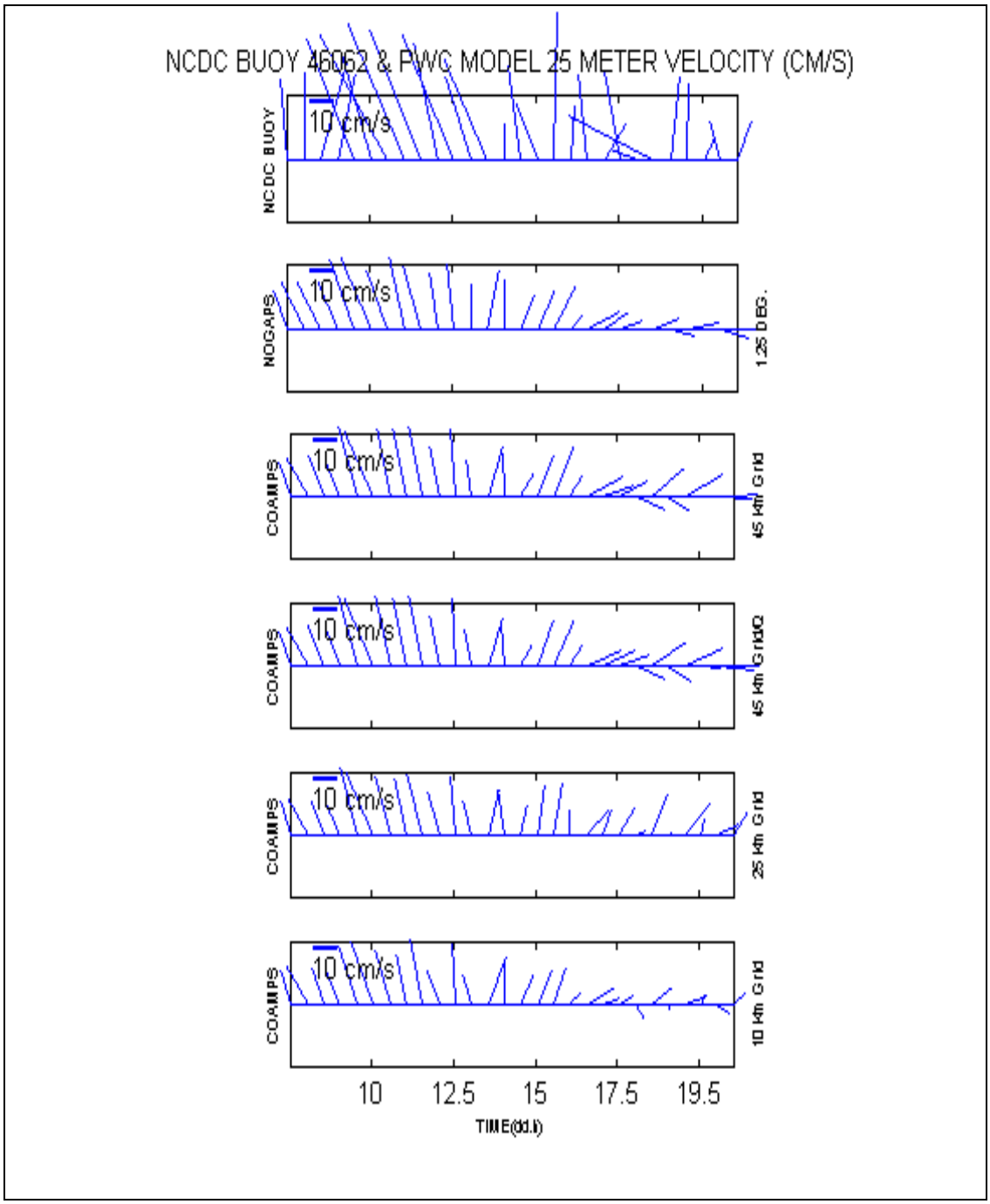

Figure 6.16. Same as Figure 6.15, except for buoy 46062 (Pt. San Luis).

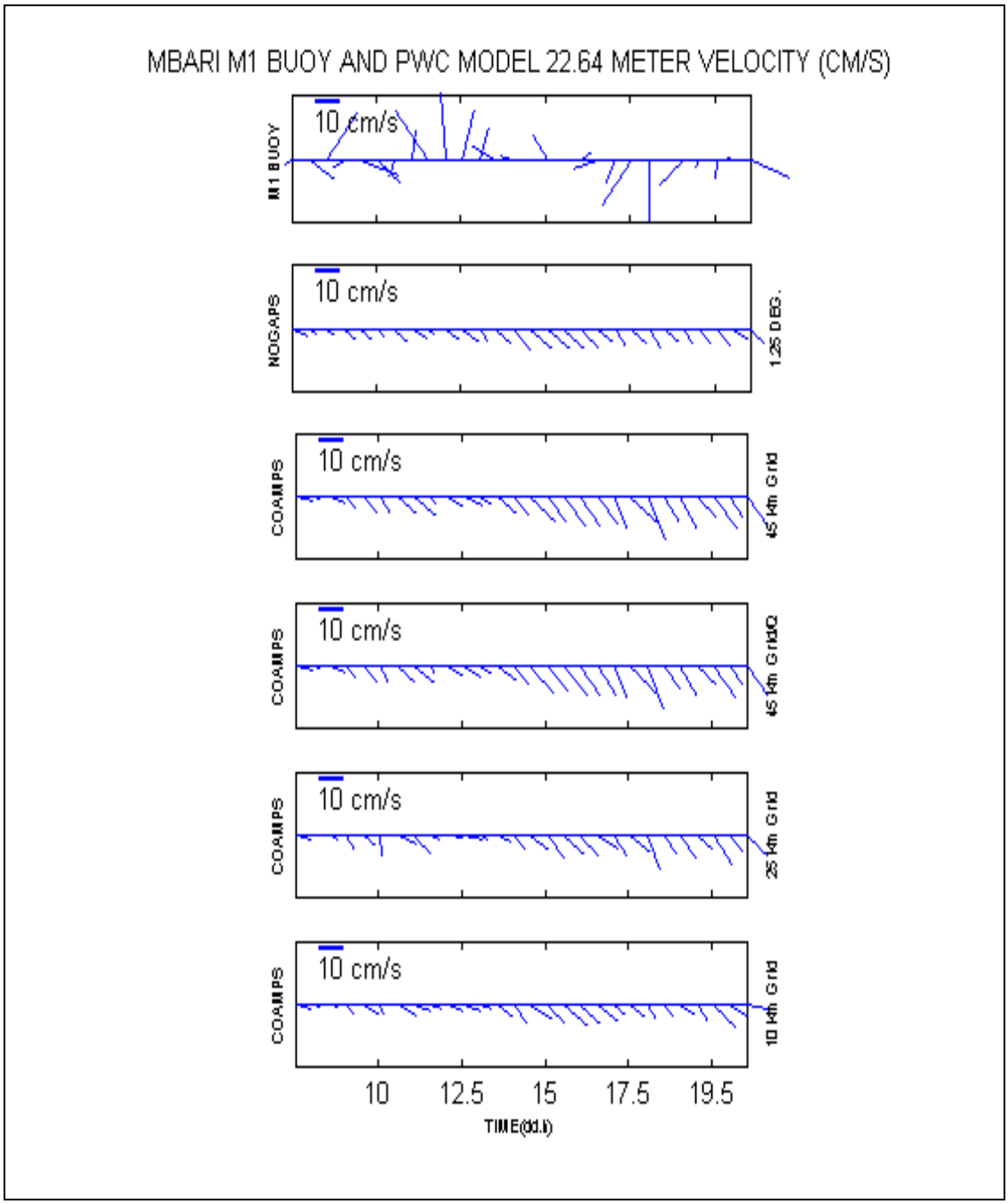

Figure 6.17. MBARI buoy M1 ADCP 22.64 m depth velocity.

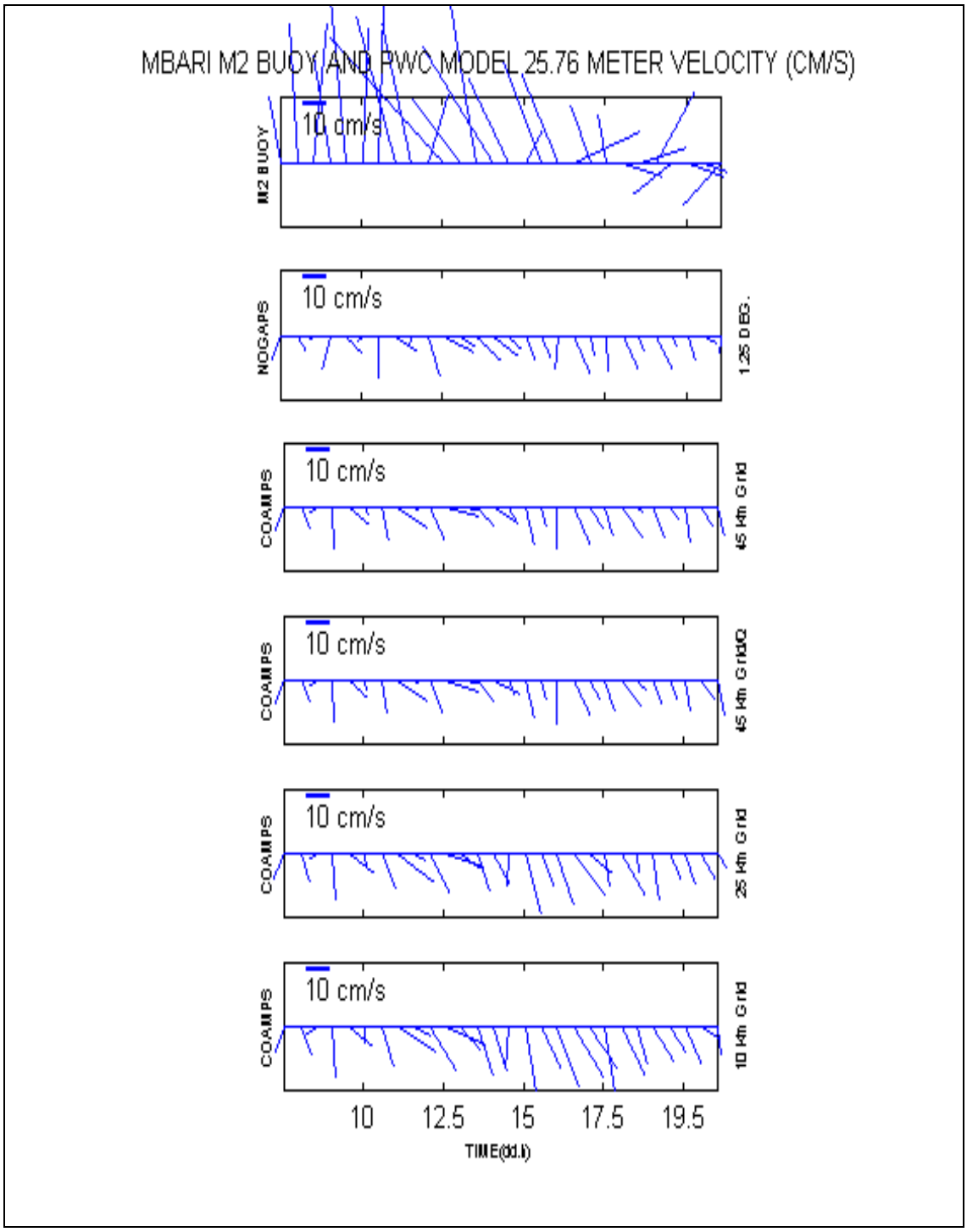

Figure 6.18. MBARI buoy M2 ADCP 25.76 m depth velocity.

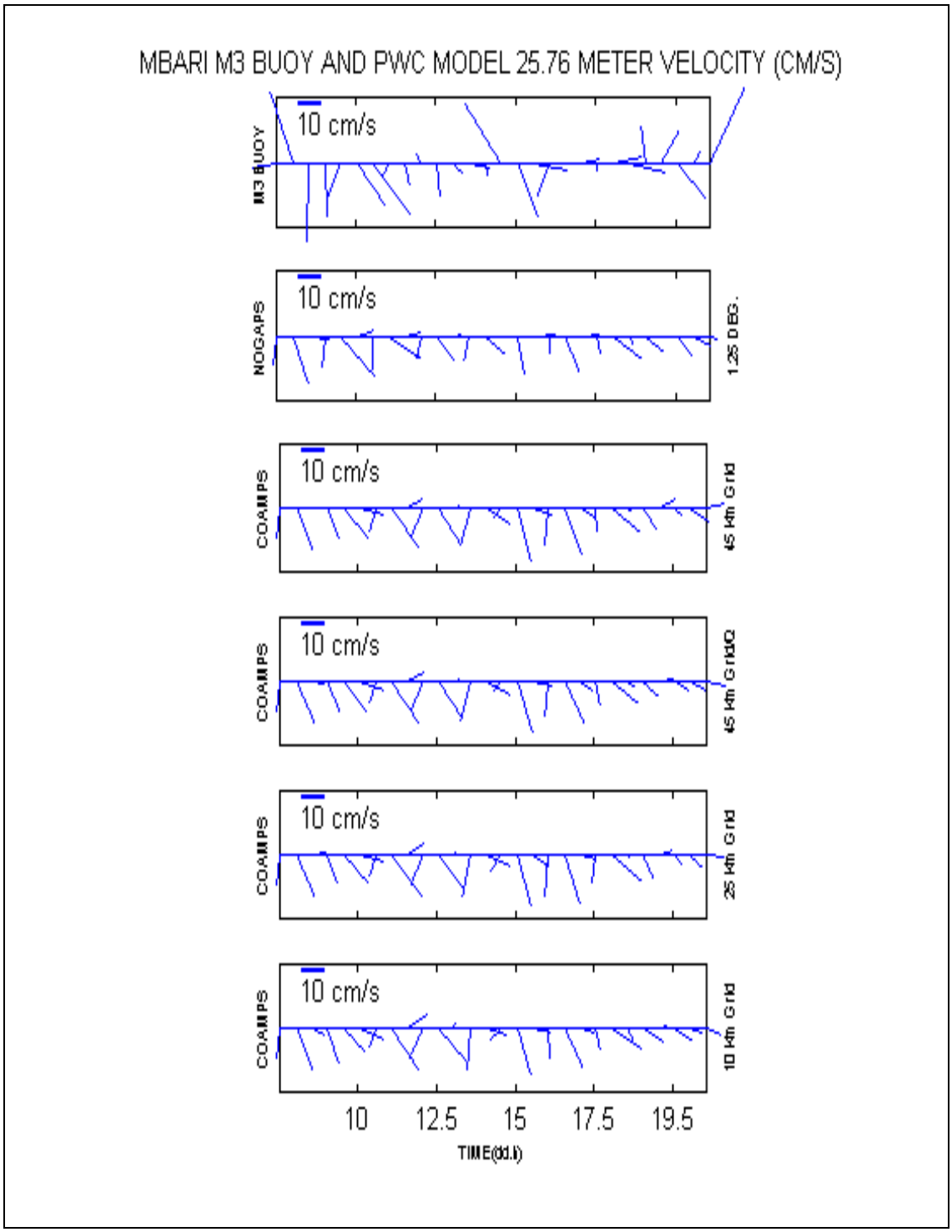

Figure 6.19. MBARI buoy M3 ADCP 25.76 m depth velocity.

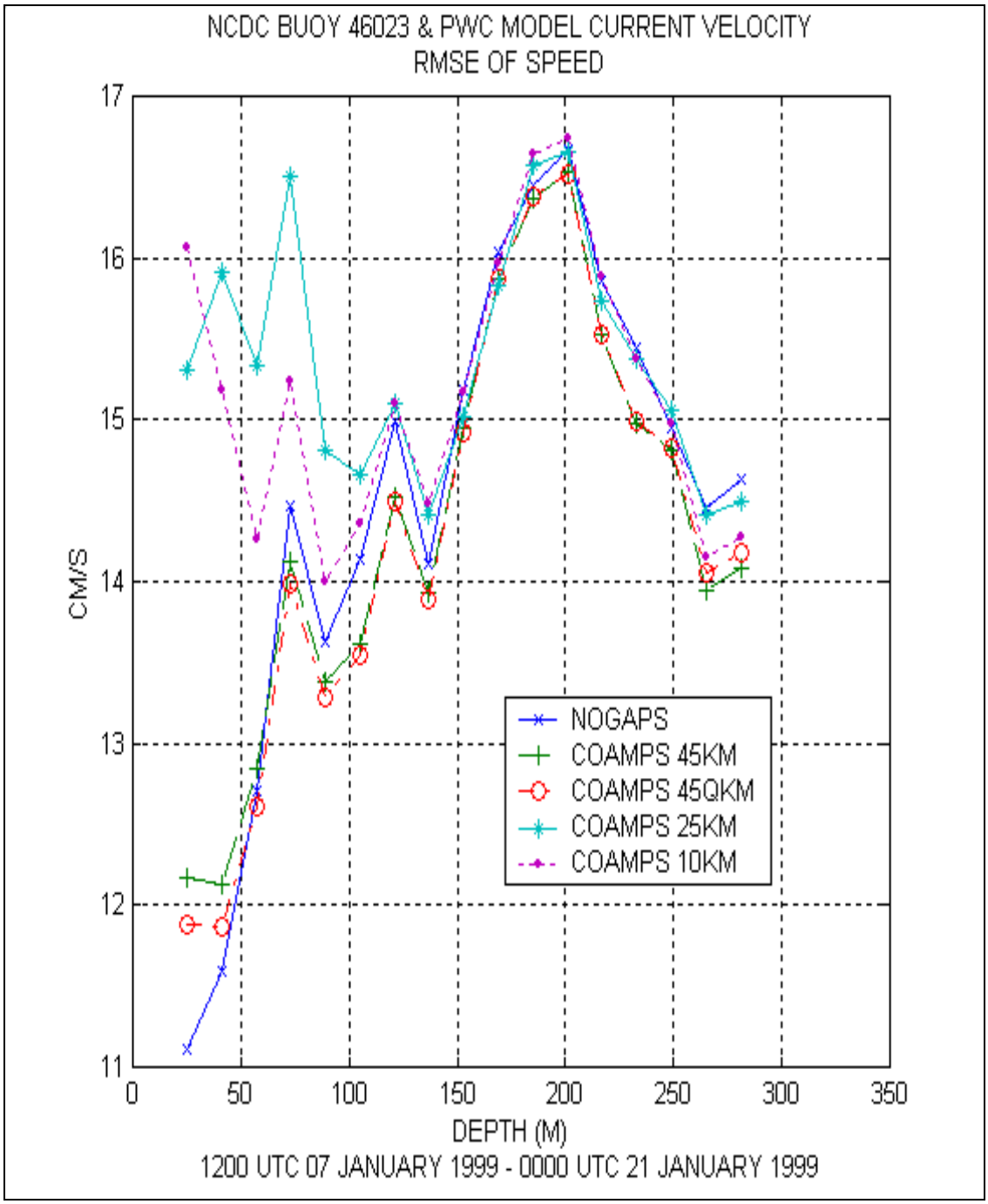

Figure 6.20. Buoy 46023 (Pt. Arguello) RMSE.

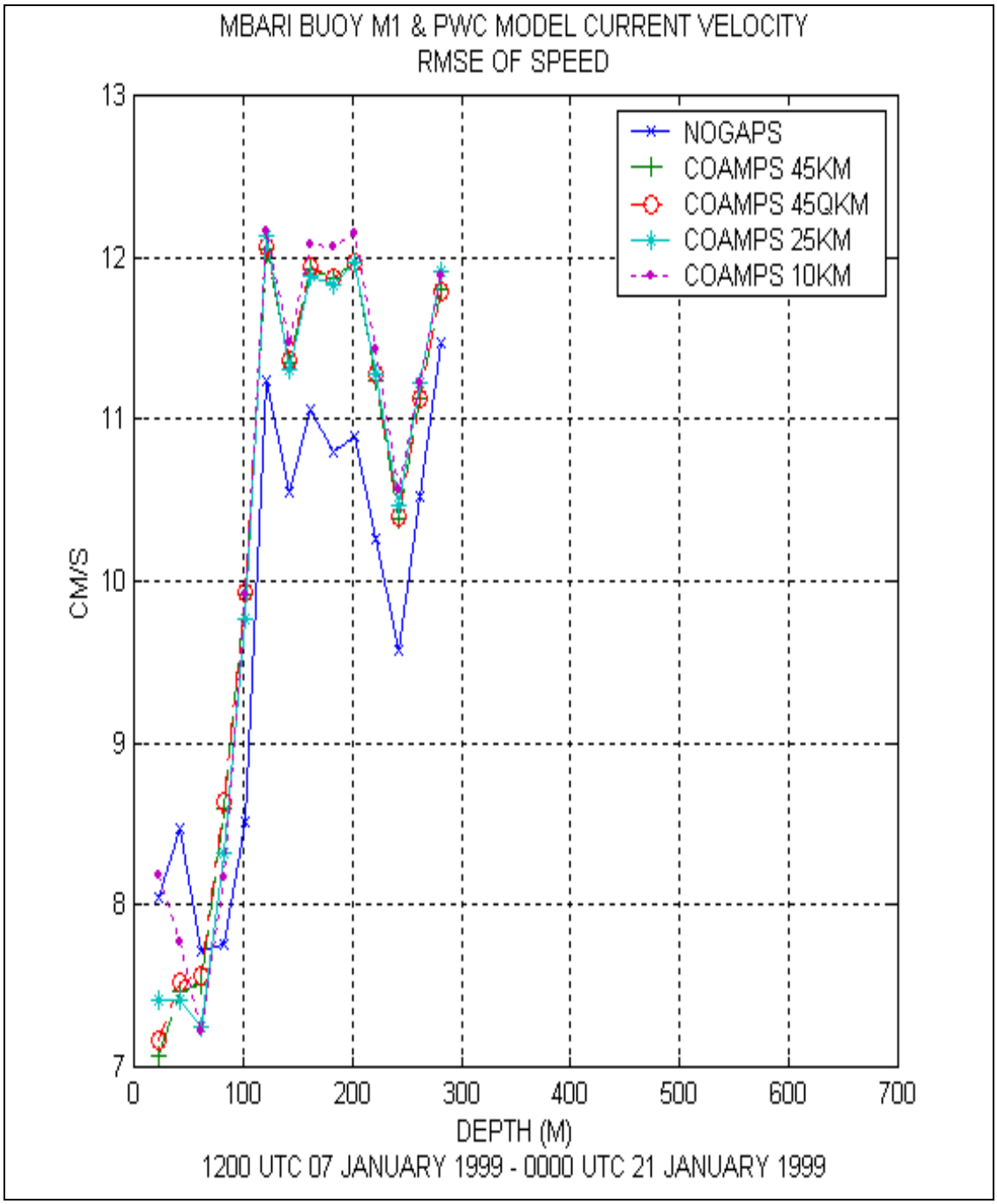

Figure 6.21. Same as Figure 6.25, except for Buoy M1.

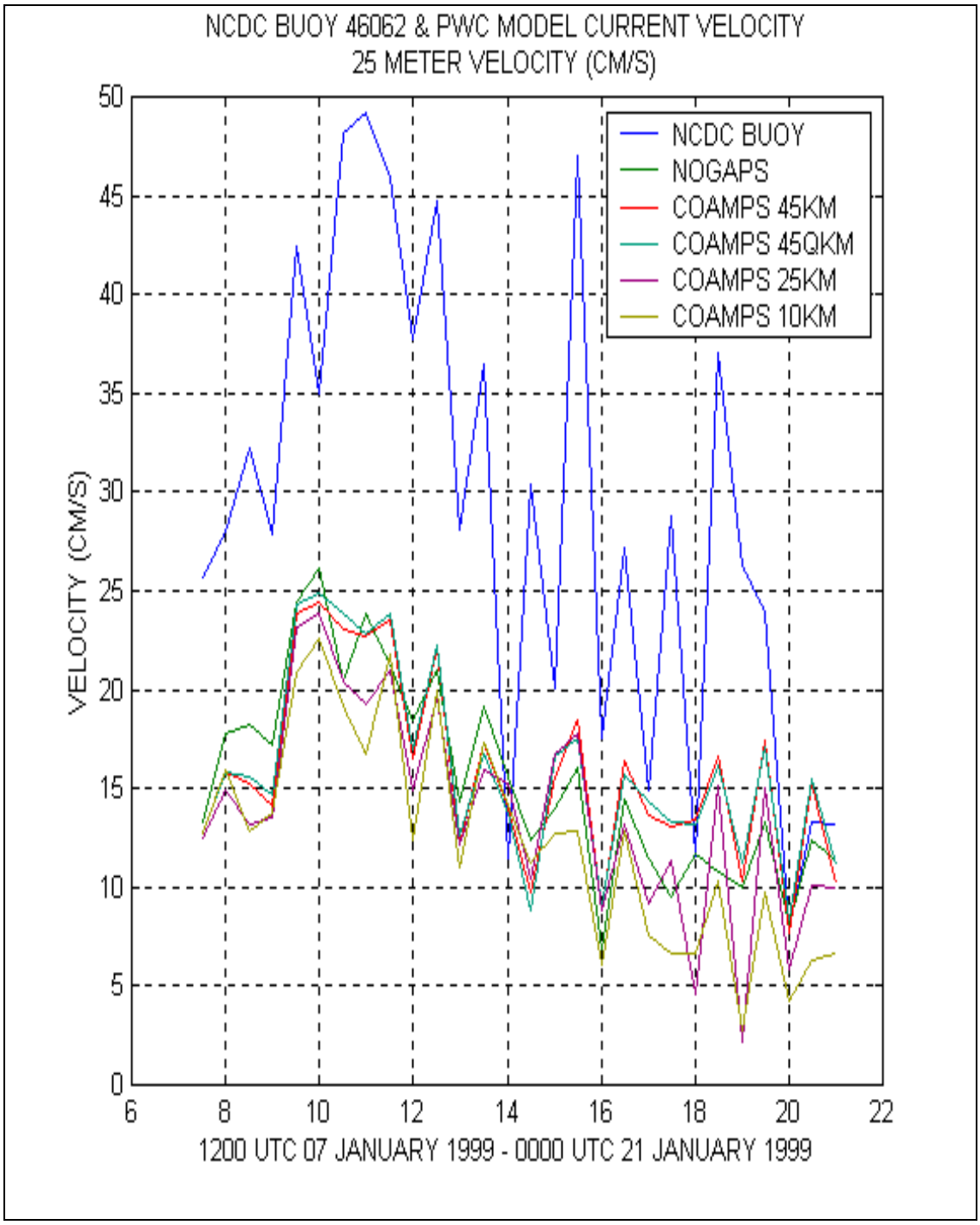

Figure 6.22. Buoy 46062 (Port San Luis) & PWC current speed.

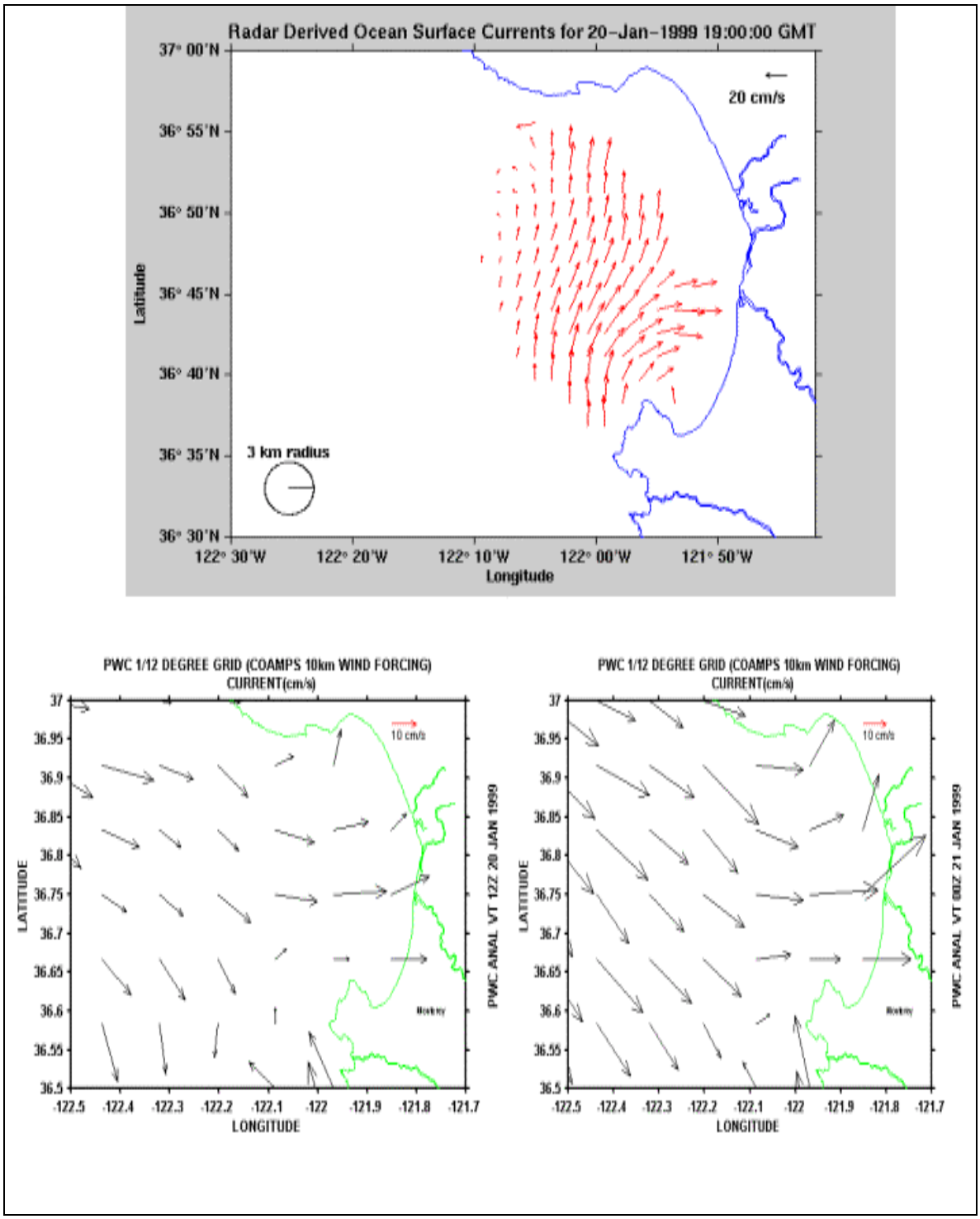

Figure 6.23. CODAR & PWC (CMP 10 km) current velocity (20 Jan 1999).

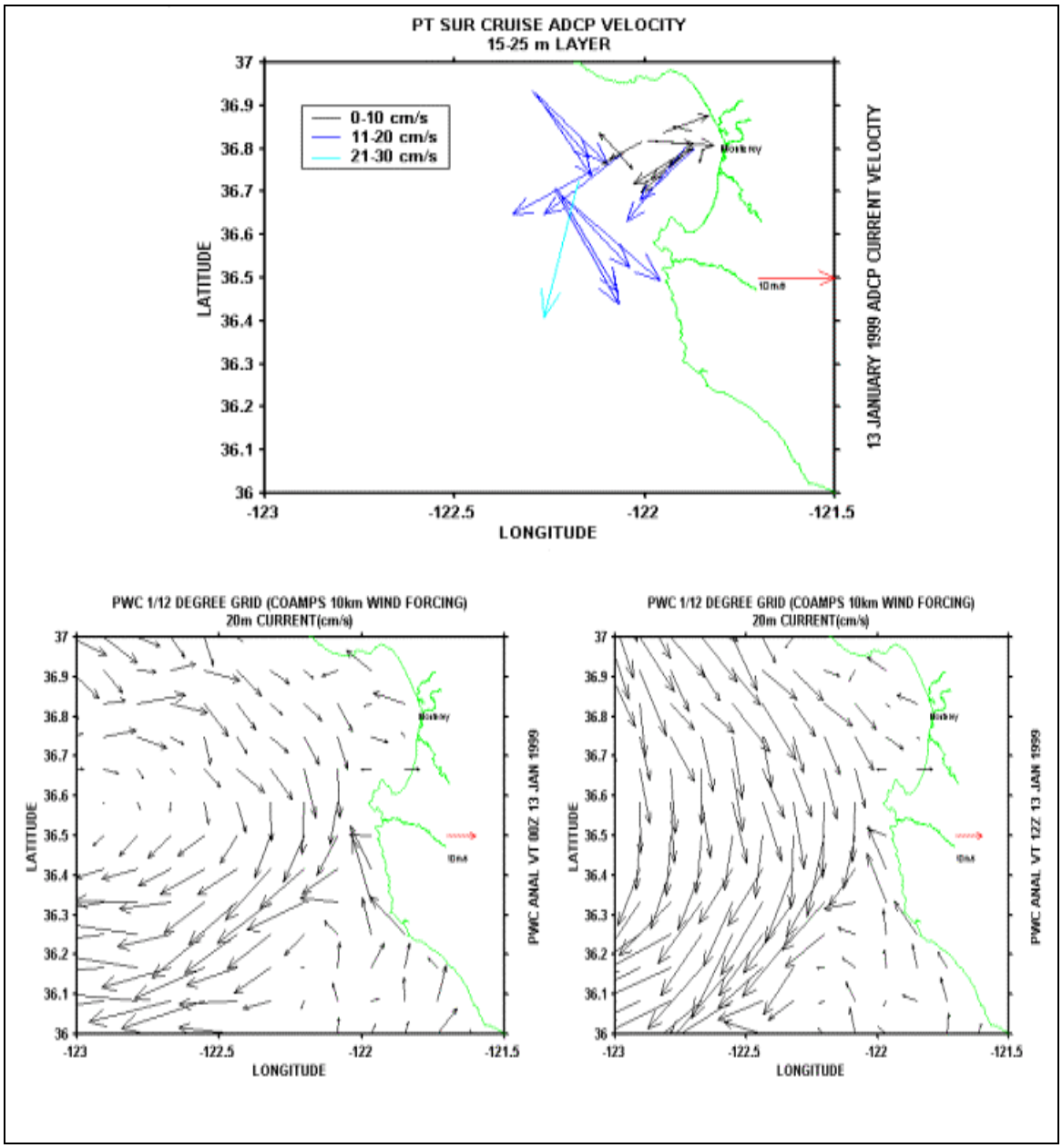

Figure 6.24. NAVO & PWC (CMP 10 km) current velocity (13 Jan 1999).

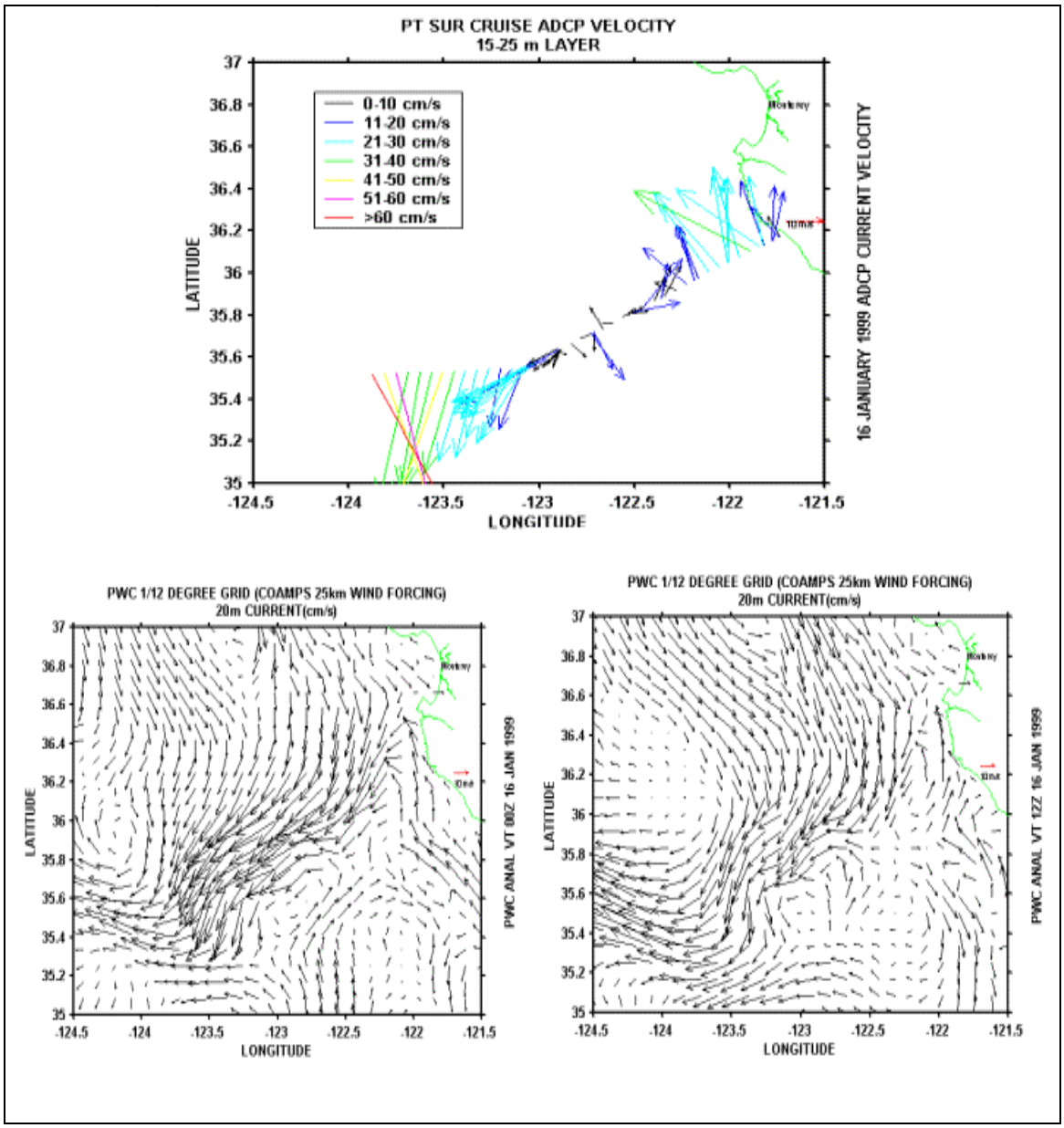

Figure 6.25. NAVO & PWC (CMP 25 km) current velocity (16 Jan 1999).

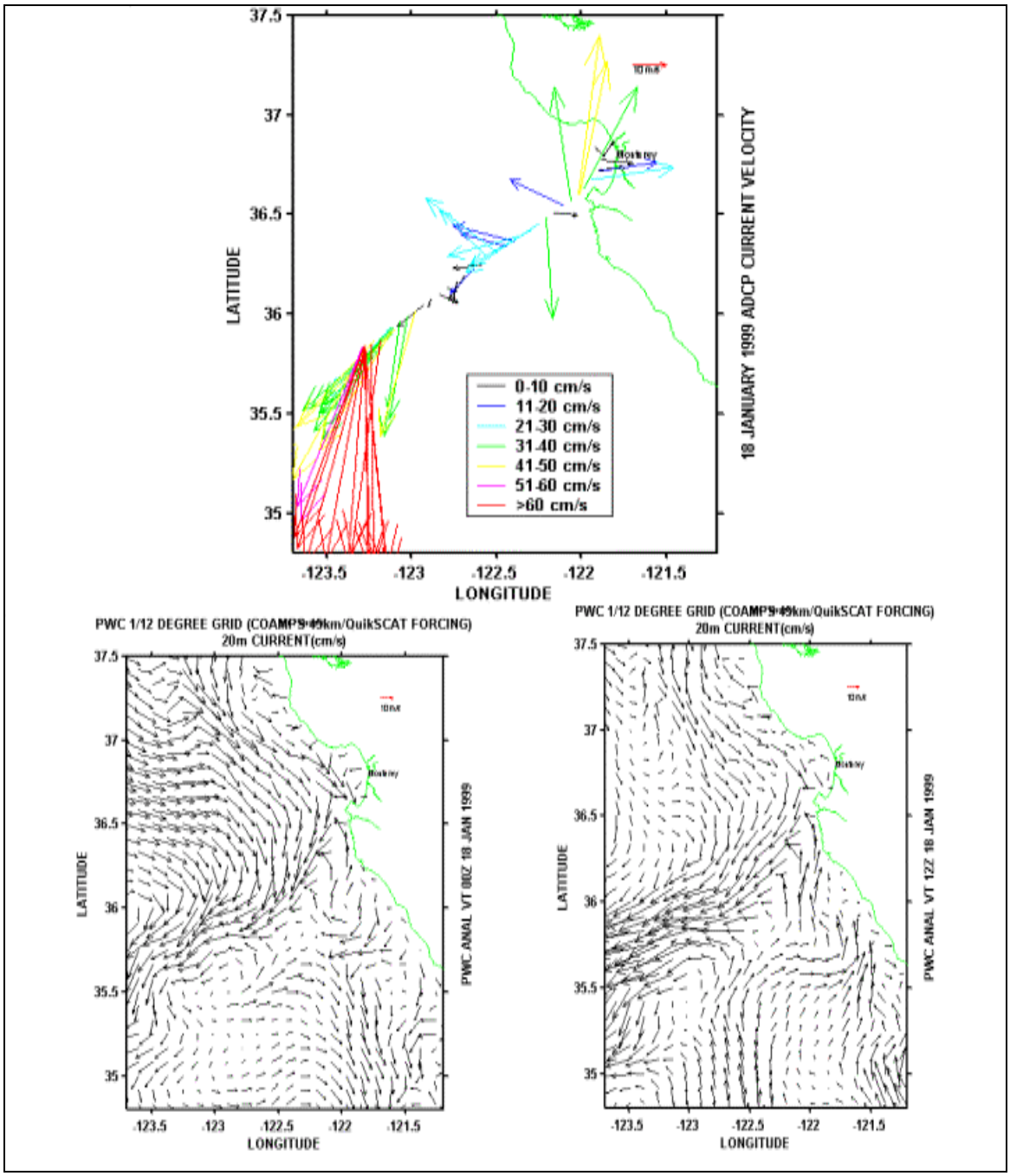

Figure 6.26. NAVO & PWC (CMP 45 km w/Q) current velocity (19 Jan 1999).

VII. CONCLUSIONS AND RECOMMENDATIONS

In a 14-day study, statistically significant differences in wind stress are found between NOGAPS and COAMPS using varying horizontal grids, and in the case of COAMPS 45 km, the insertion of synthetic QuikSCAT observations. Temporally static COAMPS 25 km wind stress fields are used to create the synthetic scatterometer data. During real QuikSCAT data acquisition, there are continuous changes in the wind field occurring during satellite transit which is a potential source of error not accounted for in the synthetic data. In addition, real satellite data contain many types of error including biases, correlated errors and gross errors due to transmission. Thus, the synthetic scatterometer data represents an idealized data set and may not reflect the actual operational impact of scatterometer data assimilation into a COAMPS 45 km model.

These atmospheric models produce statistically significant differences in the PWC ocean model with a fixed horizontal grid. In the ocean model, significant statistical differences are only detected in the surface current. No statistically significant differences are found between SSH, SST and salinity fields. As in previous studies, there is significant improvement (evaluated subjectively) with increasing atmospheric model resolution in producing realistic structures (e.g., expansion fans, ocean eddies) in coastal areas with variable topography.

Generally, the COAMPS predictions provide more structure, especially in the atmosphere, compared to NOGAPS and other COAMPS runs with increasing horizontal grid resolution. Quantitatively, the COAMPS wind stress and wind stress curl values are in agreement with previous research conducted with aircraft. Atmospheric model wind stress comparisons to buoy data show good agreement and a tendency for NOGAPS and COAMPS to underestimate and overestimate wind stress amplitude. The insertion of synthetic QuikSCAT data into the COAMPS 45 km grid produces a statistical difference but no significant operational difference in wind stress, wind stress curl and ocean current. This result implies that higher spatial and/or temporal resolution (i.e., multiple QuikSCAT satellites with improved sensors) is required for the satellites to have a

significant impact, or that the atmospheric model has sufficient skill in coastal areas using currently (i.e., DMSP SSM/I, etc) available observations.

The ocean model predictions have the expected climatological features and variability. The higher wind stress in COAMPS is translated to the ocean model in the form of higher velocity currents, closed circulations, higher EKE and better defined structure in vorticity. Comparisons to NAVOCEANO observations indicate that ocean variability increases with increasing atmospheric model horizontal resolution. In comparisons of model current to ADCP buoys, the model current amplitude is usually underestimated. This can result from model damping of the inertia waves or coarse spatial and temporal resolution of the wind stress.

The ocean model current direction reflected the variability of CalCOFI data and increased with increasing atmospheric model resolution. The model currents show improved agreement with CODAR observations with higher resolution COAMPS runs, however, the three-hourly wind input and 12-hourly ocean model output is not adequate to compare to the high spatial and temporal resolution of CODAR.

In comparison to buoy data, the direction of the model currents often followed the offshore flow, sometimes in opposition to the observed direction but is generally in agreement in phase. The impact of detiding buoy data was negligible (~ 5 cm/s). Thus, the offshore ocean features (e.g., California/Davidson Currents) in the model may mask the variability attributed to local wind forcing, bottom topography, baroclinic tides, transient coastal waves, and nonhydrostatic model physics. In particular, some differences between in the model results and NDBC buoys (46023, 46054, 46062) may be attributed to bottom topography and PWC hydrostatic model physics. The hydrostatic primitive equations neglect the horizontal coriolis terms and time which denies them a full angular momentum principle and ability to obtain the vertical velocity prognostically. The key factor determining whether the horizontal coriolis terms are important is the stratification, which can suppress vertical motion. Futhermore, the buoy depths (~400 m) are within the 300-500 m depth of the CUC/DC and CC, which implies that the vertical velocity may be non-negligible due to the 10-60 cm/s horizontal currents moving along steep bottom topography. Thus, the combination of wintertime weak stratification (i.e.,

deep mixed layers) and bottom topography (shallow buoy depths) brings into question the appropriateness of the HPEs in predicting buoy conditions (Marshall et al., 1997).

The hydrostatic primitive equations used in models such the PWC begin to break down somewhere between 10 and 1 km, as the horizontal scale of the motion becomes comparable with its vertical scale (Marshall et al., 1997). Pullen (2000), used a nested (3km and 1 km) version of the PWC and NOGAPS wind forcing in the vicinity of the Oregon coast (winter 1996-1997). The 3 km model outperformed the 9 km model with good agreement between the amplitude and time variability of the nested model currents and observations. Lewis et al. (1998) and Shulman et al. (1999) used similar nested ocean models in Monterey Bay. The model used by Shulman et al. (1999) showed greater ocean variability with higher atmospheric model horizontal resolution but was not verified by observations. The model-predicted surface currents of Lewis et al. (1998) with Doppler assimilation successfully modified the current to better match the pattern of the Doppler currents. However, as in this study, their ocean model under-predicted the Doppler current magnitudes.

The modeling of ocean currents is critical to Navy ASW, SAR and Special Warfare and Mine Warfare operations. A Navy goal is to rapidly assimilate and analyze oceanographic data to create a 4-dimensional characterization of the ocean environment at the highest possible resolution. However, unlike the atmosphere, there is no comparable network of observations. Observations on currents remain the least available. Ocean buoys, HF radar and tidal gauges are usually not available in wartime theaters of operations. It is traditional to use density measurements and geostrophic approximation to infer the current in the water column. However, in the shallow, wind-driven coastal regions "geostrophy" is difficult to apply and the limititation of microwave sensors near the coast precludes the acquisition of altimetry observations. Finally, wartime Navy operations will require data within hours rather than days or weeks.

The results of this study and others appear to point to the fact that the "one size fits all" approach, in which all regions are run with the same resolution, may not be a good use of computer resources and the demonstrable benefits of increasing resolution may vary spatially and temporally. Similarly, fast moving storm systems and their

associated winds cannot be sampled properly in both space and time. No comparison is made between COAMPS/NOGAPS wind forcasts and buoy observations to see that frontal propagaton in the models agree with reality. However, because this inertial time scale is approximately equal to the PWC 12-hour output, a systematic bias in frontal propagation speed of 12-24 hours may cause phase differences between buoy and model observations. In this study, an additional time error may result from the 3-6 hour requirement for the dynamic adjustment of the wind stress in COAMPS. For example, Table 2.2 shows that the 3-hour forecast is also used for the analysis which may introduce forecast errors as a result of the 3-hour lag in wind stress. Furthermore, this study is conducted in the winter season. However, a summer land-sea breeze system would be a challenge for future research.

Multi-day composite ocean winds derived from satellites are not optimal for use in driving a high-resolution coastal ocean model that requires data output on at time scale of hours. Thus, the Navy should continue its current approach of developing relocatable, nested, high-resolution atmospheric and ocean models. These should include development of multiple scatterometer satellite platforms with emphasis on the development of microwave sensors capable of 1-10 km resolution, and non-hydrostatic ocean models (Marshall et al., 1997) to complement the non-hydrostatic atmospheric models such as COAMPS. Finally, further sensitivity studies are needed using real scatterometer data, coupled air-ocean models, land masking interpolation, variable atmosphere and ocean model horizontal resolutions, assimilation of tides, and variable diffusion to determine the optimal use of Navy resources.

APPENDIX A. SUPPLEMENTAL GRAPHICS & TABLES

Table A.1 NDBC buoy locations, depths, and distances to model gridpoints.

						Distance to Buoy (km) Before Interpolation				
Buoy ID	**Location**	**Depth(m)**	**Land (km)**	**Buoy lon**	**Buoy lat**	**NOGAPS**	**CMP 45**	**CMP 25**	**CMP 10**	**PWC**
46005	Washington	2779.8	217.4	-131.02	46.06	27.6	7.1	7.1	N/A	N/A
46006	SE Papa	4023.4	414	-137.49	40.84	45.5	24.3	12.7	N/A	N/A
46011	Santa Maria, CA	185.9	14.5	-120.87	34.88	37.2	11.6	6.9	4.2	5.7
46012	Santa Cruz, CA	87.8	16.6	-122.73	37.39	23.8	18.7	6.5	4.6	5.9
46013	Bodega, CA	122.5	33.1	-123.33	38.23	68.4	12.4	13.4	2	4.5
46014	Pt Arena, CA	264.9	13.1	-123.97	39.23	56.6	8.6	13.9	4.7	2.4
46022	Eel River, CA	274.3	11.7	-124.51	40.74	70.2	11.6	11.5	0.1	3.3
46023*	Pt Arguello, CA	384.1	11.7	-120.97	34.71	41.2	20.6	15.8	5.2	6.8
46025	Catalina Ridge, CA	859.5	22.8	-119.08	33.75	30.6	16.2	14.5	1.5	3.8
46026	San Francisco, CA	52.1	12.4	-122.83	37.76	41	16.1	15.42	4.3	3.8
46027	St George	47.9	5.5	-124.38	41.85	84.2	20.7	0.7	0.7	4.5
46028	Cape San Martin, CA	1111.9	38	-121.89	35.74	79	8.1	6.3	6.3	3.7
46029	Columbia River, OR	128	53.8	-124.5	46.12	41.2	19.3	15.2	3.5	5.5
46050	Stonewall Bank	130.1	13.8	-124.53	44.62	56.3	9.7	11.8	5.2	4.3
46053	Santa Barbara E, CA	417	8.3	-119.85	34.24	56.1	25.4	14.3	4.6	1.4
46054*	Santa Barbara W, CA	447	26.2	-120.45	34.27	71	20.9	15.5	1.2	2.3
46059	California	4599.9	246.3	-129.996	37.98	53.3	29.9	5.3	78.6	5.6
46062*	Pt San Luis, CA	378.9	12.4	-121.01	35.1	24.5	18.2	6.7	4.718	2.7
46063	Pt Conception, CA	598	34.5	-120.66	34.25	77.7	21	14	4.3	1.8
CARO3	Cape Arago, OR	land	land	-124.37	43.33	68.6	4.6	8.9	1.7	4.7
PTGC1	Pt Arguello, CA	land	land	-120.65	34.58	72.1	16	9.3	2.8	2.8
DESW1	Destruction IS, WA	land	land	-124.48	47.67	43.4	16.9	12.9	5.4	3.8
NWPO3	Newport, OR	land	land	-124.07	44.62	49.3	19.8	4.9	3	4.1
PTAC1	Pt Arena	land	land	-123.73	38.95	22.3	28.9	14.5	4.2	3.7
TTIW1	Tatoosh IS	land	land	-124.73	48.38	45.8	20	6	1.1	5.6
M1	Monterey, CA	1600	17.3	-122.02	36.74	6.9	1.7	9.8	2.4	4.7
M2	Monterey, CA	1800	34.5	-122.4	36.67	4.7	3.3	7.4	4.6	3.4
M3	Monterey, CA	3000	39.3	-122.97	36.57	5.5	9.9	6.2	3	5.1

* ADCP buoy

Table A.2. ADCP buoy depth levels (meters).

M1	M2	M3	NDBC	PT Sur
22.64	5.76	5.76	25	20
42.64	9.76	9.76	41	37.5
62.64	13.76	13.76	57	62.5
82.64	17.76	17.76	73	87.5
102.64	21.76	21.76	89	112.5
122.64	25.76	25.76	105	137.5
142.64	29.76	29.76	121	162.5
162.64	33.76	33.76	137	187.5
182.64	37.76	37.76	153	187.5
202.64	41.76	41.76	169	212.5
222.64	45.76	45.76	185	237.5
242.64	49.76	49.76	201	262.5
262.64	53.76	53.76	217	287.5
282.64	57.76	57.76	233	312.5
302.64	61.76	61.76	249	337.5
322.64	65.76	65.76	265	362.5
342.64	69.76	69.76	281	387.5
362.64	73.76	73.76	297	412.5
382.64	77.76	77.76	313	
402.64	81.76	81.76	329	
422.64	85.76	85.76		
442.64	89.76	89.76		
462.64	93.76	93.76		
482.64	97.76	97.76		
502.64	101.76	101.76		
522.64	105.76	105.76		
542.64	109.76	109.76		
562.64	113.76	113.76		
582.64	117.76	117.76		
602.64	121.76	121.76		

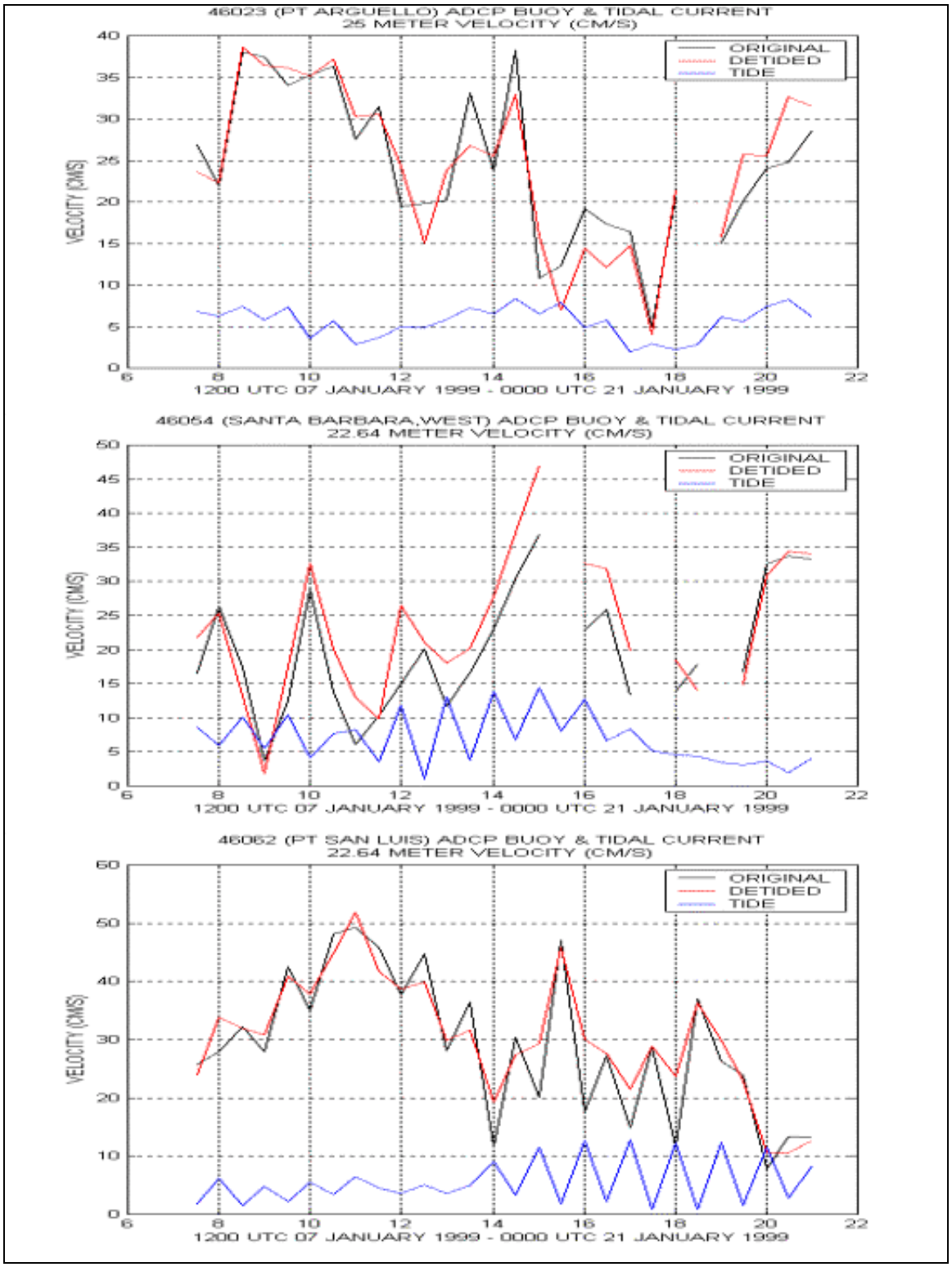

Figure A.1. NDBC buoy and tidal currents.

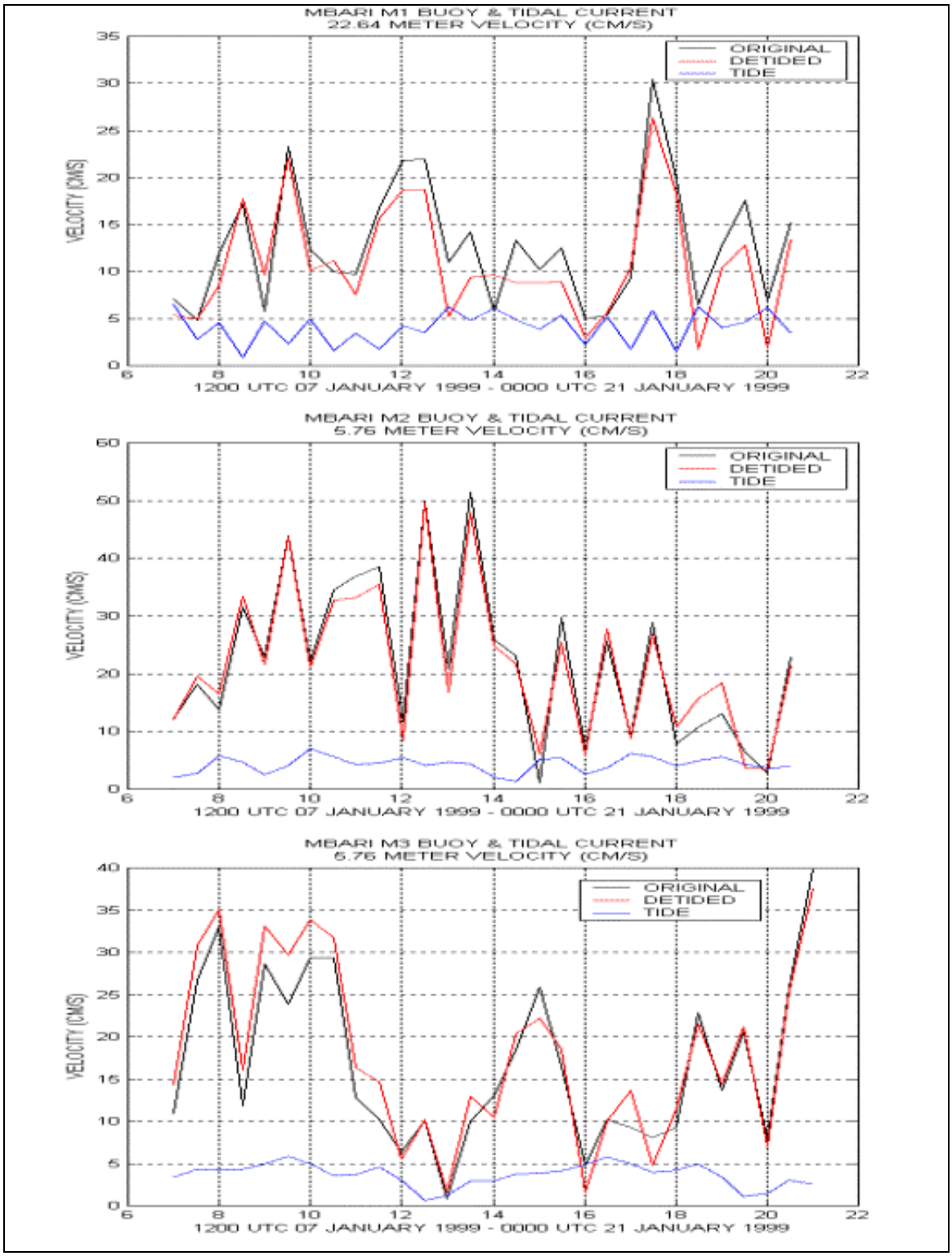

Figure A.2. MBARI buoy and tidal currents.

LIST OF REFERENCES

Aikman, F. III, G. L. Mellow, T. Ezer, D. Sheinin, P. Chen, L. Breaker, K. Bosley, and D. F. Rao, 1995: Toward An Operational Nowcast/Forecast System For The U.S. East Coast. Chapter 6.2 In *Modern Approached To Data Assimilation In Ocean Modeling*. P. Malanotte-Rizzoli, editor. Elseveir Science Publishers, Elseveir Oceanography Series, David Halpern, editor, 38 pp.

Allen, J.S., 1980: Models of Wind-driven Currents On The Continental Shelf. *Ann. Rev. Fluid Mech*., **12**, 389-433.

Allen, J.S., P.A. Newberger and J. Federiuk, 1995: Upwelling Circulation On The Oregon Continental Shelf. I. Response to Idealized Forcing. *J. Phys. Oceanogr*., **25**, 1843-1866.

Allard, R., P. Farrar, D. Mark, J. Martin, B. Shapiro, S. Lowe, and D.S. Ko, 1996: Creating a 4-D Integrated Scenario Near Camp Pendleton, CA. *Proceedings of The American Meteorological Society Conference On Coastal Oceanic and Atmospheric Prediction*, Atlanta, GA, 28 January through 2 February 1996, pp. 15-21.

Arthur, R.S., 1965: On The Calculation of Vertical Motion In Eastern Boundary Current From Determinations of Horizontal Motion. *J. Geophys. Res*., **70**(12), 2799-2803.

Banta, R.M., L.D. Oliver, and D.H. Levinson, 1993: Evolution of The Monterey Bay Sea-breeze Layer As Observed By Pulsed Doppler Lidar. *J. Atmos. Sci*., **50**(29), 3959-3982,

Baker, N.L., 1992: Quality Control For The Navy Operational Atmospheric Database. *Wea. Forecasting*, **7**, 250-261.

Bakun, A. and C.S. Nelson, 1991: The Seasonal Cycle of Wind Stress Curl In Subtropical Eastern Boundary Current Regions. *J. Phys. Oceanogr.*, **21**, 1815-1834.

Barker, E.H., 1992: Design of The Navy's Multivariate Optimum Interpolation Analysis System. *Wea. Forecasting*, **7**, 220-331.

Barnier, B., M. Boukthir and J. Verron, 1991: Use of Satellite Scatterometer Winds To Force An Ocean General Circulation, Model. *J. Geophys. Res.*, **96**, 22025-22042.

Barnier, B., J. Capella, and J.J. O'Brien, 1994: The Use of Satellite Scatterometer Winds To Drive A Primitive Equation Model of The Indian Ocean: The Impact of Bandlike Sampling. *J. Geophys. Res.*, **99**, 14187-14196.

Batteen, M. L., 1997: Wind-forced Modeling Studies of Currents, Meanders, And Eddies In The California Current System. *J. Geophys. Res.*, **102**, 985-1010.

Batteen, M. L., C. A. Collins, C.R. Gunderson and C.S. Nelson, 1995: The Effect of Salinity On Density In The California Current System. *J. Geophys. Res.*, **100**, 8733-8749.

Blencoe, D.G., 2001: Impact of High Resolution Wind Fields On Coastal Ocean Models. M.S. Thesis, Naval Postgraduate School, Monterey, California, September 2001.

Blumberg, A.F., and G.L. Mellor, 1987: A Description of A Three-dimensional Coastal Circulation Model. *Three-Dimensional Coastal Circulation Models*, N. Heaps, editor, American Geophysical Union, Washington, DC, 208 pp.

Boutin, J., J. Etcheto, M. Rafizaden, and D. C.E. Bakker, 1999: Comparison of NSCAT, ERS-2 Active Microwave Instrument, Special Sensor Microwave Imager, and Carbon Interface Ocean Atmosphere Buoy Wind Speed: Consequences For The Air-sea Carbon Dioxide Exchange Coefficient. *J. Geophys. Res.*, **104**, 11375-11392.

Boutin, J., Siefridt, J. Etcheto and B. Barnier, 1996: Comparison of ECMWF And Satellite Ocean Wind Speeds From 1985 To 1992. *Int. J. Remote Sensing*, **17**, 2897-2913.

Bowditch, Nathaniel, 1995: The American Practical Navigator. Defense Mapping Agency Hydrographic/Topographic Center, Bethesda, Maryland, 873 pp.

Breaker, L. C., and W. W. Broenkow, 1994: The Circulation of Monterey Bay and Related Processes. A.D. Ansell, R.N. Gibson, and M. Barnes (eds). *Oceanography and Marine Biology*: *An Annual Review (Vol. 32)*. London: UCL Press Limited.

Brink, K.H., J.H. La Case and J.D. Irish, 1994: The Effect of Short-scale Wind Variations On Shelf Currents. *J. Geophys. Res*., **91**(C1), 1783-1797.

Burnett, W., J. Harding and G. Heburn, 2002: Overview of Operational Ocean Forecasting In The U.S. Navy: Past, Present & Future. *Oceanography*, **15**(1), 4-12.

Busalacchi, A.J., R.M. Atlas, and E.C. Hackert, 1993: Comparison of Special Microwave Imager Vector Wind Stress With Model-derived and Subjective Products For The Tropical Pacific. *J. Geophys. Res*., **98**, 6961-6977.

Chapman, D.C., 1987: Application of Wind-Forced, Long, Coastal-Trapped Wave Theory Along The California Coast. *J. Geophys. Res*., **92**, 1798-1816.

Chen, D., W.T. Liu, S.E. Zebiak, M.A. Cane, Y. Kushnir and D. Witter, 1999a: Sensitivity of The Tropical Pacific Ocean Simulation To Temporal and Spatial Resolution of Wind Forcing. *J. Geophys. Res*., **104**, 11261-11271.

Chen, D., M.A. Cane, and S.E. Zebiak, 1999b: The Impact of NSCAT Winds On Predicting The 1997/1998 El Nino: A Case Study With The Lamont-Doherty Earth Observatory Model. *J. Geophys. Res*., **104**, 11321-11327.

Chin, T.M., R.F. Milliff, and W.G. Large, 1998: Basin-scale, High-wavenumber Sea Surface Wind Fields From A Multi-resolution Analysis of Scatterometer Data. *J. Atm. Ocean. Tech*., **15**, 741-763.

Chu, P.C., Y. Chen and S. Lu, 1998: Wind-driven South China Sea Deep Basin Warm-core/Cool-core Eddies. *J. Oceanography*, **54**, 347-360.

Chu, P.C., and S.K. Wells, 1997: Temporal and Spatial Scales of The Yellow Sea Thermal Variability. *J. Geophys. Res*., **102**, 5655-5667.

Clancy, R.M., P.W., Dewitt, P. May and D. S. Ko, 1996: Implementation of A Coastal Ocean Circulation Model For The West Coast of The United States. *Proceedings of the American Meteorological society Conference on Coastal Oceanic and Atmospheric Prediction*, Atlanta, GA, 28 January through 2 February 1996, pp. 72-75.

Clifford, M.,C. Horton, and J. Schmitz, 1997: An Oceanographic Nowcast/Forecast System For The Red Sea. *J. Geophys. Res*., **102**, 25101-25122.

Collins, C.A., N. Garfield, T.A. Rago, F.W. Rischmiller, E. Carter, 2000: Mean Structure of The Inshore Countercurrent and California Undercurrent Off Point Sur, California. *Deep-Sea Research II*, **47**, 765-782.

Daley, R., 1991: Atmospheric Data Analysis. Cambridge: Cambridge University Press, 451 pp.

DeRada, S., J.C. Kindle, S. Cayula, F. Bahr, F. Chaves, J. O'Brien and M. Bourassa, 2002: High Resolution Forcing For The Northwestern Pacific Ocean Model Fields. Poster presentation Ocean Sciences Meeting.

Draper, D.W. and D.G. Long, 2002: An Assessment of SeaWinds On QuikSCAT Wind Retrieval. *J. Geophys. Res*., **107**(C12), 5-1 – 5-14.

Edwards, K.A., D.P. Rogeres, and C.E. Dorman, 2002: Adjustment of The Marine Atmospheric Boundary Layer To The Large-scale Bend In The California Coast. *J. Geophys. Res*., **107**(C12), 6-1 – 6-11.

Elzer, T. and G.L. Mellor, 2000: Sensitivity Studies With The North Atlantic Sigma Coordinate Princeton Ocean Model. *Dyn. of Atm and Oceans*, **32**, 185-208.

Emery, W.J. and R.E. Thomson, 1998: Data Analysis Methods In Physical Oceanography. Oxford: Pergamon, 634 pp.

Enriquez, A.G. and C.A. Friehe, 1995: Effects of Wind Stress and Wind Stress Curl Variability On Coastal Upwelling. *J. Phys. Oceanogr*., **25**, 1651-1671.

Ezer, T and G. Mellor, 2000: Sensitivity Studies With The North Atlantic Sigma Coordinate Princeton Ocean Model. *Dynamics of Atmospheres and Oceans*, **32**,185-208.

Foster, M.D., 1993: Evolution of Diurnal Surface Winds and Surface Currents For Monterey Bay. M.S. Thesis, Naval Postgraduate School, Monterey, California, December 1993.

Frankignoul, C., and C. Duchene, 1989: A Statistical Approach To Testing Equatorial Ocean Models With Observed Data. *J. Phys. Oceanogr*., **19**, 1191- 1207.

Gan, J. and J.S. Allen, 2002: A Modeling Study of Shelf Circulation Off Northern California In The Region of The Coastal Ocean Dynamics Experiment 2. Simulations and Comparisons With Observations. *J. Geophys. Res*., **107**(C11), 5-1 – 5-21.

Garwood, R.W., 1979: Air-sea Interaction and Dynamics of The Surface Mixed Layer. *Review of Geophysics and Space Physics*, **17**(7), 1508-1524.

Garfield, N., M.E. Maltrud, C. A Collins, T.A. Rago and R.G. Paquette, 2000: Lagrangian Flow In The California Undercurrent, An Observation and Model Comparison. *J. Marine Systems*, **29**, 201-220.

Goerss, J.S., and P. Phoebus, 1992: The Navy's Operational Atmospheric Analysis. *Wea Forecasting*, **7**, 232-249.

Grima, N., a. Bentamy, K. Katsaros, and Y. Quilfen, 1999: Sensitivity of An Oceanic General Circulation Model Forced By Satellite Wind-stress Fields. *J. Geophys. Res*., **104**, 7967-7989.

Guymer, T.H. and S. Zecchetto, 1991: Winds Derived From SEASAT's Microwave Suite. *Int. J. Remote Sensing*, **12**, 1699-1712.

Haack, T., S.D. Burk, C. Dorman and D Rogers, 2001: Supercritical Flow Interaction With The Cape Blanco-Cape Mendocino Orographic Complex. *Mon. Wea. Rev*., **129**, 688-708.

Haidvogel, D.B. and A. Beckmann, 1999: Numerical Ocean Circulation Modeling. Imperial College Press. London. 318 pp.

Halpern, D., A. Hollingsworth, and F. Wentz, 1994: ECMWF and SSM/I Global Surface Wind Speeds. *J. Atm Ocean. Tech*., **11**, 779-788.

Haney, R. L, 1991: On The Pressure Gradient Force Over Steep Topography In Sigma Coordinate Ocean Models. *J. Phys. Oceanogr.,* **21**, 610-619.

Hansen, D.V. and A. Herman, 1989: Temporal Sampling Requirements For Surface Drifting Buoys In The Tropical Pacific. *J. Atmos. Ocean. Tech*., **6**(4), 599-607.

Harding, J., T. Curtin, S. Chang, R.M. Clancy, and A. Johnson, 1996: Naval coastal ocean prediction. *Proceedings of the American Meteorological Society Conference on Coastal Oceanic and Atmospheric Prediction*, Atlanta, GA, 28 January through 2 February 1996, pp. 44-51.

Harms, S. and C.D. Winant, 1998: Characteristic Patterns of The Circulation In The Santa Barbara Channel. *J. Geophys. Res*., **104**, 3041-3065.

Haus, B.K., H. C. Graber, and L.K. Shay, 1997: Synoptic Measurement of Dynamic Oceanic Features. *Oceanography*, **10**, 45-48.

Hickey, B.M., 1998. Coastal Oceanography of Western North America From The Tip of Baja California To Vancouver Island. pp 345-393. In: The Sea, Volume 12, edited by A.R. Robinson and K.H. Brink, John Wiley and Sons, Inc., NY.

Hodur, R.M., X. Hong, J.D. Doyle, J. Pullen, J.Cummings, P. Martin and M.A. Rennick, 2002: The Coupled Ocean/Atmosphere Mesoscale Prediction System (COAMPS). *Oceanography*, **15**(1), 88-98.

Hodur, R.M., 1993: Development and Testing of The Coupled Ocean/Atmosphere Mesoscale Prediction System (COAMPS). NRL/MR/7533-93-7213, Naval Research Laboratory, Monterey, CA 93943-5502, 81 pp.

Hodur, R.M., 1997: The Naval Research Laboratory's Coupled Ocean/Atmosphere Mesoscale Prediction System (COAMPS). *Mon. Wea. Rev*., **125**, 1414-1430.

Hogan, T.F. and T.E. Rosmond, 1991: The Description of The Navy Operational Global Atmospheric Predictions System's Spectral Forecast Model. *Mon. Wea. Rev*., **119**, 1786-1815.

Hinton, Perry R, 1995: Statistics Explained; A Guide For Social Science Students. New York: Routledge.

Holt, T., J. Doyle, R. Brody and R. Hodur, 1998: Simulations of Coastal Mesoscale Phenomena Using The Coupled Ocean-Atmospheric Mesoscale Prediction System (COAMPS): A Verification and Evaluation Study. *Second AMS Conference On Coastal Atmospheric and Oceanic Prediction and Processes*, Phoenix, AZ, 11-16 January 1998, pp. 100-107.

Horton, C., M. Clifford, D. Cole, J.E. Schmitz, and L.H. Kantha, 1992: Operational Modeling: Semi-enclosed Basin Modeling At The Naval Oceanographic Office. *Oceanography*, **5**, 69-72.

Horton, C., M. Clifford, J. Schmitz and L. Kantha, 1997: A Real-time Oceanographic Nowcast/Forecast System For The Mediterranean Sea. *J. Geophys. Res*., **102**, 25123-25156.

Hurlburt, H.E. and J.D. Thompson, 1980: A Numerical Study of Loop Current Intrusions and Eddy Shedding. *J. Phys. Oceanog*., **10**, 1611-1651.

Hutt, D., 2002: Ocean Models For Defense Related Initiatives. *Backscatter*, Spring/Summer 2002, 15-20.

Huyer, A., P.M. Kosro, J. Fleishbein, S.R. Ramp, T. Stanton, L. Wasburn, F. Chavez and T. Cowles, 1991: Currents and Water Masses of The Coastal Transition Zone Off Northern California, June To August 1988. *J. Geophys. Res*., **14**, 14809-14831.

Huyer, A., 1983: Coastal Upwelling In The California Current System. *Prog. Oceanogr*., **12**, 259-284.

Jones, H., and J. Marshall, 1993: Convection With Rotation In A Neutral Ocean: A Study of Open-ocean Deep Convection. *J. Phys. Oceanogr*., **23**, 1009-1039.

Kantha, L.H., and C.A. Clayson, 2000: Numerical Models of Oceans and Oceanic Processes. Volume 66 of International Geophysics Series. Academic Press. 940 pp.

Kelly, K.A., S. Dickinson and Z. Yu, 1999: NSCAT Tropical Wind Stress Maps: Implications For Improving Ccean Modeling. *J. Geophys. Res*., **104**, 11291- 11310.

Kent, E.C., P.K. Taylor and P. G. Challenor, 1998: A Comparison of Ship-and scatterometer-derived Wind Speed Data In Open Ocean and Coastal Areas. *Int. J. Remote Sensing*, **19**, 3361-3381.

Klemp, J. and R. Wilhelmson, 1978: The Simulation of Three-dimensional Convective Storm Dynamics. *J. Atmos. Sci*., **35**, 1076-1096.

Kramer, H.J., 2002: Observation of The Earth and Its Environment: Survey of Missions and Sensors (4ed). New York: Springer-Verlag, 1540 pp.

Large, W.G., W.R. Holland and J.C. Evans, 1991: Quasi-geostrophic Ocean Response To Real Wind Forcing: The Effects of Temporal Smoothing. *J. Phys. Oceanog*., **21**, 998-1017.

Large, W.G., and S. Pond, 1981: Open Ocean Momentum Flux Measurements In Moderate To Strong Winds. *J. Phys. Oceanog*., **11**,324-336.

Lee, T.F. and J.S. Boyle, 1991: A Synoptic Comparison of SSM/I Winds With Output From An Operational Forecast System. *Wea. Forecasting*, **6**, 404-410.

Legler, D.M. and J.J. O'Brien, 1985: Development and Testing of A Simple Assimilation Technique To Derive Average Wind Fields From Simulated Scatterometer Data. *Mon. Wea. Rev*., **10**, 1791-1800.

Lewis, J. K., I. Shulman, and A.F. Blumberg, 1998: Assimilation of Doppler radar Current Data Into Numerical Ocean Models. *Cont. Shelf Res*., **18**, 541-559.

Liu, W.T., 2001: Wind Over Troubled Waters. *Backscatter*, Spring/Summer 2001, 10-14.

Lorenz, E.N. 1956: Empirical Orthogonal Functions and Statistical Weather Prediction. Sci. Rep., 1, 49 pp., Stat. Forecasting Proj., Dep. of Meteorol., Mass. Inst. of Technol., Cambridge.

Lynn, R.J., and J.J. Simpson, 1987: The California Vurrent Dystem: The Seasonal Variability of Its Physical Characteristics. *J. Geophys. Res*., **92**(C12), 12947-12966.

Marshall. J., C. Hill, L. Perelman, and A. Adcroft, 1997: Hydrostatic, Quasi-hydrostatic, and Nonhydrostatic Ocean Modeling. *J. Geophys. Res*., **102** (C3), 5733-5752.

Mass, C.F, D. Owens, K.Westrick and B.A. Colle, 2002: Does Increasing Horizontal Resolution Produce More Skillful Forecasts? The Results of Two Years of Real-time Numerical Weather Prediction Over The Pacific Northwest. *Bull. Amer. Meteor. Soc.*, **83**, 407-430.

Mellor, G. L., and T. Yamada, 1982: Development of A Turbulent Closure Model For Geophysical Fluid Problems. *Rev. Geophys*., **20**, 851-875.

Mellor, G.L., 1996: Users Guide For A Three-dimensional Primitive Equation Numerical Ocean Model. Atmospheric and Oceanic Science Program, Princeton University, Princeton, N.J., 53 pp.

Metzger, J.E., O.M. Smedstad, H.E. Hurlburt, A.J. Wallcraft and R.C. Rhodes, 2001: Nowcasting & Forecasting The Global Ocean. *Backscatter*, Winter 2001, 25-30.

Milliff, R.F., W.G. Large, W.R. Holland, and J.C. McWilliams, 1996: The General Circulation Responses of High-resolution North Atlantic Ocean Models To Synthetic Scatterometer Winds. *J. Phys. Oceanog*., **26**, 1747-1768.

Milliff, R.F., W.G. Large, J. Morzel and G. Danabasoglu, 1999: Ocean General Circulation Model Sensitivity To Forcing From Scatterometer Winds. *J. Geophys. Res*., **104**, 11337-11358.

Neal, T.C., 1992: Analysis of Monterey Bay CODAR-derived Surface Currents. M.S. Thesis, Naval Postgraduate School, Monterey, California, September 1992.

Nelson, C.S., 1977: Wind Stress and Wind Stress Curl Over The California Current. NOAA Tech. Rep. NMFS SSRF-714, 87 pp., Natl. Oceanic and Atmos. Admin., Silver Spring, MD.

Nihoul, J.C. J., P.T Strub and P.E. LaViolette, 1998: Remote Sensing. In: The Sea: The Global Coastal Ocean Processes and Methods, K.H. Brink and A.R. Robinson (Eds). New York: John Wiley & Sons, Inc., pp. 329-357.

Nuss, W.A., D.D.E. Long, P.E. Mantey, A. Pang, E.C. Rosen and J. Paduan, 1998: The Real-time Environmental Information Network and Analysis System (REINAS*). Naval Research Reviews, Office of Naval Research*, **L** (2), 24-30.

Nuss, W.A., and D. Titley, 1994: Use of Multiquadratic Interpolation For Meteorological Objective Analysis. *Mon. Wea. Rev*.,**122**,1611-1631.

Paduan, J.D., and M.S. Cook, 1997: Mapping Surface Currents in Monterey Bay With CODAR-type HF radar. *Oceanography*, **10**, 49-52.

Paduan, J.D., and L.K. Rosenfeld, 1996: Remotely Sensed Surface Currents In Monterey Bay From Shore-Based HF Radar (CODAR). *J. Geophys. Res*., **101**, 20669-20686.

Parke, M.E., R.H. Stewart and D. L. Farless, 1987: On The Choice of Orbits For An Altimetric Satellite To Study Ocean Circulation and Tides. *J. Geophys. Res.*, **92** (C11), 693-707.

Pawlowicz, R., B. Beardsley, and S. Lentz, 2002: Classical Tidal Harmonic Analysis Including Error Estimates In MATLAB Using T_TIDE. Computers & Geosciences, 28, 929-937.

Petruncio, E.T., 1993: Characterization of Tidal Currents In Monterey Bay From Remote and In-situ Measurements. M.S. Thesis, Naval Postgraduate School, Monterey, California, December 1993.

Phoebus, P. A., P. A. Wittmann, and J.S. Goerss, 1994: Model Comparisons Depicting The Influence of SSM/I Wind Observations. *Seventh AMS Conference on Satellite Meteorology and Oceanography*, Monterey, California, 6-10 June 1994, pp. 389-392.

Phoebus, P.A. and J. S. Goerss, 1991: The Operational Assimilation of SSM/I Wind Speed Data. *Ninth AMS Conference on Numerical Weather Prediction*, Denver, Colorado, 14-18 October 1991, pp. 569-572.

Pickett, M., and T. Wenqing, 2001: Accuracy of QuikSCAT Near-shore Winds Off The U.S. West Coast. *Eastern Pacific Ocean Conference*, Fallen Leaf Lake, CA, 23-26 September 2001.

Pond, S., and G.L. Pickard, 1983: Introductory Dynamical Oceanography (2ed.). Oxford: Butterworth-Heinemann, 329 pp.

Poulain, P.-M., 1993: Estimates of Horizontal Divergence and Vertical Velocity In The Equatorial Pacific. *J. Phys. Oceanogr.*, **23**, 601-607.

Pullen, J.D., 2000: Modeling Studies of The Coastal Circulation Off Northern California. Dissertation, Oregon State University, March 2000.

Ramp, S.R., L.K. Rosenfeld, T.D. Tisch and M.R. Hicks, 1997: Moored Observations of The Current and Temperature Structure Over The Continental Slope Off Central California 1. A basic description of the variability. *J. Geophys. Res*., **102**(C10), 22877-22902.

Riedlinger, S., 1996: The Development of A Dynamic/Thermodynamic Numerical Model of TheYellow Sea/East China Sea Region. *Proceedings of the American Meteorological Society Conference on Coastal Oceanic and Atmospheric Prediction*, Atlanta, GA, 28 January through 2 February 1996, pp. 15-21.

Rienecker, M. M., R. Atlas, S. D. Schubert, and C. S. Willett, 1996: A Comparison of Surface Wind Products Over The North Pacific Ocean. *J. Geophys. Res*., **101**, 1011-1023.

Rhodes, R.C., H.E. Hurlburt, A.J. Wallcraft, C.N. Barron, P.J. Martin, E.J. Metzger, J.F. Shriver, D.S. Ko, O.M. Smedstad, S.L. Cross, and A. B. Kara, 2002: Navy Real-time Global Modeling Systems. *Oceanography*, **15**(1), 29-43.

Rosenfeld, L.K., F.B. Schwing, N. Garfield, D.E. Tracy, 1994: Bifurcated Flow From An Upwelling Center. A Cold Water Source For Monterey Bay. *Cont. Shelf Res*., **14**, 931-964.

Rosmond, T.E., J Teixera, M. Peng, T.F. Hogan and R. Pauley, 2002: Navy Operational Global Atmosphere Prediction System (NOGAPS). *Oceanography*, **15**(1), 99-108.

Rosmond, T.E., 1992: The Design and Testing of The Navy Operational Global Atmospheric Prediction System. Wea. Forecasting, 7, 262-272.

Round, R.D., 1993: Climatology and Analysis of The Monterey Bay Sea Breeze. M.S. Thesis, Naval Postgraduate School, Monterey, California, September 1993.

Shulman, I., C. –R. Wu, J.K. Lewis, J.D. Paduan, L.K. Rosenfeld, S.R. Ramp, M.S. Cook, J.C. Kindle, D.-S. Ko, 1999: Development of The High Resolution Data Assimilating Numerical Model of The Monterey Bay. Estuarine and Coastal Modeling, 980-994.

Skogsberg, T., 1936: Hydrography of Monterey Bay, California. Thermal Conditions, 1929-1933. *Transactions of the American Philosophical Society*, **29**, 1-152.

Smagorinsky, J., 1963: General Circulation Experiments With The Primitive Equations, I. The Basic Experiment. *Mon. Wea. Rev*., **91**, 99-164.

Steger, J.M, C.A. Collins, F.B. Schwing, M. Noble, N. Garfield, and M.T. Steiner, 1998: An Empirical Model of The Tidal Currents In The Gulf of The Farallones. *Deep Sea Res*., **45**, 1471-1505.

Stewart, R.H., 1994: Methods of Satellite Oceanography. Berkeley: University of California Press, 360 pp.

Stodden, D.Y., and G.D. Galasso, 1996: Satellite Orbit Analysis Program (SOAP) Version 8 User's Manual.. The Aerospace Corporation, El Segundo, California.

Strub, P.T., J.S. Allen, A. Huyer, and R. L. Smith, 1987: Seasonal Cycles of Currents, Temperatures, Winds, and Sea Level Over The Northeast Pacific Continental Shelf: 35 N To 48 N. *J. Geophys. Res*., **92**, 1507-1526.

Tisch, T.D., S.R. Ramp, and C. A. Collins, 1992: Observations of The Geostrophic Current and Water Mass Characteristics Off Point Sur, California, From May 1988 Through November 1989. *J. Geophys. Res*., **97**, 12535-12555.

Verron, J., and L. Cloutier, 1996: Assessing Dual-satellite Altimetric Missions For Observing The Midlatitude Oceans. *J. Atm. Ocean Tech*., **13**, 1073-1089.

Verron, J., 1990: Altimeter Data Assimilation Into An Ocean Circulation Model: Sensitivity To Orbital Parameters. *J. Geophys. Res*., **95**(C2), 11443-11459.

Von Storch, H., and C. Frankignoul, 1998: Empirical Modal Decomposition In Coastal Oceanography. In: The Sea: The global Coastal Ocean Processes and Methods, K. H. Brink and A. R. Robinson (Eds). New York: John Wiley & Sons, inc., pp. 419-455.

Wallcraft, A.J., 1991: The Navy Layered Ocean Model Users Guide. NOARL Report 35, Naval Research Laboratory, Stennis Space Center, MS 39529.

Wang, W., W.D. Nowlin Jr., and R. O. Reid, 1998: A Comparison Among LATEX, NCEP, and ERS-1 Scatterometer Winds Over The Northwestern Gulf of Mexico. *J. Atm. Ocean. Tech*., **15**, 1204-1214.

Wilks, Daniel S., 1995: Statistical Methods In The Atmospheric Sciences. San Diego: Academic Press, 467 pp.

Winant, C.D., E.P. Dever, and M.C. Hendershott, 2003: Characteristic Patterns of Shelf Circulation At The Boundary Between Central and Southern California. *J. Geophys. Res*., **108**(C2), 3-1,3-13.

Winant, C.D., C.E. Dorman, C.A. Friehe, and R.C. Beardsley, 1988: The Marine Layer off Northern California: An Example of Supercritical Channel Flow. *J. Atm. Sci*., **45**, 3588-3605.

Wunsch, C., 1996: The Ocean Circulation Inverse Problem. Cambridge: Cambridge University Press, 442 pp.

THIS PAGE INTENTIONALLY LEFT BLANK

INITIAL DISTRIBUTION LIST

1. Defense Technical Information Center
   Ft. Belvoir, VA

2. Dudley Knox Library
   Naval Postgraduate School
   Monterey, CA

3. Associate Professor Mary L. Batteen
   Department of Oceanography, Code OC/Bv
   Naval Postgraduate School
   Monterey, CA

4. Professor Roland W. Garwood
   Department of Oceanography, Code OC/Gd
   Naval Postgraduate School
   Monterey, CA

5. Professor Curtis L. Collins
   Department of Oceanography, Code OC/
   Naval Postgraduate School
   Monterey, CA

6. Associate Professor Wendell A. Nuss
   Department of Meteorology, Code MR/
   Naval Postgraduate School
   Monterey, CA

7. Assistant Professor Douglas Miller
   Department of Meteorology, Code MR/
   Naval Postgraduate School
   Monterey, CA

8. Dr. Paul May
   Naval Research Laboratory
   Monterey, CA

9. Mr. Mike Clancy
   Fleet Numerical Meteorology and Oceanography Center
   Monterey, CA

10. Mr. Peter DeWitt
    Fleet Numerical Meteorology and Oceanography Center
    Monterey, CA

11. Commander Henry Jones
    Department of Oceanography
    United States Naval Academy
    Annapolis, MD

12. Oceanographer of the Navy
    Naval Observatory
    Washington, DC 20390

13. Commander
    Naval Meteorology and Oceanography Command
    Stennis Space Center, MS

14. Commanding Officer
    Naval Oceanographic Office
    Stennis Space Center, MS